SYNTHESIS AND CHARACTERIZATION OF TITANIA BASED ELECTROCERAMIC VOLTAGE SENSORS

COMPUTERISED

A Thesis submitted to the

UNIVERSITY OF PUNE

For The Degree of

DOCTOR OF PHILOSOPHY

in

PHYSICS

TH--1063

by

SANTHOSH P. N.

Physical Chemistry Division

National Chemical Laboratory

Pune - 411 008

November 1996

---------------------------------- TO MY

BELOVED PARENTS

CERTIFICATE

This is to certify that the thesis entitled "**Synthesis and characterization of titania based electroceramic voltage sensors**" describes the original research work done by **Mr.Santhosh P.N.** under my supervision for the Degree of **Doctor of Philosophy in Physics** of the **University of Pune**. Such material as has been obtained from other sources has been duly acknowledged in the Thesis.

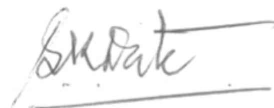

Place: Pune
Date: 27th NOV. 1996

Dr. S. K.Date
Scientist 'F'
NCL, Pune.
(Research Guide)

Acknowledgements

*I would like to thank my guide, **Dr.S.K.Date**, who through his inspiring guidance helped me in taking up this problem and completing the Thesis work within the stipulated time. I found in him, a guide who is always there to help you out not only in scientific problems but personal as well. Without his help, I am sure, I would have left my research carrier during those days of uncertainty. I am deeply indebted to him for his timely help.*

*I would like to thank two persons who have stood by my side all through my Ph.D. work. Firstly, I like to thank my labmate, my constant companion and my former roommate, **Mr.P.S.Anil Kumar**, who went out of his way to support and stand by me for all my scientific as well as personal problems. Secondly, I thank **Dr.P.A.Joy**, for being there, as an elder brother and a friend during those days when I really needed the support to come out of the bad patch I was going through.*

*I would like to thank **Dr.S.B.Deshpande** and **Dr.H.S.Potdar** for their wholehearted support to me for finishing this thesis in time. Thanks are also due to Dr.D.K.Kharat(ARDE), Dr.C.E.Deshpande, Mrs.J.J.Shrotri and Gangopadhyay for their help during the course of this work. I like to thank all SIL staff, in paticular Dr.S.R.Sainkar, Dr.S.D.Pradhan and Dr.A.Mitra for their help in SEM, TGA and XRD measurements. I also like to thank Dr.K.Vijayamohanan, Dr.K.Sreedhar, Dr.I.S.Mulla, Mrs.A.Suguna and Dr.S.D.Sathaye for their support. I would like to express my sincere gratitude and thanks to **Mr.Koshy** for his support during all these five years. I also thank Devidas for his help.*

*I express my sincere thanks to **Dr.A.R.Kulkarni**, Associate Professor, IIT, Bombay, for allowing me to carry out the impedance measurements in his lab and for the useful discussions. I would like to thank Shyamala for her help during the measurements.*

*I would like to thank **Radhakrishnan, the bearded-gullible Chettan**, for being a close friend and giving me the support I need. My sincere thanks to **Reni** and **Shanti** for being so nice friends whose friendship I really do cherish. Thanks to **Jayasree Sham** for being such a wonderful sister. My sincere gratitude to my friends Rajeev, Pradeep(Pallan), N.Pradeep, Suresh, Chengal, Krishanu, Selvam, Soumen, Anand, Dinesh, Gopal, Prasad, Jayaprakash, Rajesh, Seayad, Asokan, Mahesh, Manoj, Sindhu, Deena, Rohini, Prakash, Sipra, Neepa and many others. My sincere thanks to my friend **Binod** for his moral support.*

I express my sincere thanks to Dr.Dongare, Dr.Rajiv, Puru, Sidhu and Bhandari for making the evening hours at the Badminton court worth remembering.

During these five years, the support from my brother, **Dr.Suresh.P.N**, *was immense. He was instrumental in making me continue my research carrier at NCL when I was thinking to discontinue my research carrier to be with my parents who were going through a bad period. I also like to thank my sister-in-law,* **Dr.Vrinda**, *for being so supportive. I also like to thank all my family members, who were there to help my parents out, during those bad days when we needed their support the most.*

I thank each and every person who have helped and supported me during this research period.

I thank **Director NCL,** *for allowing to submit this work in the form of a Ph.D thesis..*

Finally I thank the **University Grants Commission** *for Junior and Senior Research Fellowships.*

P.N. Santhosh

Santhosh.

Contents

Chapter 1

1.1	Ceramics	1
1.2	Electroceramics	4
1.3	Electroceramic sensor	8
1.4	Voltage sensors or varistors	8
1.5	Zinc oxide varistors	9
1.6	Performance parameters of a varistor	12
1.7	Microstructure of ZnO varistors	14
1.8	Microstructural engineering of varistors	16
1.9	Processing methods and their influence on varistor properties	22
1.10	Energy barrier, electronic states and their detection	25
1.11	Degradation behaviour	27
1.12	Theoretical models for electrical conduction	28
1.13	Impedance analysis	31
1.14	Search for new varistors	33
1.15	Aim of this work	35
1.16	Titanium dioxide	35
1.17	Tin dioxide	38
1.18	Application of varistors	38
1.19	Varistor research and market analysis	40
	References	42

Chapter 2

2.1	Introduction	51
2.2	Part-I Synthesis of active powders	51
	2.2.1 TiO_2 based voltage sensors	51
	2.2.1.1 Solid state synthesis route	51
	2.2.1.2 Chemical synthesis route	52
	2.2.2 SnO2 based voltage sensors	54
	2.2.2.1 Solid state synthesis route	54

2.2.2.2 Chemical synthesis route 55
2.3 Part-II Physico-chemical characterization 56
2.3.1 Density 56
2.3.2 Thermal analysis(DTA/TGA) 56
2.3.3 Phase analysis by X-ray diffraction 56
2.3.4 Microstructural analysis by Scanning Electron Microscope 57
2.4 Part-III Electrical Characterization 57
2.4.1 Electroding 57
2.4.2 DC current-voltage characterization 59
2.4.3 AC impedance analysis 60

Chapter 3

3.1 Introduction 61
3.2 Experimental results and analysis 61
3.3 Current-voltage(I-V) characteristics 62
3.4 DTA/TGA analysis 65
3.5 Density 65
3.6 X-ray diffraction for phase analysis 67
3.7 Scanning electron micrographs of fractured surface 69
3.8 Impedance analysis 71
3.9 Bode plots 74
3.10 TiO_2 voltage sensors doped with Ca^{2+}, Ba^{2+}, Mg^{2+} in place of Sr^{2+} 79
3.10.1 Current-voltage(I-V) characteristics 79
3.10.2 Density 82
3.10.3 Phase analysis by X-ray diffraction 84
3.10.4 Scanning electron micrographs of fractured surface 84
3.11 Chemically synthesized TiO_2 voltage sensor 88
3.11.1 Current-voltage(I-V) characteristics 88
3.11.2 DTA/TGA analysis 90
3.11.3 Density 90
3.11.4 Phase analysis by X-ray diffraction 91
3.11.5 Scanning electron micrographs of fractured surface 94

3.12 Discussion 94
3.13 Conclusions 99
References 100

Chapter 4

4.1 Introduction 101
4.2 Current-voltage(l-V) characteristics 102
4.3 Density 105
4.4 X-ray diffraction analysis 107
4.5 Scanning electron micrographs of fractured surface 108
4.6 Impedance analysis 110
4.7 Bode plots 113
4.8 Effect of other Co concentrations 120
4.8.1 Current-voltage(I-V) characteristics 121
4.8.2 Density 124
4.8.3 X-ray diffraction for phase analysis 124
4.8.4 Scanning electron micrographs of fractured surface 126
4.9 Chemically synthesized SCNA samples 128
4.9.1 Current-voltage(I-V) characteristics 128
4.9.2 DTA/TGA analysis 130
4.9.3 Density 131
4.9.4 X-ray diffraction for phase analysis 131
4.9.5 Scanning electron micrographs of fractured surface 134
4.9.6 Impedance analysis 135
4.10 Discussion 138
4.11 Conclusions 140
References 142
List of Publications

CHAPTER 1

INTRODUCTION

TH-1063

1.1 CERAMICS

The word ceramic is of Greek origin which means potter's earth (Keramos)[1]. Ceramics are the group of non-metallic inorganic solids. Advanced ceramics are developed from chemical synthesis routes or from naturally occurring materials that have been finely refined [2]. The diversity of ceramic products, which ranges from microscopic single-crystal whiskers, tiny magnets, and substrate chips to multiton refractory furnace blocks, from single-phase closely controlled compositions of multiphase multicomponent brick, and from porefree transparent crystals and glasses to lightweight insulating forms is such that no simple classification is possible [3].

A variety of new ceramics has been developed in the last 40 years. These are of particular interest because they have either unique or outstanding properties [4]. In order to indicate the active state of development, a few are listed below.

Electrooptic ceramics such as lithium niobate ($LiNbO_3$) and lanthanum modified lead zirconate titanate (PLZT) provide a medium by which electrical information can be transformed to optical information or by which optical functions can be performed on command of an electrical signal[5]. Magnetic ceramics that form the basis of magnetic memory units in large computers and their unique electrical properties are particularly useful in high frequency microwave electronic applications[6]. Nuclear fuels based on Uranium dioxide (UO_2) [7]. Ceramic carbides and nitrides with unusually good properties for special applications like commercially important refractories and potential gas turbine gas components have been developed. Metal ceramic composites are now an important part of the machine tool industry and have important uses as refractories. Ceramic borides have been developed which have unique properties of high temperature strength and oxidation resistance[8,9]. Ferroelectric ceramics such as barium titanate have been developed which have extremely high dielectric constants and are particularly important as electronic components[10]. Non-silicate glasses have been developed which particularly useful for infrared transmission, special optical properties and semiconducting devices[11].

The demand for improved performance/properties has led to the development of these new materials and consequently, the availability of new materials has led to uses based on their

unique applications. This cycle of new ceramics-new uses-new ceramics has accelerated with better understanding of the processes involved in the forming of ceramics. The different ceramic materials classified according to their properties and uses are given in figure**1.1**. This vast field of new materials, now coined as the Advanced ceramics, is the group with the most market growth during the past few years[12]. For instance, the total value of the U.S advanced ceramics components market for 1994 was $4.9 billion. This is expected to increase to $8.5 billion by 2000 with a growth rate of 9.8%.

Figure 1.1 Advanced ceramic classification according to use and properties

These advanced ceramics are generally classified into

a) Structural ceramics are those used as cutting tools, wear components, heat exchangers and adiabatic engine components. Materials such as silicon nitride (Si_3N_4), Silicon carbide (SiC), Zirconia (ZrO_2), Boron carbide (B_4C), Alumina (Al_2O_3) and Sialon(SiAlON) are typical examples of structural ceramics.

b) Electroceramics are those used as insulators, substrates and other components used in electronic equipments. They include insulators, substrates, capacitors, integrated packages, magnetic ferrites, piezoelectric ceramics, semiconductors and superconductors. Materials such as barium titanate ($BaTiO_3$), zinc oxide (ZnO), lead zirconate titanate ($Pb(Zr_xTi_{1-x})O_3$), lithium niobate ($LiNbO_3$), lanthanum strontium cuprate ($LaSrCuO_4$) are few of the materials which come under this category.

c) Coating materials. Coating is the process by which a surface is modified, yielding a composition or property gradient between the bulk and the surface. Coating is often performed to alter or improve properties of the component. Chemical vapor deposited (CVD) diamond for cutting tools and also for electronic applications is one of the examples of coating materials.

d) Composites are materials with two or more dissimilar constituents which is used to display a combination of preferred characteristics of each of the components. One of the principal areas of composite growth has been in the toughening of structural ceramics through whisker and fiber reinforcement. For example, SiC-fibre and SiC-particulate reinforced Al_2O_3 now have many applications like cutting tools.

Critical factors in the commercialization of advanced ceramics are the starting powders and, in the case of structural and some electronic ceramics, the way they are shaped. Figure**1.2** represents the ultrastructural processing chemistry approach to obtain high performance ceramics. Typical defects in ceramic components often are introduced by powder themselves, and/or in the forming and densification process. Improvements in powder processing and forming technologies will improve the reliability of advanced ceramics and lower their cost. This in turn will increase market growth.

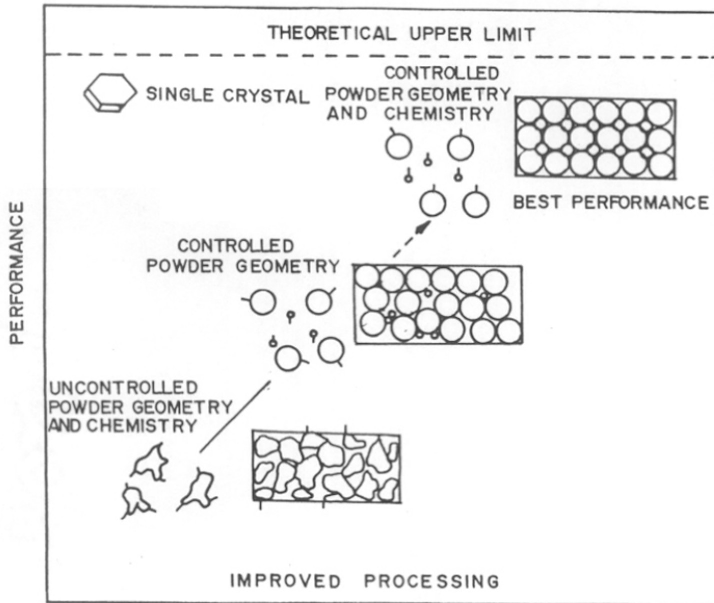

Figure1.2 Conceptual approach of ultrastructural processing chemistry route

In this thesis the field of interest is electroceramics. A detailed introduction to electroceramics is given in the next section.

1.2 Electroceramics

Electroceramics or electronic ceramics can be considered as materials whose uses rely primarily on their electrical or magnetic properties rather than their mechanical behaviour. The electroceramics field is a mature one and dates back to 1940's when insulating properties of Al_2O_3 were used in spark plugs. But now a days this is a rapidly expanding area of materials science and forms the largest sector of advanced ceramics. Examples of electroceramics include, ceramics insulators, varistors, piezoelectrics, capacitors, gas sensors, electrooptic devices, semiconductors, superconductors, etc. Hence all these ceramic materials which are used in applications related to electronics can be called as electroceramics. A brief description of each of these electroceramic materials are given below.

Ceramic insulators: Special materials whose primary function is the physical separation of conductors and the regulation and prevention of current flow between them. Important other

functions are to give mechanical support, heat dissipation and environmental protection of conductors. The main advantage of ceramics as insulators is their property of high-temperature operations without hazardous degradation in chemical, mechanical or dielectric properties. Most of the ceramic glasses, porcelains, oxide and nitride materials, as well as mica come under the category of ceramic insulators [13].

Ceramic capacitor materials: Capacitor's basic function is energy storage. It is used to block direct current or to couple ac circuits. The properties of capacitor dielectric materials which determine in detail the manner in which the energy storage function is performed are (a) dielectric constant which measures the response of the dielectric polarization mechanism to an electric field (b) dissipation factor which measures the net efficiency of the polarization process (c) Insulation resistance, a measure of the efficiency of dc blocking and (d) temperature, frequency and field strength dependence of the parameters above. Examples of ceramic materials used as dielectric materials for capacitor applications are porcelains, rutile TiO_2, barium titanate, relaxor dielectrics like tungsten bronze structure system. Ceramic capacitors are of different types. They are film capacitors, multilayer capacitors, barrier layer capacitors and multilayer GBBL capacitors [14-18].

Ferroelectric ceramics: Ferroelectric materials are characterized as crystals that possess a spontaneous dipole and this dipole is reversible by an electric field of some magnitude less than the dielectric breakdown of the material itself. The number of ferroelectric materials known today include large number of ceramic solid-solution compositions. Most outstanding feature of a ferroelectric ceramic is its hysteresis loop (polarization vs electric field). It describes the non-linear polarization switching behaviour as a function of field. Examples of ferroelectric ceramics are barium titanate, lead zirconate titanate(PZT), lead niobate, bismuth titanate, sodium potassium niobate, lead titanate, relaxor ferroelectrics and polymer composites[19-24].

Electrooptic ceramics: Ferroelectric ceramics possessing useful optical properties are termed as electrooptic ceramics. The properties which were found to be important are (1) electrically poled, thin polished plates of ferroelectric ceramics transmit light (2) these materials exhibited either electrically variable light scattering behaviour or electrically variable optical birefringence (3) their light transmission characteristics depend both on the

thoroughness and direction of poling and (4) small local area of the ceramic can be switched independently of adjacent areas. PLZT and lithium niobate are the most commonly used electrooptic ceramics [25,26].

Magnetic ceramics: Ceramic based materials compose a major share of both hard and soft magnetic materials. Permanent magnet applications are found in the aerospace, automotive, computer, electronics, instrumentation, medical, telecommunications etc. These permanent or hard ferrite materials are part of a family of complex oxides having the general composition $MO.6Fe_2O_3$ (eg: $SrO.6Fe_2O_3$, $BaO.6Fe_2O_3$). The performance characteristics of the ferrites are being improved following many chemical approaches. Soft magnets are important in many electrical and electronic systems. Soft ferrites can be classified further according to the frequency of use and crystal structure. Mn-Zn, Ni-Zn and Mg-Zn ferrites are the widely used soft ferrites depending on the frequency of interest [27-29].

Multilayer ceramic technology: MLC is one of the most challenging growth areas in the ceramic industry today. The technology lends itself to computer control of the process, including the design and artwork, and this has become one of the most sophisticated ceramic technologies yet developed. Successful design of an MLC substrate depends on complete understanding of the green and fired properties of the ceramic and the metallurgy used and careful matching of shrinkage curves between metal and ceramic during firing [30,31].

Table 1.1 Classification of Ceramic Sensor Materials

Exploited attribute	General Application	Functional Property	Material
Bulk Properties	Temperature sensor Oxygen gas sensor Oxygen gas sensor Pressure sensor Radiation sensor	NTC thermistor Solid electrolyte Semiconductor Piezoelectric Pyroelectric	NiO, Fe_2O_3 ZrO_2 TiO_2, $SrTiO_3$ $Pb(Zr,Ti)O_3$ PZT type
Grain boundary properties	Temperature sensor Voltage sensor/ electronic sensor	PTC thermistor Semiconducting varistor	Doped $BaTiO_3$ ZnO, $SrTiO_3$
Surface effect properties	Humidity sensor Electronic sensor	Catalyst/ Semiconducting	$ZnO-Cr_2O_3$ $MgCr_2O_4$ SnO_2, $BaTiO_3$

Table 1.2 Ceramic materials which are applicable as sensors

	Output	Effect		Material (form)	Remarks
TEMPERATURE SENSOR	Change in resistance	Temperature changes carrier density	(NIC)	NiO , FeO , CuO , MnO , CoO , Al_2O_3 SiC , (Bulk , Thick Film , Thin Film)	Thermometer , bolometer
			(PIC)	Semiconductive , $BaTiO_3$ (Sintered body)	Overheat protection sensor
		Semi-conductor metal phase transition		VO_2 V_2O_5	Thermal switch
	Change in magnetism	Ferrimagnetism paramagnetism transition		Mn Zn based ferrite	Thermal switch
	Electromotive force	Concentrated oxygen cell		Stabilized zirconia	High-temperature corrosion resistance thermometer
POSITION/SPEED SENSOR	Change in waveorm of reflected wave	Piezoelectric effect		PZT : ($PbTiO_3$, $PbZrO_3$)	fish finder , flaw detector blood flow meter
OPTO SENSOR	Electromotive force	Collecting effect		$LiNbO_3$, $LiTaO_3$, PZT , $SrTiO_3$	Infrared ray detection
		Anti-stoke measurement		LaF_3 (Vb , Pr)	
		Progressive wave doubling effect		Piezoelectries , $Ba_2NaNb_5O_{15}$(BNN) $LiNbO_3$	Infrared ray detection
	visible light	Fluorescence		ZnS (Cu , Al) , Y_2O_2S (Eu)	Color TV CRT
				ZnS(Cu , Al)	X-ray monitor
		Thermal fluorescence		CaF_2	Thermal fluorescence dosimeter
GAS SENSOR	Change in resistance	Inflammable gas contain combustion reaction heat		Pt Catalyst / alumina Pt. Line	Inflammable gas thermometer and alarm
		Migration of charge due to adsorption and desorption of gas from an oxidized semiconductor		SnO_2 , In_2O_3 , ZnO , WO_3 , γ - Fe_2O_3 NiO , CoO , Cr_2O_3 , TiO_2 , $LaNiO_3$ (La , Sr) CoO_3 , (Ba , La) TiO_3 etc.	gas alarm
		Temperature changes in a thermistor due to gas heat conductive dissipation		Thermistor	High -density gas sensor
		Stochimetric Change in oxide semiconductors		TiO_2 , CoO , MgO	Automibile exhaust gas sensor
	Electromotive force	High temperature solid electrolytic Concentrated oxygen cell		Stabilized Zirconia (ZrO_2 CaO , ZrO_2 Y_2O_3 , La_2O_3) Thoria ($ThO_2Y_2O_3$)	Exhaust gas sensor (random sensor) Molten steel and molten steel oxygen content analyzer
	Amount of electricity	Coulomb titration		Stabilized zirconia	Lean combustion oxygen sensor
HUMIDITY SENSOR	Change in resistance	Moisture absorption in conductivity		LiCl , P_2O_5 , ZnO , Li_2O	Hygrometer
		Oxide semiconductor		TiO_2 , $NiFe_2O_4$, $MgCr_2O_4$, TiO_2 , ZnO , Ni ferrite , Fe_3O_4 Colloid	Hygrometer
	Permittivity	Change in permittivity due to moisture absorption		Al_2O_3	Hygrometer
ION SENSOR	Electromotive force	Solid electrolytic film concentrated cell		AgX , LaF_2 , Ag_2S_3 , Thin glass film , CaS , AgI	Ion concentration sensor
	Resistance	Gate adsorption effect MOSFET		Si (Gate material H for Si_3N_4 / SiO_2 S_2 for : Ag_2S , X for : AgX , PbO)	Ion sensitivity FET (II SET)

1.3 Electroceramic sensors

Among the electroceramic materials discussed above the field of interest in this thesis is Electroceramic sensors. Ceramic sensors have currently become an integral part of the society and are being used in a variety of fields like Industry, defence and various household appliances [32].

As mechanical, electronic and electromechanical devices increase in technical complexity and understanding of the hazards of industrial and technological by-products also increased, diverse applications are seen for sensors which can be used to provide feedback for control circuitry and provide warning and detection of hazardous conditions/or toxic substances. The specific classification of ceramic sensor materials in respect to whether they use bulk properties, grain boundary properties or surface effect properties are given in Table**1.1**.

In addition to the above classification, Ichinose[33] has compiled the exhaustive list of ceramics which are being in use as ceramic sensors in a variety of field. Table**1.2** gives a listing of these electroceramic materials which are applicable as sensors.

1.4 Voltage sensors or Varistors

The power fluctuations/over-voltage usually encountered due to natural lightning and switching operations can permanently damage the electronic/electrical devices. It is essential to suppress/bypass these over voltages to protect the sensitive components/devices. A device which performs the duty of protecting the electronic device is called the Voltage sensor/Voltage dependent resistor (VDR) or voltage suppresser or surge arrestors or more popularly called the **VARISTOR**. Voltage sensors offer the circuit protection to the sensitive devices during continuous operations.

In early stages, spark gaps were used for over-voltage protections and guarding the sensitive devices. These spark gaps remain short-circuited after the first spark and hence were not repeatedly usable. The development of silicon carbide(SiC) based voltage sensors around 1930[34] set the stage for the emergence of the classical type of voltage sensors which are used extensively from 1930 to the middle of 1970. These voltage sensors use a set of gaps in series with the SiC based voltage sensor. The presence of series gaps in this type of voltage

sensors and the limited non-linearity(~5) of the SiC based voltage sensors restricted the protective actions. The most important path breaking development in the field of voltage limiters came with the discovery of highly non-linear behaviour in ZnO doped with other oxides such as Bi_2O_3, Sb_2O_3, CoO, MnO, Cr_2O_3 etc by Matsuoka[35]. These varistors were found to have better performance parameters compared to the early surge arrestors or voltage limiters.

1.5 Zinc Oxide Varistors

Zinc oxide varistors [36] are electronic ceramic devices whose primary function is to sense and limit transient voltage surges and to do so repeatedly without being destroyed. These are ZnO based , ceramic semiconductor devices with highly non-linear current-voltage characteristics similar to back to back Zener diodes but with much greater current and energy handling capabilities[37-40].

The most important property of a varistor is its non-linear current-voltage characteristics as illustrated in figure**1.3** and **1.4**. Figure**1.3** represent the ideal curve for a non-linear resistor material.

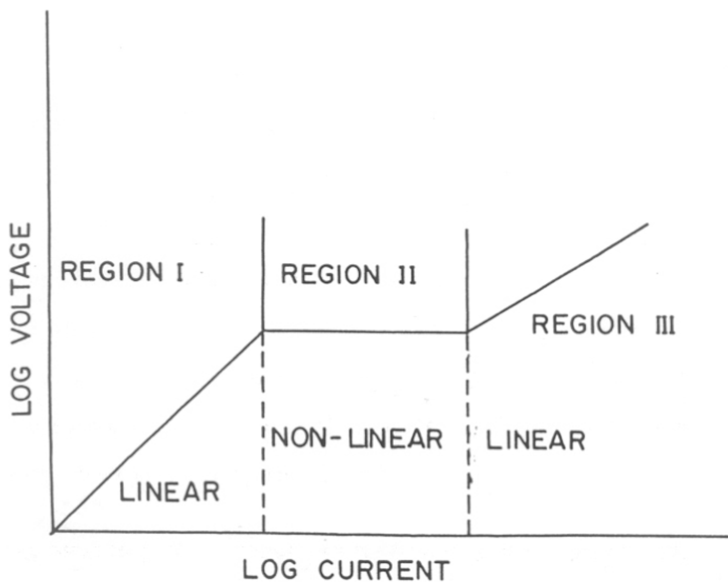

Figure1.3 Current-voltage (I-V) curve of an ideal varistor

Functionally , a varistor or voltage sensor acts as an insulator before reaching a critical voltage called the breakdown voltage. This region is called as the pre-break down or low current linear region. Above this voltage, the varistor starts conducting heavily. This region is the most important part of the varistor, called the non-linear region. Again at high currents (>10^3 Amp/sq.cm), it exhibits ohmic behaviour. This region of the I-V curve is called high-current linear region. This is indicated in figure**1.3**. A practical varistor will never show a clear distinction between the linear region and the non-linear region. i.e., we cannot point out the point of inflection. A practical I-V curve will always look like that given in figure**1.4**.

The electrical features that make ZnO varistor attractive to the designer are the non-linear or non-ohmic characteristics in the conductive mode and the low leakage current of the ready operating voltage in the resistive mode. These features are highlighted by referring to three important regions of the curve given in both figures**1.3** and **1.4**.

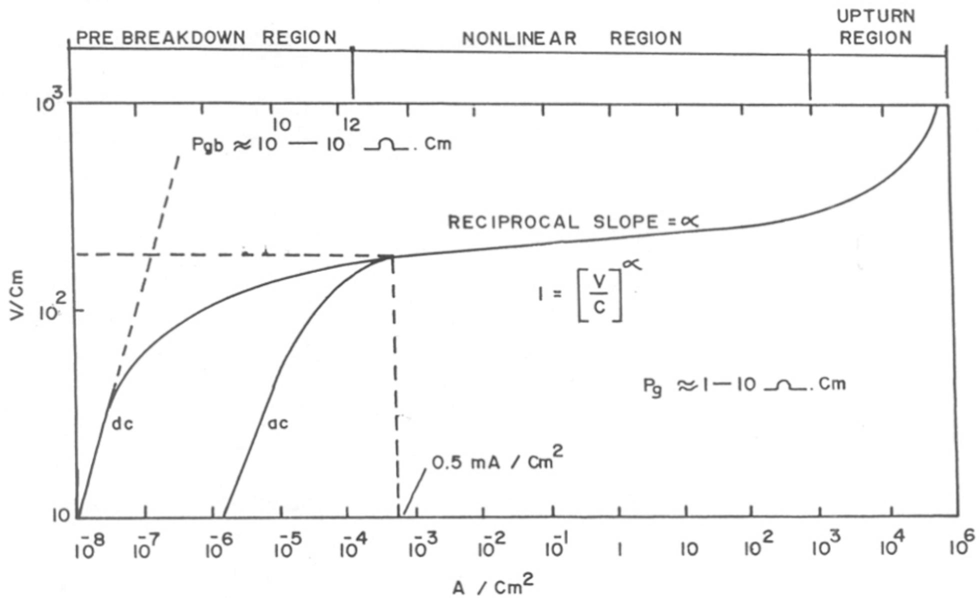

Figure 1.4 Typical current-voltage curve of a practical varistor.

a) **Low-current-linear region or pre-breakdown region**

The current-voltage curve in this region have a linear relation as can be seen from the figure. This is the low-current region. i.e., for currents $<10^{-4}$ Ampere/cm^2. The slope of the I-V curve in this region will give the dc resistance of the sample. This resistance is approximately equal to the grain boundary resistance. This is because the insulating resistance of this grain boundary region is much higher than the grain resistance. Hence the current voltage characteristics of this linear low-current region is controlled by the resistance of the grain boundary.

b) **Intermediate non-linear region**.

The non-linear region of the intermediate current is the heart of the varistor. In this region the device conducts an increasingly large amount of current for a small increase in voltage. The non-linear region may extend over 6 to 7 orders of magnitude of current. the degree of non-linearity is determined by the flatness of the curve. i.e., flatter the curve, better the device. The current-voltage curve in this non-linear region is explained by the relation

$$I \propto (V)^{\propto} \qquad \text{---------------------------(1.1)}$$

here, V is the applied voltage, I is the current passing through the varistor and $\propto$ is the non-linear coefficient. Magnitude of $\propto$ determines the flatness of the current-voltage curve. i.e. flatter the curve means higher non-linear coefficient $\propto$. The material with large $\propto$ will have superior varistor properties.

c) **High-current linear region or Upturn region**

In the high current or upturn region ($>10^3$ Ampere/cm^2), the current-voltage characteristics is again linear, similar to that in the low-current prebreakdown region. This region of the current-voltage curve is controlled by the impedance of the grain. Hence the dopants which are incorporated in the grains have a great influence on the high-current upturn properties. The current in this region is rather high and hence it is not possible to measure the current characteristics in this region in the dc model. This is because there is a distinct possibility of a heat breakdown. Usually high voltage pulses is used to measure the I-V characteristics in this region.

To understand the characteristics of a varistor, it is necessary to study all the three regions mentioned above. Among these regions, the non-linear intermediate region plays the most important part.

1.6 Performance parameters of a Varistor

The important performance parameters of the varistor are the non-linear coefficient($\propto$) and the breakdown voltage (E_{1mA}). Other performance parameters are also there which are important in a commercial point of view. The performance parameters for device applications are summarized in Table **1.3.**

A description of the two most important performance parameters $\propto$ and E_{1mA} which is relevant to this Thesis is given below.

a) **Nonlinear coefficient ($\propto$)**

The current voltage relation of a varistor in the non-linear region can be empirically expressed as

$$I = K (V)^{\propto} \qquad \text{------------------------(1.2)}$$

Table 1.3 Parameters for device application

Parameter	Function	Equation*
Nonlinear coefficient	Protective level	$I = K (V)^{\propto}$
Nonlinear voltage	Voltage rating	$C = V / I^{(1/\propto)}$ V at 1mA
Leakage current	Watt loss/operating voltage	$I_R = V_{ss} / R_{gb}$
Life	Stability	$P_G < P_D$
Energy absorption	Survival	$J = I\,V\,t$

* I is the current, V is the voltage, K is a constant, I_R is resisitive current, V_{ss} is steady state voltage, R_{gb} is grain boundary resistance, P_G is power generated, P_D is power dissipated, J is Joules and t is time.

where V is the applied voltage across the sample, I is the current flowing through the sample, K a constant of proportionality and $\propto$ the non-linear coefficient. From equation (1.2) one can arrive at an expression for $\propto$ as

$$\propto = d \ln(I) \,/\, d \ln(V) \qquad \text{---------------------(1.3)}$$

the $\propto$ value increases in the prebreakdown region, reaches a maximum value in the breakdown region, and then diminishes in the upturn region. Because of this change in $\propto$ in the three regions of the I-V curve, it is necessary to indicate the current range in which the $\propto$ value is measured. In practice, therefore, the $\propto$ value is estimated between two desired magnitude of currents and corresponding voltages by

$$\propto = \log (I_2 / I_1) \;/\; \log(V_2 / V_1) \qquad \text{------------------(1.4)}$$

the practical implication of equation (1.2) is that, for a given discharge current, the voltage rise is lowered with increasing values of $\propto$. The importance of a ZnO varistor results from the fact that their $\propto$ values are considerably larger than other (SiC) known varistors .

(b) **Breakdown voltage (E_{1mA})**

The varistor is characterized by the voltage which marks the transition form linear to non-linear mode of operation. The voltage at the onset of the non-linearity, just above the "knee" of the I-V curve, is the breakdown voltage or non-linear voltage which determines the voltage rating of the device. Because of a lack of sharpness in the I-V curve of a practical varistor, as can be seen in figure(1.4), the exact value of the voltage is difficult to find. So, the convention followed by the researchers in this area is by defining the breakdown voltage as the voltage observed when 1mA current flows through the system. The breakdown voltage of a varistor is controlled by the grain size and the thickness of the material. For a given grain size, the breakdown voltage of the varistor can be manipulated to suit the application by changing the device size.

To calculate the varistor parameters, the convention followed is to plot current density (Amperes/cm^2) vs voltage (Volts/mm) on a log-log scale. The slope of this curve in the non-linear region directly gives the non-linear coefficient and the voltage corresponding to 1mA as the breakdown voltage which can be easily calculated from this curve. The factors deciding the non-linear coefficient, breakdown voltage and other performance parameters (energy handling capability, and life time) are well studied[41-46]. This field of changing the performance parameters by dopant additions, preparation conditions, shape forming, generally come under the category of microstructural engineering of the varistors. Since the final parameters of a varistor device is affected by the grain, grain boundary and their

distributions, a thorough understanding of the microstructure is necessary to evaluate a varistor.

1.7 Microstructure of ZnO Varistors

The microstructure of a ZnO varistor consists of large (few microns) electrically conducting n-type ZnO grains surrounded by electrically insulating grain boundaries (few nanometers). This functional microstructure of a varistor is formed as a result of various dopant distributions brought about by sintering mechanisms. The microstructure of the ZnO varistor has been extensively studied and several reviews are available in the literature[47-50].

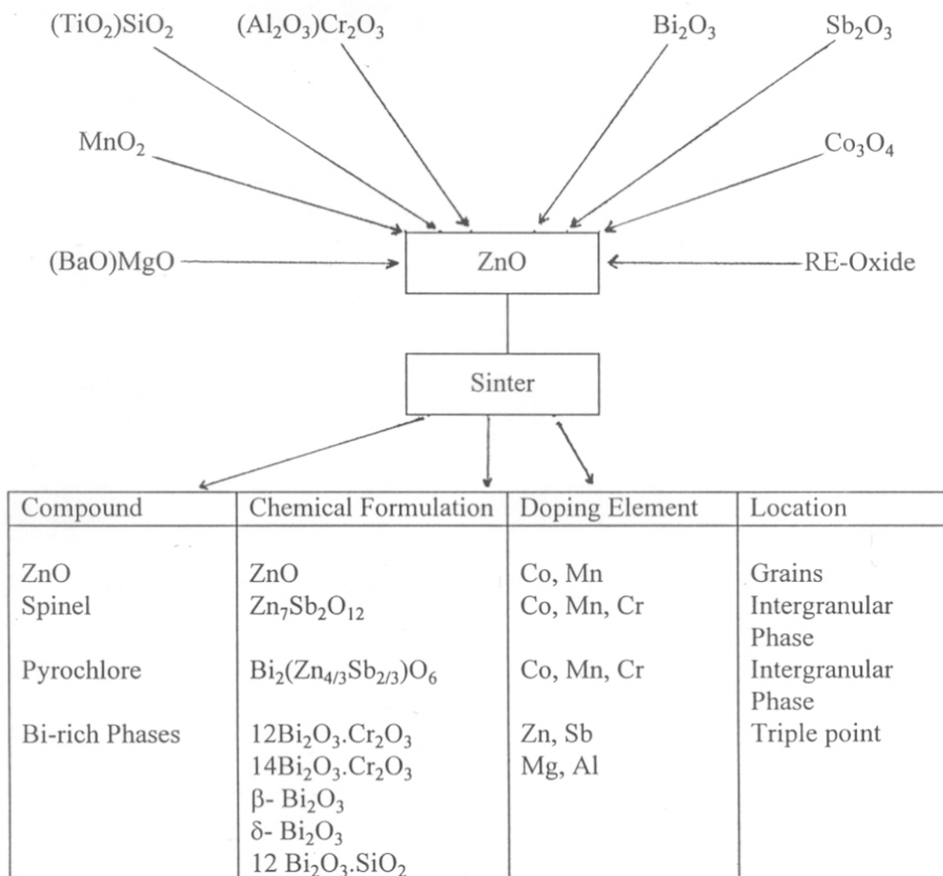

Compound	Chemical Formulation	Doping Element	Location
ZnO	ZnO	Co, Mn	Grains
Spinel	$Zn_7Sb_2O_{12}$	Co, Mn, Cr	Intergranular Phase
Pyrochlore	$Bi_2(Zn_{4/3}Sb_{2/3})O_6$	Co, Mn, Cr	Intergranular Phase
Bi-rich Phases	$12Bi_2O_3.Cr_2O_3$ $14Bi_2O_3.Cr_2O_3$ β- Bi_2O_3 δ- Bi_2O_3 $12\ Bi_2O_3.SiO_2$	Zn, Sb Mg, Al	Triple point

Figure 1.5 Major findings of microstructural analysis [36]

Major research efforts on microstructure analysis are summarized in figure**1.5**. During the heat treatment the basic components formed are ZnO, spinel, pyrochlore and many bismuth rich phases. There are other minor phases which are not readily detectable by conventional techniques. The spinel and pyrochlore phases are found to restrict grain growth. The pyrochlore phase is favored at low temperatures, whereas the spinel phase is formed at high temperatures[51-54].

The research efforts have led to a microstructural electrical model for a ZnO varistor. During the processing time, various dopant species are distributed in the matrix in such a way that the near grain boundary region becomes highly resistive ($\rho_{gb} \approx 10^{12}$ Ω.cm) and the grain interior highly conductive ($\rho_g \approx 1$ to 10 Ω.cm).

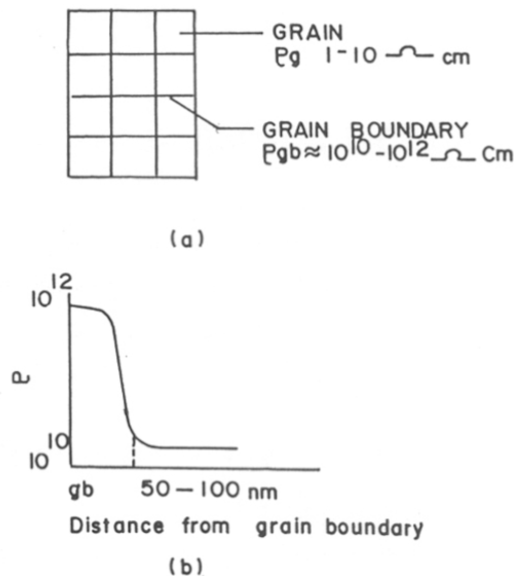

Fig 1.6 (a) Ideal microstructure of a varistor and (b) resistivity profile at the grain boundary.

Figure**1.6(a)** shows the schematic diagram of a varistor. Here we presume the device to be made of conducting ZnO grains, shown by squares, separated by insulating grain boundaries (thick lines). A sharp drop in resistivity occurs from the grain boundary to grain within a distance of a few nanometer length (≈ 100nm) known as the depletion layer. This steep drop is shown schematically in figure**1.6(b)**.

This understanding of the grain and grain boundary distribution and their resistivity has led to the correlation of the microstructural and electrical properties. When a voltage is applied to a varistor in the pre-breakdown region, the leakage current is entirely controlled by the grain boundary impedance and the high current region or the upturn region is entirely controlled by the impedance of the grain. The intermediate non-linear region is indirectly controlled by the resistivity differential between the grain boundary and grain.

The breakdown voltage of a varistor can also be controlled by the change in microstructure. For a given varistor, the breakdown voltages corresponding to a single barrier will be relatively constant, at all the points in the sample. Therefore, if a sample of given thickness is taken, we can change the breakdown voltage of that device by changing the grain sizes. If E_{gb} is considered as the breakdown voltage per grain boundary, E_{1mA} is the breakdown voltage per mm of the sample and n_g is the number of grains per mm of the sample, then

$$E_{gb} = E_{1mA} / n_g \qquad \text{------------------(1.5)}$$

hence, it is clear from the equation that for a given sample size, the breakdown voltage can be manipulated by changing the grain size. Similarly for a given grain size, the breakdown voltage can be changed by increasing or decreasing the thickness of the varistor dense compacts.

1.8 Microstructural engineering of varistors.

Varistor properties are changed by changing the microstructure and by creating intermediate energy states in the ZnO grains and grain boundary structures. This is brought about by dopant distribution in the sample. This field of material science where the properties of the varistor are engineered to suit the application is known as Microstructural Engineering of Varistor[55]. A detailed analysis of the literature available is discussed in this section. For microstructural engineering of varistors a thorough understanding of the crystal structure and band structure of the base compound is necessary. Since a major part of this introduction is based on ZnO, the crystal structure and band structure of ZnO are given below in figure**1.7**.

ZnO has a wurtzite structure. In this structure, the oxygen atoms are arranged in a hexagonal close packed type of lattice with zinc atoms present at half the tetrahedral sites. Zn and O atoms are tetrahedrally coordinated to each other. The ZnO structure is then relatively open with half the octahedral sites being empty. There are enough empty sites available to accommodate the dopants which have considerable influence on the nature of defects and mechanism of diffusion of defects in a ZnO structure.

The band gap of ZnO has been found to be 3.3eV. It is known that thermodynamically formed natural defects occupy the donor and acceptor levels within the band gap. The natural defects that are formed during the thermodynamic process are given in figure**1.7**. An understanding of the defect states or rather defect chemistry is very important to successfully engineer the microstructure. Similarly a thorough understanding of the grain boundary is also necessary. The study of the grain boundary is more difficult since the grain boundary itself is a defect between two grains. The microstructure of a varistor is such that the grain boundary has an excess negative charge of acceptor defects that are balanced by equal and opposite positive charge of donor defects that penetrate some distance into the grains and thereby forming the depletion layer.

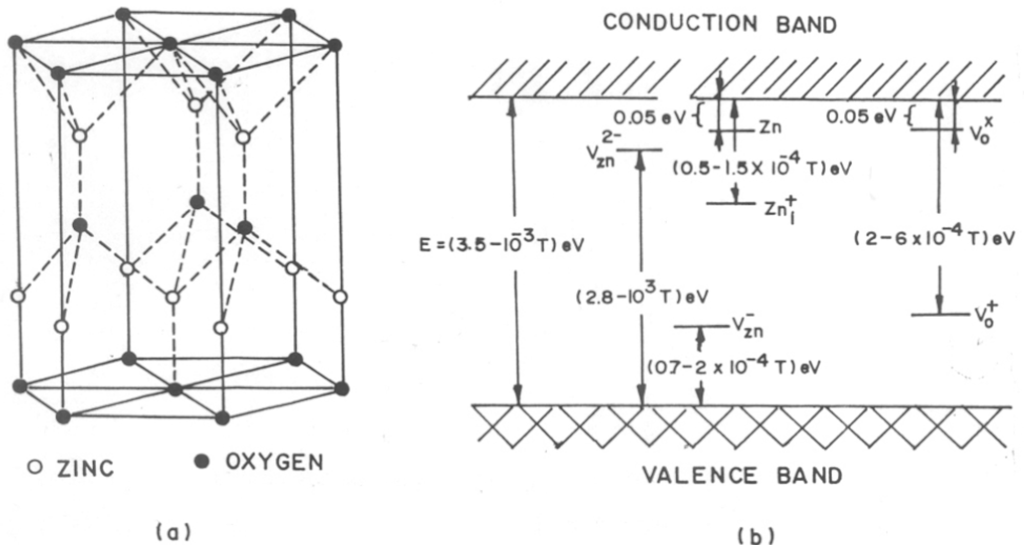

Figure 1.7 Crystal structure and band structure of ZnO

TH-1063
RR 681.586:537(043)
SAN

The important aspects of a grain boundary can be summarized as (a) they have a relatively open structure having characteristic width for easier accommodation of foreign atoms and for relaxation of structure upon doping (b) they provide a rapid diffusion path for ions, especially for anions (c) they have the ability to segregate charges when the ceramic is cooled from the fabrication temperatures (d) the ease of formation of vacancies and interstitials is greater in the grain boundaries.

The ZnO varistor system provides a way to study the effect of dopants on grains, grain boundaries, intergranular layers, etc. This arises from the fact that the current-voltage characteristics of a varistor is microstructure dependent. As explained in section**1.5**, the properties which are grain specific will show up in the "upturn region". Those which are grain boundary specific will appear in the "pre-breakdown region". By monitoring the dopant effects on the upturn and low current regions, it is possible to know whether the dopant is grain specific or grain boundary specific. Combining this knowledge with the defect models for these regions, it can be determined whether the dopants act as donor, acceptor or some cases even both.

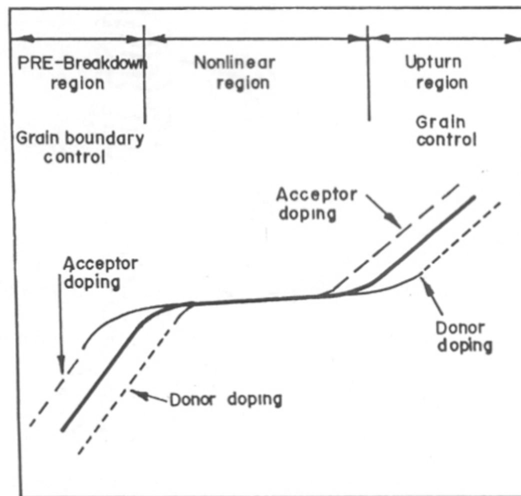

Figure1.8 Effect of donor and acceptor doping on the current-voltage characteristics of a ZnO varistor

Figure**1.8** shows the perturbations of I-V curve as a result of donor or acceptor doping in the grains and the grain boundaries. Consider the upturn region. If the grain impedance is determined by donor doping, the voltage rise will be retarded and upturn will be delayed to higher current densities. On the other hand, if impedance of the grain is increased by acceptor doping the upturn will be at lower current densities. Similar effects are also found at the grain boundaries and is seen at the pre-breakdown region of the current-voltage region. This effect has been experimentally tested[56-59]. These reports represent the effect of addition of Al_2O_3, Li_2O and Na_2O on ZnO varistors. It was seen that, in the prebreak-down region, a monovalent Li acts as an acceptor in ZnO, pushes the I-V curve to the left of the undoped one.(Shown in figure**1.8**). At the same time Al^{3+} as donor in ZnO, pushes the I-V curve to the right. These results point that the leakage current and electrical conductivity are reduced by Li doping and increased by Al doping. Further studies [60,61] found that for Al^{3+}, doping up to a certain level (ie,2000ppm) it acts as a donor in the grain boundary. But with higher concentration of doping it acts as an acceptor. The same behaviour is observed at the upturn region for Al doping. The above set of results indicated that both Al and Li affects both the grain and the grain boundary.

Na doping has a similar[62] effect as Al doping. For smaller amounts, it acts as a donor, but it acts as an acceptor at higher levels of doping. The important aspect about Na doping is that, unlike Al doping, there is no change in the I-V curve in the upturn region. Thus Na is a true grain boundary specific dopant. Also for Na doping, there is no change in the flat middle section of the I-V curve brought about by change in grain size. In the case of Al doping there is indeed a change in grain size, which is reflected on the breakdown voltage.

Gupta[55] have tried to explain the unusual behaviour of the effects of Al, Li and Na dopants on the I-V curve of the varistor characteristics by proposing a defect model. Frenkel disorder[63] is the predominant type of defect in ZnO as the material gets heated. This gives rise to interstitial Zn_i that occupies the available interstitial sites, ie, the octahedral and tetrahedral sites, in the crystal. The Zn_i is a shallow donor ($E_d = 0.05$ eV) and hence readily ionizes.

$$Zn_i \longrightarrow Zn_i^{\bullet} + e' \qquad (1.6)$$

Since the interstitial sites are thus filled with Zn_i, the externally incorporated Al ion will tend to occupy the lattice site as a donor.

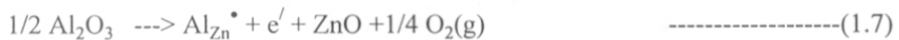

$$1/2\ Al_2O_3 \ \text{--->}\ Al_{Zn}^{\bullet} + e^{/} + ZnO + 1/4\ O_2(g) \qquad \text{-------------------(1.7)}$$

The trivalent Al^{3+} ion replaces a divalent Zn^{2+} ion in the lattice with the liberation of a net electron to conduction band and resulting in the formation of a positively charged $Al_{Zn}^{\bullet}$. As the Al concentration increases, these dopants will try to occupy the Zn_i (ie, interstitials occupied by Zn ions). For this to happen, Al acts as an acceptor

$$1/2\ Al_2O_3 \ \text{--->}\ Al_i^{/} + h^{\bullet} + 3/4\ O_2(g) \qquad \text{-------------------(1.8)}$$

This effect is same in both the grains and grain boundaries and hence the shift in the I-V will be same in both the regions of the curve. Similar effect is reported with Ga^{3+} and In^{3+} dopants[64]. The transition metal oxides have a different kind of effect on the varistor characteristics when added as a dopant. These are generally doped in 0-1 mol% range. Considerable amount of literature is available on the effect of MnO_2, CoO, Cr_2O_3,etc on the varistor characteristics[65-68]. More specifically, they affect the non-linearity of the I-V curve. For example, a simple addition of 0.1 mol% Bi in ZnO gives rise to non-linear behaviour with maximum $\propto$ of 5. But with a further 0.1 mol% addition of Mn and Cu increases the $\propto$ value to 50 and 30 respectively[69,70]. The high $\propto$ value of Mn doped samples are found to be counter balanced by degradation of electrical behaviour which is related to the ability of Mn to adopt several oxidation states(Mn^{2+}, Mn^{3+}, Mn^{4+})[71].

In the case of Cr_2O_3 addition, with very small percentages of dopant (0.1 mol %) there is certainly an increase in the non-linear coefficient [72]. But if large amounts of Cr_2O_3 is added as dopants, it lowers the height of the potential barrier at grain boundaries, increases the leakage current and decreases the $\propto$ values[73].

Another dopant which is used to improve the non-linear behaviour of a varistor is cobalt. There are reports comparing the addition of CoO/ Co_2O_3 in the ZnO varistor system and studying the effect of dopants[74,75]. It is seen that the donor concentration is lowered by increasing the Co dopant concentration. The carrier mobility was found to increase with Co_2O_3 concentration but above 0.5 mol% Co_2O_3 decreased the carrier mobility.

In all the ZnO varistors so far discussed, it was found that oxides of Bi, Pr, Sb as one of the necessary dopants for varistor behaviour. These oxides volatilize at a lower temperature than the sintering temperature of a varistor. These are materials which lead to an effective insulating grain boundary layer which are essential to the varistor behaviour. Hence the varistor dopants can be separated into mainly three different groups. The first group can be called as *Varistor formers*. This group essentially consists of oxides of Bi, Sb, Pr, Pb, etc. These are found to be essential for varistor behaviour. The second group is called the *Performance enhancers*. Their function is to improve the non-linear behaviour of the varistor. These are oxides of Mn, Co, Cr, Ni, etc. The last group of dopants are called as *Performance highlighters*. These dopants improve a specific property of the material like stability, non-linear coefficient etc. This group consists of elements like Al, Na, Li, K, etc. The performance highlighters are added in very small concentrations, usually in the ppm range. The varistor formers are added in comparatively large amount, ie, several mol%. All these studies led to some important rules which are essential to successfully engineer the materials. These rules are summarized below:-

a) The most important rule is that the host material must be a semiconducting material having large enough band gap that allows energy levels to be formed in the forbidden gap, when dopants are added.
b) Polycrystallinity is a necessary condition.
c) The site preference of the dopant ions arise from the localized reduction of free energy.
d) Relative size of the host/guest ions is very important along with their crystal structure.
e) An open crystal structure of the host will allow for better accommodation of guest ions as is found in the case of ZnO.

For example, a larger guest ion (Na) will go to grain boundary and a smaller dopant (Al) can go to both grain and grain boundary. Once the dopant is placed at the grain or grain boundary, it can act as either donor or acceptor. The rules for this aspect is not yet very clear. The above mentioned engineering rules are summarized in Table**1.4**.

There are dopants which changes the grain size distribution and thereby affect the breakdown voltage characteristics of the varistor[76-78]. Generally the dopants which are

found to affect the grain size are Al_2O_3, TiO_2, MgO. In our group at NCL Pune, a detailed study was carried out to find the effect of MgO on the ZnO varistor characteristics. MgO was found to be a grain growth inhibitor. This, in turn, has led to an increase in breakdown voltage of the varistor material of a particular size. Also the addition of MgO improved the microstructure to give a homogeneous distribution. This aspect was checked by impedance analysis also. Similar effect was found in the case of sample doped with Al_2O_3 and SiO_2[79,80]. Doping with TiO_2 increased the grain size[81]. Hence TiO_2 is a grain growth enhancer. This will decrease the breakdown voltage of the varistor. A similar effect of grain growth enhancement was observed when the sample was doped with BaO[82].

Table 1.4 Hierarchy of microstructural engineering

Hierarchy of microstructural engineering
First Level of Engineering
Find dopant which is
1. Grain boundary specific
2. Grain specific
3. Mixed mode
Second level of Engineering
Dopant acts as
1. Donor
2. Acceptor
3.Both/none of the above
Third level of Engineering
Dopant is
1. Lattice site specific/donor or acceptor
2. Interstitial site specific/donor or acceptor
3. Both

Recently Wu *et al* [83] reported the varistor behaviour in ZnO doped with V_2O_5. Here a change of grain growth mechanism from isotropic growth behaviour of pure ZnO to the abnormal growth was observed after doping with V_2O_5. A maximum $\propto$ of 9 was observed with 0.25 mol% V_2O_5. Most importantly there was no Bi_2O_3 as a dopant.

1.9 Processing methods and their influence on varistor properties

A homogeneous distribution of dopants and thereby resultant uniform microstructure is an essential criterion for the reproducibility of varistor characteristics. Hence an understanding of the initial physical characteristics of the green powders, effect of sintering temperature, sintering time, sintering rate, cooling rate, effect of binder concentration, etc. is very

important. Considerable amount of literature data is available on these aspects which were studied on ZnO varistors[84-95]. Various ways of synthesis of complex varistor compositions are available in the literature[96-100]. A homogeneous distribution of composition is needed to control thermal stresses arising from variations in resistance and thereby localized heat buildup. For achieving a uniform sintered microstructure, a uniform green microstructure of uniformly packed particles with a narrow size distribution is needed.

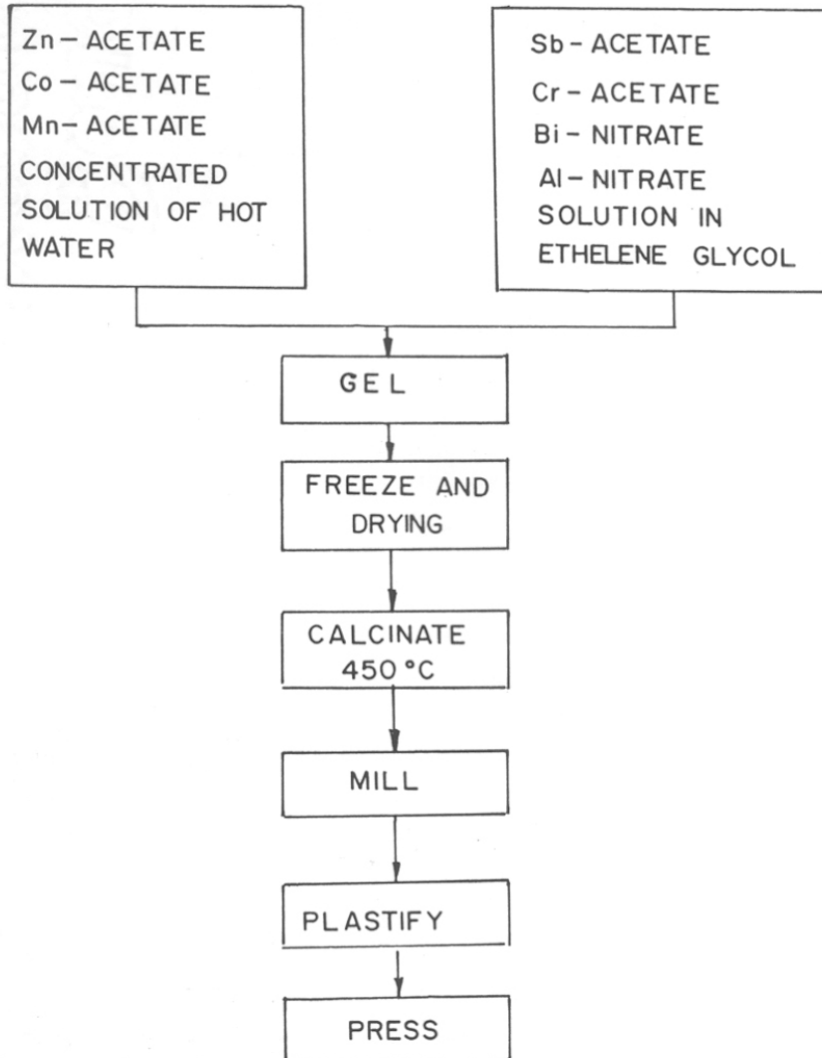

Figure 1.9 Schematic diagram of sol-gel technique (99)

One method is to synthesize uniform monosize, monodisperse, equiaxed particles. Aqueous precipitation of spherical ZnO particles is one such successful method[100]. These studies exhibited improved properties over those fabricated by conventional ball milling. Another method is the sol-gel process[98]. This process is carried out using inexpensive source materials such as acetates and nitrates. A block diagram of the sol-gel process as described by Hohenberger *et al* [99] is given in figure**1.9**.

Varistor ceramics made from sol-gel powders can be sintered at lower temperatures. The sol-gel prepared varistors exhibited a better non-linear characteristic, i.e. large non-linear coefficient. Also the breakdown field of the sol-gel sample is much higher compared to the ball milled samples. This is due to the fact that the sol-gel material has more varistor-active grain boundaries as a result of more homogeneous distribution of dopants. These powders have a better energy handling capability because in these materials there are more varistor active paths. Hence these materials are generally used for high voltage applications.

Most importantly, these preparations yielded final grain sizes in the range 3-4 μm compared to ≅ 20μm for the conventionally prepared ZnO varistor. The high electrical breakdown and ability to withstand high powers enabled the researchers to manufacture small varistor. So these chemically prepared powders are expected to play a major role in the production of chip-varistors, multilayer varistors and surface mounted devices [101-103].

There are other methods also to produce uniform fine grained particles. Some of them are Urea process[104], Microemulsion techniques[105], Amine process[106], etc. All these processes gives rise to uniform, dense and nanosized particles having high surface area and surface free energy which can be sintered to near theoretical density at lower sintering temperature and time.

The electrical properties are dependent on the sintering temperature, time, atmosphere, cooling rate, etc[107-115]. Improvement of the varistor properties have been found to occur by hot isostatic pressing technique. The electrical properties are found to improve by increasing the sintering temperature and time, because this makes most of ZnO-ZnO junctions into direct contacts and reduce interface energy. It is also found that uniformity of trapping conductance (due to acceptors and donors) is enhanced by increasing the sintering time and temperature. If the sintering temperature is increased above the optimum

temperature, volatilization of low melting point materials (Bi_2O_3, Sb_2O_3) occurs within the grain boundaries. The donor concentration is also increased in the ZnO grains due to increasing dissociation of ZnO. These will change the non-ohmic nature of ZnO varistors to an ohmic one.

1.10 Energy barrier, electronic states and their detection.

Non-linearity of a varistor is a grain boundary phenomenon where an energy barrier to the motion of majority carriers (i.e., electrons) exists in the depletion layers of the adjacent grains [116,117]. Schottky barrier is found to be the most likely barrier existing at the grain boundary. The negative surface charge at the grain boundary interface (electron traps) are compensated by the positive charge in the depletion layer in the grain on both sides of the interface.

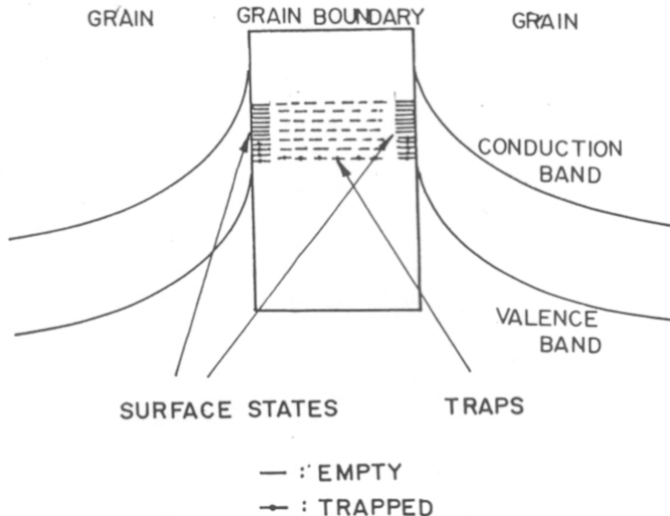

Figure 1.10 Grain-grainboundary-grain model of a varistor.

Figure**1.10** represents the typical energy level diagram of a ZnO-ZnO grain boundary. Electron traps are important in the formation of energy barriers. There are two types of electron traps; traps located at the ZnO-ZnO grain boundaries are known as interface traps and those located within the bulk of ZnO grains are known as bulk traps. Interface trapping mechanism[118,119,120] is generally considered as the mechanism giving rise to the double Schottky barriers at the grain boundaries. Electrons trapped in the interface states are compensated by positive, ionized shallow donors and donor like traps within the depletion

region of the junction. These electron traps are atomic defects, either native to the semiconductor or arising from impurities.

One of the methods of detecting the interface electronic states is by observing the recovery of the non-equilibrium grain-boundary barrier capacitance[121]. These results indicated that a large density of electron traps is observed 0.6 to 0.7 eV below the conduction band edge in ZnO varistors. The most commonly used techniques are DLTS (Deep level transient spectroscopy)[122] or ICTS (Isothermal capacitance transient spectroscopy)[123]. From all these measurements large density of interface states were observed 0.9-1 eV[124] and 0.6-0.7eV[125] below the conduction band edge. However, it must be remembered that these studies still donot give a clear idea about the origin of interface states. The possible candidates for the origin of interface states are found to be absorbed excess oxygen[126,127], impurities in the form of transition metal ions(Mn,Co)[128-130], dangling bounds of ZnO lattice[131], and strain effects caused by large ions such as Bi and Pr in ZnO[132]. The study of these defects is unclear because of many factors like different grain sizes, density, crystalline phases, diffusion of ions, microdefects,etc, which are present in a varistor.

The role of grain boundary oxygen in the formation of trap level has been proved by X-ray photoelectron spectroscopy[133]. These studies even indicate that the role of Bi as varistor former may be limited to supplying excess oxygen to the grain boundaries. Measurements using Auger electron spectroscopy[134] do agree similarly to the above conclusions.

Capacitance-voltage (C-V) analysis is another important tool to study a varistor. The donor density, the interface trap density, and Schottky barrier height can be calculated from the C-V data using the relations

$$(1/C - 1/2C_o)^2 = 2(\phi_b + V) / q\varepsilon N_d \qquad \text{------------------(1.9)}$$

C_o and C are the capacitance per unit area of a grain boundary biased with zero and V volts, q the electron charge, ε the dielectric constant of the grains, N_d the donor concentration of the grain, ϕ_b- the barrier height of grain boundary. The interface trap density

$$N_t = 2\,(2\varepsilon\, \phi_b N_d / q)^{1/2} \qquad \text{------------------(1.10)}$$

These experimental data are then correlated with the processing methods and can be used to modify successfully the material.

1.11 Degradation behaviour

Zinc oxide varistors exhibit a degradation phenomenon when continuously stressed by external field. Degradation has been reported to be related to the deformation of Schottky barrier [135-145]. The degradation mechanism has been studied under a.c, d.c and pulsed electric fields and several theories have been proposed[146,147], (i.e., electron trapping, dipole orientation, ion migration and oxygen desorption,etc.). The degradation phenomenon arising out of migration of ions in the depletion layer in grain boundary is the currently accepted model. The concept of this model is that the depletion layer comprising the barrier consists of two components; a stable component consisting of spatially fixed positively charged ions and a metastable component consisting of mobile positively charged zinc interstitials. Since all the octahedral and half the tetrahedral interstitial sites are empty in the ZnO structure, zinc interstitials rapidly migrate within the structure via vacant interstitial sites. Both electric field and elevated temperature provide necessary driving force for the interstitial migration in the depletion layer. These positively charged $Zn_i^{\bullet}$ interstitial and a negative charge ($V_{Zn}^{/}$) combine and two neutral defects are(Zn_i^{x} and V_{Zn}^{x}) formed at the grain boundary. These neutrals Zn_i^{x} keep accumulating as the concentration of compensating charges are reduced in equal proportion in the depletion layer as well as at the grain boundary interface. This process is reversible with field. The degradation and stability of the varistor can be controlled by heat treatment. The key factor in restoring the stability by heat treatment is the formation of stable ZnO lattice at the grain boundary at the expense of the zinc interstitials in the depletion layer. Varistor degradation can be minimized by two methods:

(a) Annealing induced stability: The zinc interstitials in the depletion layer are permanently out diffused via thermal anneal[148,149].

(b) Chemically induced stability: The strategy here is to incorporate an amphoteric dopant such as sodium or potassium in the ZnO lattice. The amphoteric dopants can occupy both the lattice and interstitial sites. By occupying interstitial sites, the dopants will first block

the formation of zinc interstitial in the available sites, and second they will prevent the migration of zinc interstitials via available sites[150].

1.12 Theoretical models for electrical conduction.

The physics of varistor has been of great interest to various researchers and a large number of models have been proposed to explain the high conduction in the non-linear region of the varistor. These models have their origin in the work on germanium and silicon based semiconductors[151,152]. Considerable progress has been made in these models which tried to take into account various contributions to the varistor phenomenon. Table**1.5** shows the progress in research in the understanding of conduction mechanism in varistors along with the relevant references.

Table 1.5: Theoretical models evolved in the last 25 years

	Model	Ref.no.	Year
1.	Space-charge-limited current (Matsuoka)	35	1971
2.	Tunneling through schottky barriers (Levine)	118	1975
3.	Tunneling through a thin layer (Levinson and Philipp)	156	1975
4.	Tunneling through schottky barriers(Morris et al)	157	1976
5.	Tunneling through schottky barriers with heterojunctions (Emtage).	158	1977
6.	Tunneling through schottky barriers with heterojunction (Eda)	159	1978
7.	Tunneling through homojunctions (Einziger)	160	1978
8.	Tunneling through schottky barriers (Hower)	161	1979
9.	Hole assisted tunneling through Schottky barriers (Mahan)	162	1979
10.	Bypass effect at heterojunctions (Eda)	163	1982
11.	Hole-induced breakdown (Pike)	164	1984
12.	Bypass effect at heterojunctions (Levinson and Philipp)	165	1986
13.	Hole induced breakdown (Blatter and Greuter)	166	1986

Initially, avalanche breakdown was considered as a possible process. But the current-voltage characteristics associated with this process are extremely sharp. i.e., $\propto$ value>1000. Also these are characterized by a positive temperature coefficient of breakdown voltage. but the ZnO varistors exhibit a negative temperature coefficient of breakdown voltage. The theory of Avalanche breakdown was discarded[153]. Matsuoka[35] tried to explain the high non-linear current-voltage phenomenon by using space charge limited current(SCLC). The space charge limited (SCL) process describes the conduction within an insulator provided with ohmic contacts[154]. It is known that SCLC will occur at an electric field of about 10^4 V/cm[155]. Segregation layers in ZnO, consisting of many oxides providing electron traps, cause an electric current to flow at the above field. This theory is applicable for the explanation of the effect of additives on the non-ohmic property. But the theory is unable to explain the small temperature dependence of current-voltage characteristics in the highly-non-ohmic region.

Levinson and Philipp[156] tried to explain the behaviour by a thermally simulated and tunneling currents. According to this model, the highly non-ohmic property observed in the voltage region above the breakdown voltage is consistent with the Fowler-Nordheim tunneling process which is represented by

$$J \propto \exp(-\gamma / V) \quad \text{------------------ (1.11)}$$

where J is the current density and V the field. The conduction mechanism in the voltage region below the breakdown voltage follows the thermally activated Frenkel-Poole law or the Schottky barrier law of the form

$$J \propto \exp[-(E_i - \beta V^{1/2}) / KT] \quad \text{--------------------(1.12)}$$

where E_i is the activation energy. These theories were able to explain the voltage-current characteristics and their temperature dependence. But these theories are unable to explain the effect of additions, and asymmetrical degradation of voltage-current characteristics. These inadequacies are due to the fundamental assumption for the thickness of the intergranular layer, which is assumed to be infinitesimally thin or negligible.

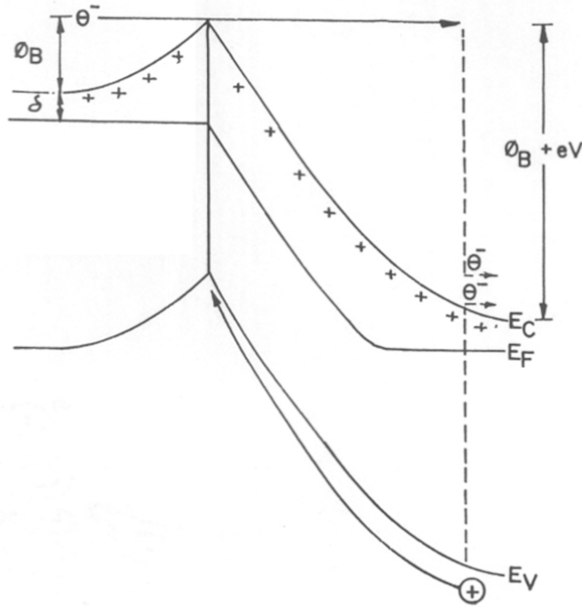

Figure 1.11 Energy band diagram near a grain boundary under applied voltage.

At present the model which is based on hole induced breakdown mechanism [162-167] is widely accepted. Mahan et al , Pike et al argued that none of the above mentioned mechanism can realistically account for the extremely high non-linearity observed in ZnO varistors at small voltage (~3.5V) per grain boundary. They suggested that the varistor breakdown mechanism is controlled by hole creation in the forward bias side of the double Schottky barrier. The creation of holes is due to interband impact ionization in the positively biased depletion region and is shown schematically in figure **1.11**.

E_c, E_v and E_F are the conduction band, valence band and the quasi-fermi level. In the thermionic emission model[168], most of the electron that cross the grain boundary rapidly lose their excess energy by optical phonon scattering and remain close to the depletion region. In this model it is assumed that a small fraction of electrons can penetrate the depletion region without significant energy loss. For voltage per grain boundary

$$eV + \phi_B > E_c - E_v = 3.2\text{eV} \qquad \text{------------------(1.13)}$$

Some of the electrons can impact ionize electrons from the valence band, creating holes which move towards the electron trapped at the grain boundary. These holes reduce the net

excess charge at the grain boundary and cause the barrier height to decrease. This theory has been able to explain the high non-linearity of the ZnO varistor. Also impact ionized holes have been able to explain the unusual phenomenon of negative differential capacitance observed in ZnO varistor. The presence of these holes were proved by experiments done using electroluminescence[169]. The models acknowledge thermionic emission and tunneling as the major transport mechanisms for electronic conduction.

1.13 Impedance analysis.

Impedance spectroscopy is a valuable technique used for the characterization of inhomogeneous (insulating, electrical and magnetic) materials exhibiting granular structures. To differentiate between the varying contributions from grains, grain boundaries, intergranular layers and electrode interfaces, ac impedance spectra are often used with great success. In favourable cases, the difference in impedance responses originating from the different regions of the granular ceramics can be explained using RC parallel and series circuit elements. Any intrinsic property that influence the conductivity of an electrode-material system can be studied by Impedance spectroscopy. Most common method of impedance analysis is to measure impedance directly in the frequency domain by applying a single frequency voltage to the interface and measuring the phase shift and amplitude (real and imaginary parts) of the resulting current at that frequency. This way the measurements are done in a large range of frequencies (few Hz to Giga Hz).

In impedance spectroscopy, a time dependent voltage $E(\omega) = \delta E \, Sin(\omega t)$ is applied across the ceramic sample. A sinusoidal current with the same angular frequency will then flow through the sample and the response is characterized by a complex impedance Z. Z will be a function of ω. The real and imaginary parts of their complex impedance Z ($Z^{/}$ and $Z^{//}$) can be recorded for a large range of frequencies using the available impedance analyzer. When the data points are plotted in complex impedance plane ($Z^{/}$ Vs $Z^{//}$), the data points are usually distributed along the arc of circles as shown in figure **1.12**. An equivalent circuit based on a serial assembly of parallel resistances and capacitances can be then used to simulate the electrical behaviour. Usually the values of the resistances and capacitances of each cell and therefore each arc can be assigned to a specific part of the ceramic sample -the grain interiors, grain boundaries, metal-ceramic interfaces,etc. The chord of each arc of a

circle is the resistance of that individual part of the ceramic. The time constant τ corresponding to each arc obeys the relation $\omega^*\tau = 1$, where ω^* corresponds to the top of the semicircular arc it corresponds to. The time constants corresponding to grains, grain boundaries, interfaces differ by one order of magnitude and hence well distinguished arcs corresponding to each part of the ceramic are usually obtained. A careful selection of the electrode is necessary to avoid the presence of an arc of a circle in the impedance spectrum which can interfere with the grain-boundary contributions.

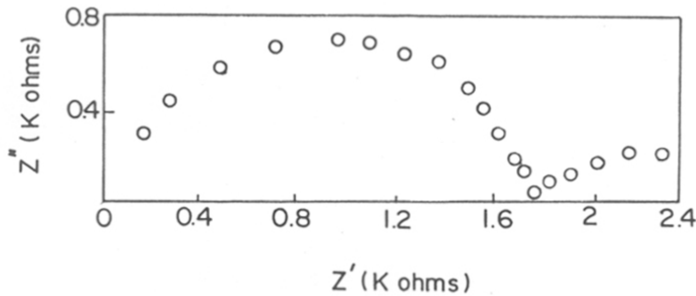

Figure 1.12 Typical impedance plot

The lumped-parameter/complex plane analysis have been found to be an important technique to study a heterogeneous system[170]. Another important parameter found to be very important is the depression angle θ. Its presence indicates non-Debye (non-ideal) relaxation. A depression angle is defined when the centre of semicircular relaxation lies below the X-axis instead of on the X-axis. The depression angle θ observed in the Z plane is related to the degree of uniformity/non-uniformity in reactance's for the associated relaxation resulting in an average time constant.

Similarly the capacitance vs frequency, admittance vs frequency and other plots available from this technique give lot of information on the characteristics of the ceramic materials. Alim *et al* and others[171-176] have done extensive work on the impedance analysis on ZnO varistors. These measurements were able to prove the homogeneity of the material and other aspects like activation energy of the grains, grain boundaries, metal ceramic interfaces, etc. This technique is a successful experimental method to investigate the structural

uniformity, degradation, time dependent processes, etc. in these heterogeneous materials-based devices. Extensive data is available on how impedance analysis is used to assess the influence of dopants on varistor properties[177], trapping phenomenon[178], sintering behaviours[179] etc in the literature.

1.14 Search for new varistors

Varistors are protective devices used in parallel with electronic circuits to protect these circuits from spurious voltage surges and transients. In an earlier section it was explained how the surge arrestors have evolved from the gapless arrestors to SiC varistors and then to ZnO varistors. ZnO varistor had a superior non-linear characteristic ($\propto \sim 50$). $SrTiO_3$ is one of the new varistor materials which exhibited relatively good varistor phenomenon($\propto \approx 20$)[180,181]. Commercially, ZnO varistors are mounted in surge arrestors and absorbers. $SrTiO_3$ varistors are used in micromotors.

Protection against transient voltage surges requires varistors with appropriate voltage and frequency characteristics. ZnO varistors are used for high-amplitude and low-frequency voltage surges, such as transient voltage surges (e.g.: transient line voltage and switching surges). $SrTiO_3$ varistors are used for medium amplitude and high-frequency transients such as interference generated by electric motors.

Modine and Hyatt[182] reported a new varistor made of a composite structure of semiconductor, conductor, insulator and a binder. Carbonyl nickel was the conductor, silicon carbide the semiconductor, fumed silicon dioxide the insulator and silicon rubber is the polymeric binder. It gave a non-linear coefficient $\propto$ of 10, and the breakdown voltage was usually in the range 1-10 KV/cm. In this particular material, no sintering was done. The low capacitance of the material is suited for use as high-frequency antenna protection.

A well known trend in recent times is the miniaturization of electronic circuits. But the ZnO varistors have an average breakdown voltage of 3V per grain boundary. Hence for low voltage applications, ZnO varistors are not preferred since there is a limit to the thickness that can be reduced for the sample. Lot of experimental work has been done to make thin film varistors[183,184], multilayer varistors[185] etc.

TiO_2, which is a wide band gap semiconductor, was chosen as the base material in an attempt to develop new varistors. Yan and Rhodes[186] first reported this material in 1982. The varistor characteristics are due to two different kind of dopants. The first group of dopants is used to decrease the lattice resistivity of TiO_2. This dopant group consists of elements with a 5^+ valence (Nb,Ta) to donate extra conduction electrons and with similar ionic radii to easily get into TiO_2 lattice. The second group of dopants consists of divalent cations with large ionic radii (Ba,Sr, Ca). These dopants segregate at the grain boundary to relax the large elastic energy. The segregation of divalent cations increases the grain boundary resistivity because pentavalent donors (Nb or Ta) are locally compensated by the divalent acceptor (Ba,Sr,or CA). This in turn will lead to an effective depletion layer. A maximum $\propto$ value of 7 was observed.

Wu et al have done considerable amount of research on TiO_2 varistors doped with PbO, Ba, Bi,etc [187-189]. The maximum value of $\propto \approx 9$ was found in these experiments. But the most important aspect in these studies is that the breakdown voltage per grain boundary is considerably lower than that obtained for ZnO varistors. For Ba, Bi and Nb doped TiO_2 varistors a value of 0.8 V per grain boundary was found. This small value of breakdown voltage is of considerable importance in applications related to microelectronics.

Similarly,SnO_2 is also a wide band gap semiconductor, this material was also investigated as a possible candidate for a good varistor base material. Pianaro et al [190] tried to develop new varistor based on SnO_2. SnO_2 doped with Nb, Co and Cr were found to have relatively high non-linearity coefficient ($\propto \approx 40$) and also a high breakdown voltage (4000V/cm). These characteristics make these materials a good candidate to replace ZnO varistors. Also the absence of any volatile dopants like Bi_2O_3 may give a new varistor with better degradation behaviour than the ZnO varistors.

Another low-voltage varistor was recently reported which was based on zinc antimony spinel ($Zn_7Sb_2O_{12}$) [191]. These varistors have breakdown voltages in the range 3-20 V and $\propto$ in the range 7-15. In this case the control over the mixed valence states of antimony is very important to attain high non-linear values.

1.15 Aim of this work

(1) Attempt was made to synthesize new voltage sensor materials based on TiO_2 to obtain materials with low breakdown voltage. TiO_2 was first doped with Nb^{5+} to increase the conductivity of the TiO_2 lattice. then Sr and Bi were added to create an effective grain boundary. A systematic study was carried out on this composition by using I-V characteristics, SEM, X-ray diffraction and Impedance analysis. The effect of other dopants like Ba or Ca in place of Sr was also analyzed. The effect of doping of Mg^{2+} in place of Sr^{2+} on the varistor properties was also studied. Another aim was to find the effect of chemical synthesis on the varistor characteristics. The properties of the chemically prepared samples were then compared with the conventionally prepared samples.

(2) Attempt was made to synthesize a new varistor composition based on SnO_2. There were two reasons for selecting SnO_2 as the base material. First one is that SnO_2 is a wide band gap semiconductor. Second one is that it has a rutile structure similar to TiO_2. Hence a comparison of the properties between TiO_2 and SnO_2 varistors will be possible. SnO_2 doped with Nb, Co and Al was prepared by the conventional ceramic route. Their electrical characteristics were studied using I-V measurements and impedance analysis. SEM analysis and X-ray diffraction analysis were also characterized to find the microstructural and phase studies. The effect of different concentrations of one of the dopants Co was also studied. Similar to TiO_2 voltage sensors, a chemical method of synthesis was done to get uniform distribution of dopants in SnO_2. These samples were then analyzed using current-voltage characteristics, SEM and XRD. These results were then compared with the results obtained from the conventionally prepared samples.

Hence the primary aim of this work is to search for new varistor materials/compositions which give a relatively good non-linear behaviour. The effect of chemical synthesis on the uniform distribution of dopants and thereby on the final properties of the voltage sensors were analyzed.

1.16 Titanium dioxide

Titanium dioxide exists in three crystalline modifications, rutile, brookite and anatase. At elevated temperatures. titanium dioxide exists in the rutile form. Other phases of titanium

dioxide are converted to rutile when heated to temperatures between 700 and 920°C. This transformation is not reversible. The crystal structure of rutile TiO_2 is given in figure**1.13**.

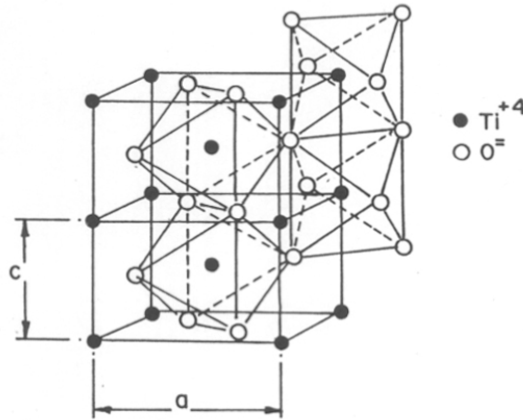

Figure 1.13 Crystal structure of rutile TiO_2

The oxygen ions are arranged in the form of somewhat distorted octahedra. Each octahedron shares an edge with the adjacent members of the chain. Alternatively, the crystal structure mat be visualized as chains of ions -O-Ti-O-O-Ti-O. All chains in the same layer are parallel and the chains in adjacent layers are perpendicular to one another and to the c-axis. The unit cell of rutile is tetragonal. Literature data is available[192,193] on the cell parameters which gives the values a= 4.594±0.003A°, c = 2.959±0.002 A°, c/a =0.6441.

A sketch of the energy band structure of pure stoichiometric TiO_2, based on a tight binding approximation, is given in figure**1.14**. The results of the theoretical calculations show that TiO_2 is a semiconductor with a 3eV energy gap separating the filled oxygen 2p band from the empty Ti 3d band. Optical absorption and photoconductivity experiments carried out on a pure, stoichiometric single crystal TiO_2 gave an absorption edge at 3.05eV. This is the energy gap between the oxygen 2p band and titanium 3d band. The intrinsic activation energy of TiO_2 is 1.5eV. TiO_2 need not be contaminated with transition metal ions in order to reduce the activation energy of free carriers. This is because Ti^{4+} itself is a transition metal ion, and it has another valence state, Ti^{3+}, which is easily excited. The presence of any

foreign ion of higher valency (>4+) in a $Ti^{4+}O_2$ can lead to presence of one or more Ti^{3+} ions, to preserve charge neutrality of the crystal.

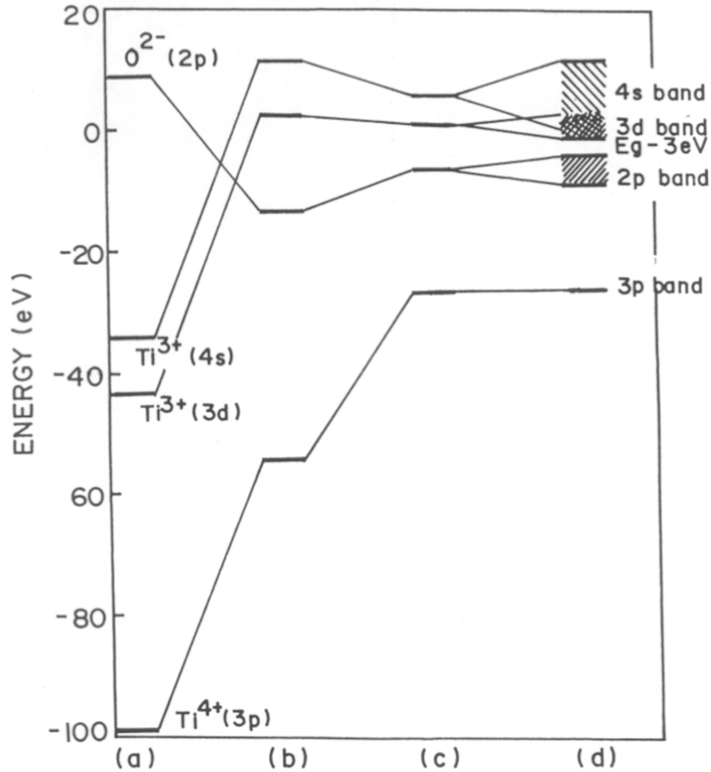

Figure 1.14 Energy band structure of pure, stoichiometric TiO_2 (a) Free ion energies (b) effects of Madelung potential (c) Screening and covalent effects (d) bandwidth effects.

When TiO_2 is reduced, a stoichiometric excess of Ti is created. This reduction provides either oxygen vacancies or titanium interstitials. Since the rutile structure is loosely packed, titanium interstitials are commonly found. A Ti interstitial has four extra electrons. Only one electron is bound to the interstitial [Ti^{3+}], but the remaining three are bound on nearest neighbor Ti sites. Once again, the binding energies can be expected to be smaller, at least for the first two or three electrons. Thus a Ti interstitial acts as a quadrupole donor.

The various experimental techniques[194,195] have concluded that non-stoichiometric rutile [TiO_{2-x}] is a metal excess n-type semiconductor. The experimentally found energy gap (≈3.1eV) and the loosely packed rutile structure of TiO_2 are thus good criteria to be used as

a varistor base material. The large band gap and the crystal structure of TiO_2 allow us to dope the materials. These properties are found to be useful in making TiO_2 a potential sensing materials for reliable detection and satisfactory monitoring of CO and H_2[196].

1.17 Tin dioxide

Tin dioxide (SnO_2) is also n-type wide band gap semiconductor (3.6eV) with the same rutile structure as TiO_2 [197,198]. SnO_2, with similar properties as TiO_2, is widely used in gas sensor[199]. Polycrystalline thin films of SnO_2 are used for the production of resistor, transparent electrodes [200], transistors, antistatic coatings, etc[201]. SnO_2 crystallizes with tetragonal rutile structure with space group D4h14 ($P4_2/mnm$).The rutile structure of SnO_2 is similar to that given in figure[1.13]. Each tin atom is at the center of six oxygen atoms placed approximately at the corners of an equilateral triangle. Thus, it is the structure of 6:3 coordination. The lattice parameters are a=b= 4.737A° and c = 3.185A°. The electrical and optical properties of SnO_2 are similar to TiO_2 and hence it will not be discussed here.

1.18 Application of Varistors.

The varistor is mainly used as a surge suppresser. Usually they are connected in parallel to the electronic circuit that is to be protected. This is done as shown in figure **1.15**. Varistors are selected in such away that their breakdown voltage is just below the limiting voltage of the electronic components. At ordinary working voltages of the circuit(load), the varistor is in its pre-breakdown or low-current region. Hence it acts as a high resistor. When the voltage spike occurs, the varistor conducts heavily since the varistor is now in its non-linear region. The surge is bypassed through the varistor and the circuit components are saved from the voltage surge.

For many years, the varistor have been in use to regulate transient voltage surges. Initially selenium rectifiers were used as varistors. These were later replaces by single-crystal silicon devices or avalanche Zener diodes for low voltage applications and SiC and ZnO varistors for high voltage applications. ZnO varistors are the most commonly used varistors. They account for 80% of the market value. $SrTiO_3$ is the new varistor in this group which is produced in a large scale commercially.

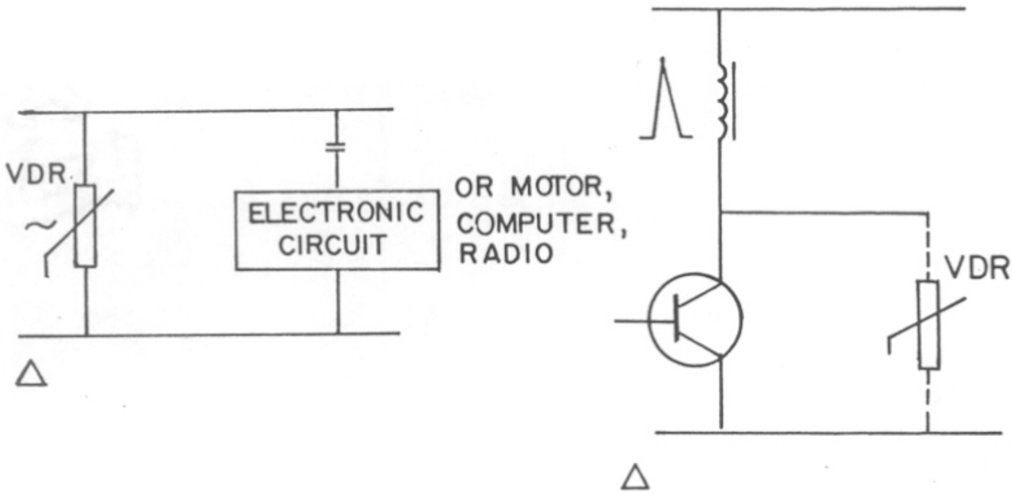

Figure 1.15 Varistor connected as a protector in an active circuit

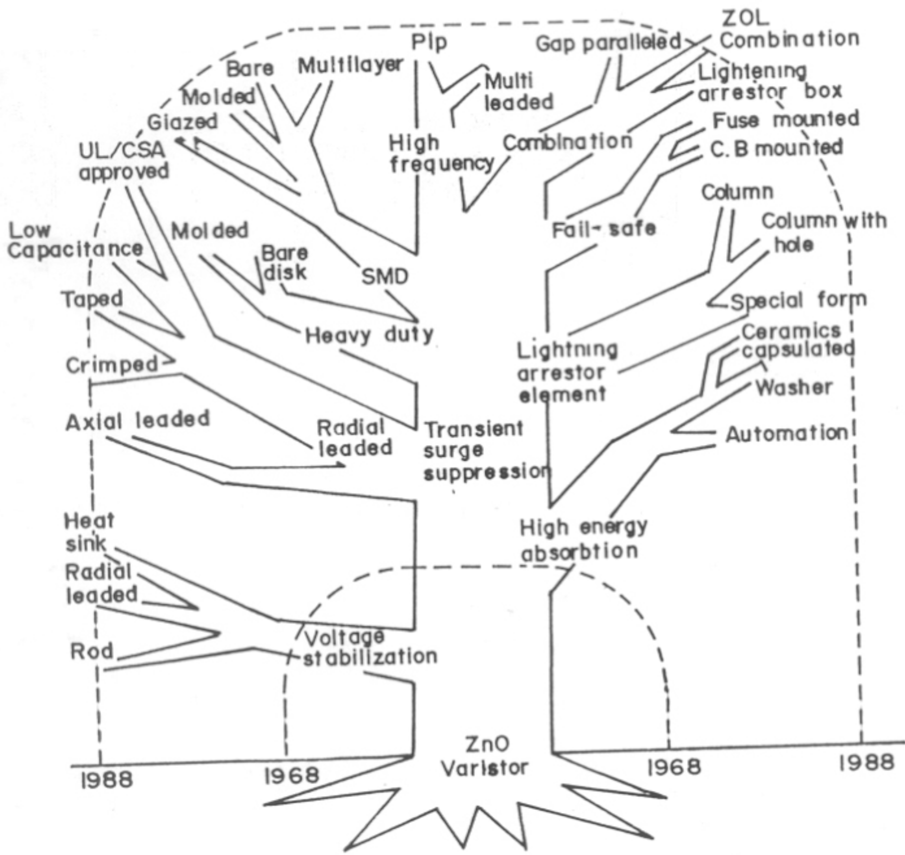

Figure 1.16. Different applications of a varistor

The areas of application of varistors are manifold. Different application areas of varistors are given in the form a tree in figure**1.16**.

1.19 Varistor research and market analysis

Many materials science groups are doing extensive research work on the preparation and characterization of ZnO and other new varistor materials. Many industries like General Electric, Matsushita,etc are producing varistors on a commercial scale. These industries have R&D's which are pursuing the basic research on the varistor phenomenon. Siemens, Thomson, NEC,etc are the other major global players in the international varistor market. Japan has produced 1.9 billion varistors annually since 1991.

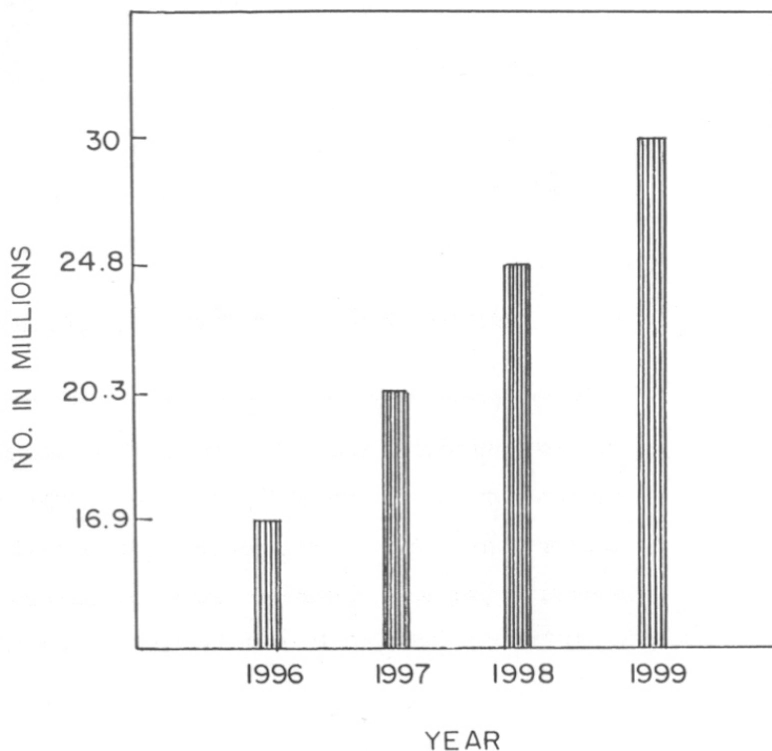

Figure 1.17 Histogram representing the number of varistors used in India(202).

In India, there are few laboratories which are doing varistor research. RRL Trivandrum, BARC Bombay, IISc Bangalore, IIT Bombay are among the few institutions working in this area other than NCL Pune. Phillips India, Elpro, Crompton Switch gears Nasik are the very few industries which are commercially producing the varistors.The demand for these

varistors is expected to increase because of implementation of safety measures and product liability laws for electronic appliances.

According to the Philips market study, the forecast for low voltage varistors in India are improving each year and the projected market both in terms of Quantity and cost are given in Figure[1.17]. Detailed information about the types of varistors manufactured by Philips India is given in their manual [202].

References

1. W.D.Kingery, H.K.Brown and D.R.Uhlmann., "Introduction to ceramics", 2nd edition, A Wiley-Interscience publication (1976).
2. D.Segal., "Chemical synthesis of advanced ceramic materials" in chemistry of solid state materials, Vol.1, edited by A.R.West and H.BAxter, Cambridge University press(1989).
3. "Ultrasonic processing of Advanced ceramics", edited by J.D.Mackenzie and D.R.Uhlrich, A Wiley-Interscience publication (1988).
4. "Advanced ceramics", edited by E.C.SubbaRao, Indian Academy of Science, Bangalore (1987) (check).
5. E.G.Spencer, P.V.Lenzo and A.A.Ballman, in "Dielectric materials for electrooptic and ultrasonic device applications"., *Proceedings IEEE*, **55**, 2074(1967).
6. T.G.Reynolds and R.C.Buchanan., "Ferrite (magnetic) ceramics" in Ceramic materials for Electronics., 2nd Edition, Edited by R.C.Buchanan, Marcel Dekker Inc, NewYork.
7. W.L.Wilkinson., "Chemistry of nuclear fuel cycle" in Energy and Chemistry, Edited by R.Thomson, p164, Royal Society of Chemistry, London(1988).
8. E.M.Briscoe, "The use of advance ceramics in engines" in Chemistry and Industry, p641, (1986).
9. Annual Mineral Review, *Amer.Ceram.Soc.Bull.*, **73**, 73(1994).
10. Gilbert Goodman., "Ceramic capacitor materials" in Ceramic materials for Electronics., 2nd Ed., Edited by R.C.Buchanan., Marcel Dekker Inc., NewYork.
11. W.J.Lackey, D.P.Stinton, G.A.Cerny, A.C.Schaffhauser and L.L.Fahren- bacher., *Advanced Ceramic materials.*, **2**, 24(1987).
12. G.Geiger., *Amer.Ceram.Soc.Bull.*, **73**, 57(1994).
13. R.C.Buchanan., Ceramic materials for Electronics, 2nd Ed., Edited by R.C.Buchanan., Marcel Dekker Inc., NY.
14. A.K.Maurice and R.C.Buchanan, *Ferroelectrics*, **74**, 61(1987).
15. J.F.Scott and C.A.Raz de Aranjo, *Science*, **246**, 1400(1989).
16. W.Werrring, M.Schnoller and H.Wahl, *Ferroelectrics*, **68**, 145(1986).

17. W.Heywang., *J.Mater.Sci*., **6**, 1214(1971).

18. S.M.Park and D.A.Payne., *Amer.Ceram.Soc.Bull*., **58**, 732(1979).

19. K.Uchino., *Amer.Ceram.Soc.Bull*., **65**, 647(1986).

20. B.Huybrechts, K.Ishizaki and M.Takata., *J.Mater.Sci*., **30**, 2463 (1995).

21. P.Duran and C.Moure., *J.Mater.Sci*., **20**, 827(1985).

22. A.Amin., *J.Amer.Ceram.Soc*., **72**, 369(1989).

23. R.E.Newnham., *Rep.Prog.Phys*., **52**, 123(1989).

24. K.Uchino., *Mat.Res.Soc.Bull*., **XVIII**, 42(1993).

25. G.Haurtling and C.Land., *J.Amer.Ceram.Soc*., **54**, 1(1971).

26. K.Terabe, N.Iyi and S.Kimura, *J.Mater.Sci*., **30**, 1993(1995).

27. A.Goldman, *Modern Ferrite Technology*, p157, (Van Nostrand Reinhold, NewYork) 1990.

28. P.S.Anil Kumar, J.J.Shrotri, S.D.Kulkarni, C.E.Deshpande and S.K.Date, *Mater.Lett*., **27**, 293(1996).

29. C.R.Hendricks, V.W.R.Amarakoon andD.Sullivan., *Ceramic.Bull*., **70**, 817(1991).

30. W.S.Young and S.H.Knickerbocker, in Ceramic materials for Electronics 2nd Ed., Edited by R.C.Buchanan, Marcel Dekker Inc., NewYork.

31. Y.Sugawara, K.Onitsuka, S.Yoshikawa, Q.C.Xu, R.E.Newnham and K.Uchino, *J.Amer.Ceram.Soc*., **75**, 996(1992).

32. D.C.Hill and H.L.Tuller., Ceramic materials for electronics, 2nd Ed., Edited by R.C.Buchanan., Marcel Dekker Inc., NewYork.

33. N.Ichinose, *Advanced Ceramics*., p27(1988) Edited by S.Saito, Oxford University press and Ohmsha Ltd.

34. M.Ura, "Ceramic substrates"., in *Fine Ceramics*., p243., Edited by S.Saito., Elsevier, NewYork, 1988.

35. M.Matsuoka, *Jpn.J.Appl.Phys*., **10**, 736(1971)

36. T.K.Gupta, *J.Amer.Ceram.Soc*., **73**,1817(1990).

37. M.Bartkowiak, M.G.Comber and G.D.Mahan., *J.Appl.Phys*., **79**, 8629 (1996).

38. R.Einzinger, *Annu.Rev.Mater.Sci*., **17**, 299 (1987).

39. T.Miyoshi, K.Maeda, K.Takahashi and T.Yamasaki, p309, in *Advances in ceramics*, Vol.**1**, Grain boundary phenomena in Electronic ceramics, edited by L.M.Levinson and D.Hill, American ceramic society, Columbus, OH, (1981).

40. A.T.Santhanam, T.K.Gupta and W.G.Carlson, *J.Appl.Phys.*, **50**, 852 (1979).

41. H.R.Philipp and L.M.Levinson, *J.Appl.Phys.*, **50**, 383 (1979).

42. T.K.Gupta, M.P.Mathur and W.G.Carlson., *J.Electron.Mater.*, **6**, 483 (1977).

43. M.Tao, B.Ai, O.Dorlanne and A.Loubiere., *J.Appl.Phys.*, **61**, 1562 (1987).

44. T.C.van Kemenada and R.K.Eijnthoven., *J.Appl.Phys.*, **50**, 938, (1979).

45. T.K.Gupta., *Proceedings of 1984 conference on Electrical insulation and Dielectric phenomena, IEEE Electrical insulation society*, p304, IEEE service center, Piscataway, NJ, (1984).

46. A Sweetana, K.C.Radford, R.G.Johnson and S.P.Hensley, *Ceramic transactions*, **3**, 240, edited by L.M.Levinson, Amer.Ceram.Soc., Westerville, OH, (1989).

47. E.Olsson, I.K.L.Falk, G.E.Dunlop and R.Osterlund., *J.Mater.Sci.*, **20**, 4091 (1985).

48. T.Asokan, G.N.K.Iyengar and G.R.Nagabhushana., *J.Amer.Ceram.Soc.*, **70**, 643 (1987).

49. J.Wong and W.G.Morris., *Amer.Ceram.Soc.Bull.*, **53**, 816 (1974).

50. T.K.Gupta., p493, in *Tailoring multiphase and composite ceramics.*, edited by R.E.Tressler, G.L.Murray, C.G.Pantino and R.E.Newnham, Plenum, NewYork (1986) and A.peigney, V.Carles and A.Rousset, *Mater.Res.Bull.*, **31**, 503 (1996).

51. M.Inada, *Jpn.J.Appl.Phys.*, **17**, 1 (1978).

52. M.Inada, *Jpn.J.Appl.Phys.*, **17**, 673 (1978).

53. J.Wong, *J.Appl.Phys.*, **46**, 1653 (1975).

54. W.D.Kingery, J.B.Van der Sande and T.Mitamura., *J.Amer.Ceram.Soc.*, **62**, 221 (1979).

55. T.K.Gupta, *J.Mater.Res.*, **7**, 3280 (1992).

56. W.G.carlson and T.K.Gupta, *J.Appl.Phys.*, **53**, 5746 (1982).

57. T.Takemura and M.Kobayashi, p50 in *Advances in ceramics*, Vol.**1**, Grain boundary phenomenon in Electronic ceramics, edited by L.M.Levinson and D.Hill, Amer.Ceram.Soc., Columbus, OH (1981).

58. T.Miyoshi, K.Maeda, K.Takahashi and T.Yamazaki., *Advances in Ceramics.*, edited by L.M.Levinson., American Ceramic Sociey, Westerville, OH, **1**, 309 (1981).

59. T.K.Gupta, W.D.Straub, M.S.Ramanchalam, J.P.Schaffer and A.Rohatgi.,

J.Appl.Phys., **66**, 6132(1989).

60. T.K.Gupta, *J.Mater.Res.*, **2**, 231 (1987).
61. T.K.Gupta, *Ferroelectrics*, **102**, 391 (1990).
62. T.K.Gupta and A.C.Miller, *J.Mater.Res.*, **3**, 745 (1988).
63. F.Greuter, G.Blatter, M.Rossinelli and F.Shmuckle., *Defects in semiconductors* in Materials Science forum, volumes **10-12**, p235, edited by H.J.von Bardeleben, Trans Tech Publications Ltd, Switzerland.
64. T.K.Gupta., *J.Mater.Res.*, **9**, 2213 (1994).
65. Y.C.Chen, C.Y.Shen, H.Z.Chen, Y.F.Wei and L.Wu., *J.Mater.Sci.*, **27**, 1397 (1992).
66. H.Kanai, M.Imai and T.Takahashi., *J.Mater.Sci.*, **20**, 3957 (1985).
67. A.Miralles, A.Cornet, A.Herms and J.R.Morante., *Mater.Sci.Engg.*, **A109**, 201 (1989).
68. P.Kostic, O.Milosvic and D.Uskokovic, *Silic.Ind.*, **3-4**, 47 (1985).
69. S.Ezhilvalavan and T.R.N.Kutty., *J.Mater.Sci:Materials in Electronics.*, **7**, 137(1996).
70. Y.Yano, Y.Takai and H.Morooka., *J.Mater.Res.*, **9**, 12(1994).
71. A.Smith, D.S.Smith and P.Abelard., *Mater.Lett.*, **19**, 159 (1994).
72. M.Inada, *Jpn.J.Appl.Phys.*, **19**, 409 (1980).
73. S.A.Pianaro, E.C.Pereira, L.O.S.Bulhoes, E.Longo and J.Varela, *J.Mater. Sci.*, **30**, 133 (1995).
74. ED.Kim, C.H.Kim and M.H.Oh., *J.Appl.Phys.*, **58**, 3231 (1985).
75. A.Kusy and T.G.M.Kleinpennin, *J.Appl.Phys.*, **54**, 2900 (1983).
76. D.K.Kharat, G.S.Dhami and S.K.Date., *Solid State Commun.*, **84**, 375(1992).
77. G.Y.Sung, C.H.Kim and M.H.Oh, *Adv.Ceram.Mater.*, **2**, 841 (1987).
78. A.Smith, G.Gasgnier and P.Abelard., *J.Amer.Ceram.Soc.*, **73**, 1098 (1990).
79. S.I.Nunes and R.C.Bradt., *J.Amer.Ceram.Soc.*, **78**, 2469 (1995)
80. H.Kanai and M.Imai., *J.Mater.Sci.*, **23**, 4379(1988).
81. S.G.Yong and C.H.Kim., *Adv.Ceram.Mater.*, **3**, 604(1988).
82. U.Jaroch, J.Murbe, V.Hilarius and D.Buhling., Ceramics Today-Tomorrow's Ceramics., p2199, *Mater.Sci.Monographs.*, **66C**, Ed.by P.Vincenzini, Elsevier, Amsterdam (1991).

83. J.K.Tsai and T.B.Wu, *Mater.Lett.*, **2**, 199 (1996).

84. B.Vaupel, K.H.Bather, W.Bruckner and U.Schafler, *Krist.Tech.*, **15**, K94 (1980).

85. J.Wong, *J.Appl.Phys.*, **51**, 4453 (1980).

86. L.C.Sletson, M.E.Potter and M.A.Alim, *J.Amer.Ceram.Soc.*, **71**, 909 (1988).

87. M.V.Valsova, N.G.Kakazey, P.Kostic, O.Miloslovic and D.Uskokovic., *J.Mater.Sci.*, **20**, 1660 (1985).

88. A.Igo, M.Matsuoka and M.Masuyama, *Jpn.J.Appl.Phys.*, **15**, 1847 (1976).

90. T.Asokan, G.N.K.Iyengar and G.R.Nagabhushana., *J.Mater.Sci.*, **22**, 2229 (1987).

91. T.Asokan, *Mater.Res.Bull.*, **28**, 1277 (1993).

92. T.Asokan and R.Freer., *Brit.Ceram.Trans.J.*, **89**, 8 (1990).

93. D.K.Kharat, S.R.Sainkar, S.K.date and G.S.Dhami, *J.Sci.and Ind.Res.*, **50**, 596 (1991).

94. J.L.Huang and K.B.Li., *J.Mater.Res.*, **9**, 1526 (1994).

95. Y.S.Lee and T.Y.Tseng., *J.Mater.Sci.:Materials in Electronics.*, **6**, 90 (1995).
S.N.Bai and T.Y.Tseng., *J.Appl.Phys.*, **74**, 695 (1993).

96. P.Singh., *J.Mater.Sci.Lett.*, **9**, 613 (1990).

97. O.Miloslovic, P.Kostic, V.Petrovic and D.Uskokovic., *Sci.Sintering.*, **15**, 121 (1983).

98. R.J.Lauf and W.D.Bond., *Ceram.Bull.*, **63**, 278 (1984).

99. G.Hohenberger and G.Tomandl., *J.Mater.Res.*, **7**, 546 (1992).

100. S.M.Haile, D.W.Johnson, G.H.Wisemann and H.K.Bowen., *J.Amer. Ceram.Soc.*, **72**, 2004 (1989).

101. N.Amiji, Y.Tanno, H.Okuma and M.Kan, *Adv.Ceram. Mater.*, **1**, 232 (1986).

102. R.G.Dosch, B.A.Tuttle and R.A.Brooks., *J.Mater.Res.*, **1**, 90 (1986).

103. G.H.Matier, C.E.Hutchins and S.D.Ross., *Amer.Ceram.Soc.Bull.*, **72**, 73 (1993).

104. E.Sonder, R.A.Zuhr and J.R.Martinelli., *Mater.Res.Soc.Symp.*, **60**, 365 (1986).

105. S.Hingorani, D.O.Shah and M.S.Multani., *J.Mater.Res.*, **10**, 461 (1995).

106. S.Hishita, Y.Yao and S.I.Shirasaki., *J.Amer.Ceram.Soc.*, **72**, 338 (1989).

107. A.F.Octavio, *Rev.Mex.Fis.*, **40**, 771 (1994).

108. L.J.Zhou and Y.Hui., *Mater.Lett.*, **22**, 187 (1995).

109. D.C.Halls and C.Leach., *J.Mater.Sci.*, **30**, 2733 (1995).

110. M.C.S.Nobrega and J.K.West, *Ceram.Eng.Sci.Proc.*, **15**, 1044 (1994).

111. D.Makovec, D.Kolar and M.Trontlej, *Mater.Res.Bull.*, **28**, 803C (1993).

112. L.M.Levinson, H.A.Comanzo and W.N.Schultz., *Mater.Res.Soc.Symp. Proc.*, **269** [Microwave processing of Materials III], 311 (1992).

113. S.D.Sin, C.S.Sone, J.H.han and D.Y.Kim., *J.Amer.Ceram.Soc.*, **79**, 565 (1996).

114. S.N.Bai and T.Y.Tseng., *Jpn.J.Appl.Phys.*, Part1, **31**, 81 (1992).

115. Y.C.Chen, C.Y.Shen, H.Z.Chen, Y.F.Wei and L.Wu., *J.Mater.Sci.*, **27**, 1397 (1992).

116. F.Grueter, G.Blatter, M.Rosinelli and F.Stucki, *Advances in Varistor Technology*, ed. by L.M.Levinson [American Ceramic Society, Westerville, OH], 31 (1988)

117. G.E.Pike, *Grain boundaries in Semiconductors*, ed. by G.E.Pike, C.H.Seager and H.J.Leamy [Elsevier, Amsterdam] 369 (1982).

118. J.D.levine., *Crit.Rev.Solid.State.Sci.*, **5**, 596 (1975).

119. N.Shohata, T.Matsumara and T.Ohno., *Jpn.J.Appl.Phys.*, **19**, 1793 (1980).

120. J.Bernasconi, S.Strassler, B.Knecht, H.Klein and A.Menth., *Solid.State.Commun.*, **21**, 867 (1977).

121. J.P.Gambino, W.D.Kingery, G.E.Pike, H.R.Philipp and L.M.Levinson., *J.Appl.Phys.*, **61**, 2571 (1987).

122. D.V.Lang., *J.Appl.Phys.*, **45**, 3023 (1974).

123. T.Maeda, S.Meguro and M.Takata., *Jpn.J.Appl.Phys.*, **28**, L714 (1989).

124. K.Tuda and K.Mukae, *IECEJ. Tech.Rep.CPM86-29*, 27 (1986).

125. Y.Yano, Y.Shirakawa and H.Morooka., *Jpn.J.Appl.Phys.*, **31**, L714 (1992).

126. F.Stucki, P.Bruesch and F.Grueter, *Surf.sci.*, **189/190**, 2941 (1987).

127. M.Hayashi, M.Kuramoto and M.Hayashi., *Ceramic Transactions.*, **3**, 364 (1988).

128. J.F.Cordaro, Y.Shim and J.E.May., *J.Appl.Phys.*, **60**, 4186 (1986).

129. Y.Shim and J.F.Cordaro., *J.Appl.Phys.*, **64**, 3994 (1988).

130. S.Tanaka, K.Takahashi, T.Sekiguchi, K.Sumino and J.Tanaka., *J.Appl.Phys.*, **77**, 4022 (1995).

131. C.H.Seager, *Ann.Rev.Mater.Sci.*, **15**, 271 (1985).

132. A.B.Alles and V.L.Burdick., *J.Appl.Phys.*, **70**, 6883(1991).

133. F.Stucki and F.Grueter., *Appl.Phys.Lett.*, **57**, 446 (1990).

134. S.Tanaka, C.Akita, N.Ohashi, J.kanai, H.Haneda and J.Tanaka., *J.Solid. State.Chem.*, **105**, 36 (1993).

135. K.Eda, A.Iga and M.Matsuoka., *Jpn.J.Appl.Phys*., **18**, 997 (1979).

136. K.Eda, A.Iga and M.Matsuoka., *J.Appl.Phys*., **51**, 2678 (1980).

137. C.G.Shirley and W.M.Paulson., *J.Appl.Phys*., **50**, 5782 (1979).

138. K.Sata, Y.Takada, H.Mackava and M.Ototake., *Jpn.J.Appl.Phys*., **19**, 909 (1980)

139. W.Moldenhauer, K.H.Bather, W.Bruckner, D.Hizn and Buhling., *Phys.Status, Solidi A*, **67**, 533 (1981).

140. T.K.Gupta, W.G.Carlson and P.L.Hower., *J.Appl.Phys*., **52**, 4104 (1981).

141. M.Takata., *Amer.Ceram.Bull*., **72**, 96 (1993).

142. A.Bui, A.Khedim, A.Loubiere and M.B.Kourdi., *J.Appl.Phys*., **69**, 1036 (1991).

143. T.J.Gardner, D.H.Doughty, S.J.Lockwood, B.A.uttle and J.A.Voigt, *Advances in Varistor Technology*, *Vol.3 Ceramic Transactions*., ed. by L.M.Levinson (The American ceramic Society, Westerville, Oh) 84 (1990).

144. H.R.Philipp and L.M.Levinson, *Advances in ceramics, Vol.7 Additives and interfaces in electronic ceramics*, ed. by M.F.Yan and A.H.hener (The American Ceramic Society, Columbus, OH), 1 (1983).

145. M.Takata., *Amer.Ceram.Soc.Bull*., **72**, 96 (1993).

146. T.K.Gupta and W.G.Carlson., *J.Mater.Sci*., **20**, 3487 (1985).

147. E.R.Leite, J.A.Varela and E.Longo., *J.Mater.Sci*., **27**, 5325 (1992).

148. A.Rohatgi, S.K.Pang, T.K.Gupta and W.D.Straub., *J.Appl.Phys*., **63**, 5375 (1988).

149. T.K.Gupta and W.G.Carlson., *J.Appl.Phys*., **53**, 7401 (1982).

150. D.J.Binks and R.W.Grimes., *J.Amer.Ceram.Soc*., **76**, 3270 (1993).

151. G.E.Pike., *Phys.Rev.B*., **30**, 795 (1984).

152 G.Blatter and F.Grueter., *Phys.Rev.B*., **33**, 3952 (1986).

153. A.Goetzberger, B.McDonald, R.Haitz and R.Scarlett., *J.Appl.Phys*., **34**, 1591 (1963).

154. S.M.Sze., *Physics of Semiconductor Devices* (Wiley Interscience, NewYork 1969).

155. T.Shirakawa, A.Hayashi and J.Nakai., *Jpn.J.Appl.Phys*., **9**, 420 (1970).

156. L.M.Levinson and H.R.Philipp., *J.Appl.Phys*., **46**, 1332 (1975), and
H.R.Philipp and L.M.Levinson., *J.Appl.Phys*., **46**, 3206 (1975).

157. W.G.Morris., *J.Vac.Sci.Technol*., **13**, 926(1976).

158. P.R.Emtage., *J.Appl.Phys*., **48**, 4372(1977).

159. K.Eda., *J.Appl.Phys*., **49**, 2964(1978).

160. R.Einzinger., *Appl.Surf.Sci*., **1**, 329(1978).

161. P.L.Hower and T.K.Gupta., *J.Appl.Phys*., **50**, 4847(1979).

162. G.D.Mahan, L.M.Levinson and H.R.Philipp., *J.Appl.Phys*., **50**, 2799 (1979).

163. K.Eda., in *Grain boundaries in semiconductors*, p381, Ed.by H.J.Leamy, G.E.Pike and C.H.Seager., Elsevier, NewYork, 1982.

164. G.E.Pike., *Phys.Rev.B*., **30**, 795(1984).
G.E.Pike., *Mater.Res.Soc*., **5**, 369 (1982).

165. L.M.Levinson and H.R.Philipp., *Am.Ceram.Soc.Bull*., **65**, 639(1986).

166. G.Blatter and F.Grueter, *Phys.Rev.B*., **33**, 3952 (1986).

167. F.Grueter and G.Blatter., *Polycrystalline semiconductors in Springer proceedings in Physics*, **35**, 302, (1989), ed.by J.H.Werner, H.J.Moller and H.P.Struck (Springer-Verlag Berlin, Heidelberg).

168. S.M.Kim, H.H.Oh and C.K.kim., *Jpn.J.Appl.Phys*., Part2, **30**, L1917 (1991).

169. G.E.Pike, S.R.Kurtz, P.L.Gourley, H.R.Philipp and L.M.Levinson., *J.Appl.Phys*., **57**, 5512 (1985).

170. *Impedance Spectroscopy* (Emphasizing on solid materials and systems) ed. by J.R.Macdonald (A Wiley Interscience publication) (1987).

171. M.A.Alim, M.A.Seitz and R.A.Hirthe., *J.Amer.Ceram.Soc*., **71**, C52 (1988).

172. M.A.Alim and M.A.Seitz, *J.Amer.Ceram.Soc*., **71**, C246, (1988).

173. M.A.Alim, *J.Amer.Ceram.Soc*., **72**, 28, (1989).

174. M.A.Alim, M.A.Seitz and R.A.Hirthe., *J.Appl.Phys*., **63**, 2337 (1988).

175. M.A.Alim, M.A.Seitz and R.A.Hirthe., *Extended abstracts of the Electrochemical society fall meeting*, Vol 85-2, Abstract no. 380-381, Las Vegas, 1985.

176. K.Al Abdullah, A.Bui and A.Loubiere, *J.Appl.Phys*., **69**, 4046 (1991).

177. A.Smith, J.F.Baumard, P.Abelard and M.F.Denanot., *J.Appl.Phys*., **65**, 5119 (1989).

178. L.C.Sletson, M.E.Potter and M.A.Alim., *J.Amer.Ceram.Soc*., **71**, 909 (1988).

179. K.S.Kirckpatrick, T.O.mason, U.Balchandran and R.B.poeppel, *J.Amer.Ceram. Soc*., **77**, 1493 (1994).

180. L.Zhou and C.Yu, *J.Mater.Sci*., **29**, 6055 (1994).

181. Y.Nakano and N.Ichinose, *J.Mater.Res*., **5**, 2910 (1990).

N.Yamaoka, M.Masuyam and M.Fukui, *Amer.Ceram.Soc.Bull.*, **62**, 698 (1983).

M.Fujimoto, Y.M.chiang , A.Roshko and W.D.Kingery., *J.Amer.Ceram.Soc.*, **68**, C300 (1985).

182. F.A.Modine and H.M.Hyatt., *J.Appl.Phys.*, **64**, 4229 (1988).
183. N.Shohata, M.Nakanishi and K.Utsumi., *Advances in Varistor Technology, Vol.***3** *in Ceramic Transactions*, 329 (1989) ed..by L.M.Levinson (Amer.Ceram.Soc., Westerville, OH).
184. H.C.Ling, M.F.Yan and W.W.Rhodes., *J.Amer.Ceram.Soc.*, **72**, 1274 (1989).
185. Y.S.Lee and T.Y.Tseng., *J.Mater.Sci: Materials in Electronics*, **6**, 90 (1995).
186. M.F.Yan and W.W.Rhodes., *Appl.Phys.Lett.*, **40**, 536 (1982).
187. S.L.Yang and J.M.Wu., *J.Amer.Ceram.Soc.*, **76**, 145 (1993).
188. S.L.Yang and J.M.Wu., *J.Mater.Res.*, **10**, 345 (1995).
189. S.L.Yang and J.M.Wu., *J.Mater.Sci.Lett.*, **14**, 748 (1995).
190. S.A.Pianara, P.R.Brueno, E.Longo and J.A.Varela., *J.Mater.Sci.Lett.*, **14**, 692 (1995).
191. S.Ezhilvalavan and T.R.N.Kutty., *Appl.Phys.Lett.*, **68**, 2693 (1996).
192. F.A.Grant., *Rev.Mod.Phys.*, 646 (1959).
193. W.H.Bauer., *Acta.Cryst.*, **9**, 515 (1956).
194. R.G.Breckenbridge and W.R.Hosler., *Phys.Rev.*, **91**, 793(1953).
195. P.Kofstad., *J.Less-Common.Met.*, **13**, 635(1967).
196. A.M.Azad, S.A.Akbar, L.B.Younkman and M.A.Alim., *J.Amer. Ceram. Soc.*, **77**, 3145(1994).
197. Z.M.Jarzebski and J.P.Morton., *J.Electrochem.Soc.*, **123**, 199C(1976).
     Z.M.Jarzebski and J.P.Morton., *J.Electrochem.Soc.*, **123**, 299C(1976).
     Z.M.Jarzebski and J.P.Morton., *J.Electrochem.Soc.*, **123**, 333C(1976).
198. C.G.Fonstad and R.H.Rediker., *J.Appl.Phys.*, **42**, 2911(1971).
199. J.F.MacAler, P.T.Moseley, J.O.W.Norris and D.E.Williams., *J.Chem. Soc.*, **83**, 1323(1987).
200. H.A.Klasens and H.Koelmans., *Solid.State.Electron.*, **7**, 701(1964).
201. A.Aoki and H.Sasakura., *Jpn.J.Appl.Phys.*, **9**, 582(1970).
202. Passive components-Data Handbook, PHILIPS INDIA Limited, Book PLO1, 1996.

CHAPTER 2

EXPERIMENTAL

2.1 Introduction

This chapter describes the various experimental techniques employed in the synthesis, physico-chemical and electrical characterization of TiO_2 and SnO_2 based electroceramic voltage sensors, which is divided in three parts.

I. Synthesis of voltage sensor materials by conventional ceramic and by chemical routes. Other steps involved, such as, pelletizing, sintering, electroding to make the final product is also described.

II. Physico-chemical characterization comprising of density, phase analysis by powder X-ray diffraction, microstructure analysis by Scanning electron microscopy and thermal analysis by DTA/TGA.

III. Electrical characterization comprising of current-voltage (I-V) measurements at room temperature and ac impedance analysis at various temperatures between room temperature and 300°C

2.2 PART-I Synthesis of active powders

2.2.1 TiO_2 based Voltage sensors

2.2.1.1 Solid state synthesis route

In this section, the conventional method of synthesizing the TiO_2 voltage sensors is described. The oxides or carbonates of the representative elements are mixed in the stoichiometric ratio in the solid/powder form. Commercially available TiO_2 powder [99% pure Loba Chemie make] was taken as the base material. Oxides of Nb_2O_5 (Aldrich), Bi_2O_3, $SrCO_3$(Loba Chemie) were added to this TiO_2 base powder in the required ratio. These powders were first mixed thoroughly in the dry form inside a glass jar. The deionized water was added as the mixing agent and a slurry is formed. This mixed slurry is then transferred to a plastic jar containing glass balls. This jar is then rotated continuously for 24 hrs on rollers. A 2% PVA solution was also added into this slurry as a binding agent. After the ball

milling, the slurry was allowed to dry in an oven at T ≈ 60°C. The thoroughly dried powder is then pelletized using a steel die to get 12mm dia. pellets using a hydraulic press under a uniform pressure of 5000 psi. These pellets were then directly sintered at various temperatures in an electric furnace [Okay Furnace] for 2 hrs. This conventional ceramic process of TiO_2 voltage sensor is given in the form a block diagram in figure**2.1**.

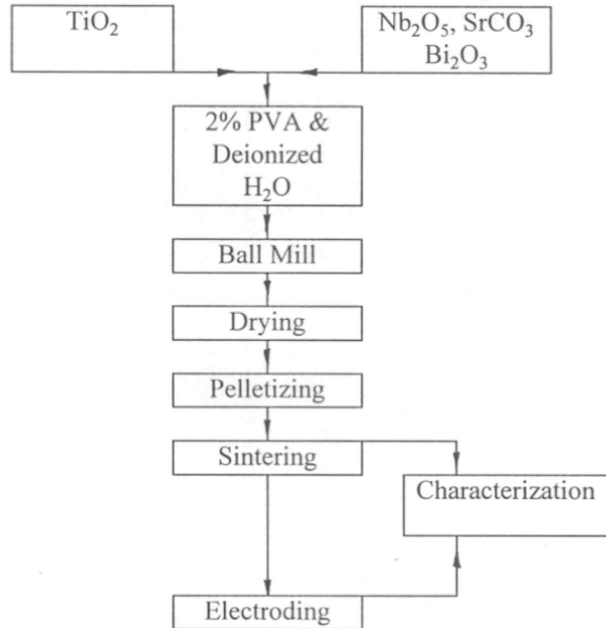

Figure 2.1 Block diagram for solid state synthesis of TiO_2 based varistor.

2.2.1.2 Chemical synthesis route

Chemical synthesis route used here is a liquid mix technique. chemical synthesis of the TiO_2 base electroceramic voltage sensors is given in the form of a block diagram in figure**2.2**. The source of titanium in this case is butyl titanyl monomer (BTM) which have the formula $(C_4H_9O)_4.Ti$, which is taken in 0.1 molar concentration. Strontium and Bismuth were added in the form of aqueous solutions of their nitrates. The BTM solution and the nitrate solution were mixed in the required stoichiometric ratio along with 750ml distilled water. The whole solution is stirred continuously. To this stirring mixture the required amount of Nb_2O_5 was

added. This mixture is stirred for 3 hrs. since there is a possibility of lose of some soluble complexes of the dopants during filtration, the whole mixture was dried on a water bath and the dried powder was calcined at different temperatures. Direct sintering of the pellets are to be avoided since the evolution of nitrous fumes and other gases can lead to crumbling of the pellets.

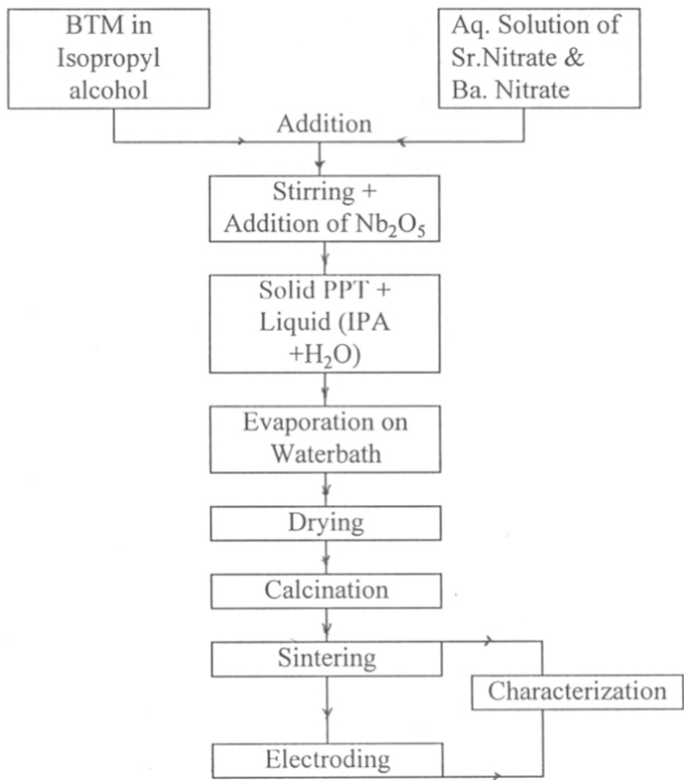

Figure 2.2 Block diagram for chemical synthesis of TiO_2 based varistor.

2% PVA solution was added to the calcined powder as a binder similar to the ceramic method. The samples are then sintered at various temperatures in an electric furnace. These sintered compacts are characterized by other methods.

2.2.2 SnO_2 based voltage sensor

2.2.2.1 Solid state synthesis route

In this case, the conventional ceramic route of synthesis was followed. Here the oxide form of the dopants were used directly. This method of synthesis is given in the form of a block diagram in figure **2.3**. SnO_2 [99% pure E merck Darmstardt] was the main constituent. CoO, Nb_2O_5 and Al_2O_3 were weighed in the required ratio (Sn:Co:Nb:Al is taken in the ratio 98.9:1:0.05:0.05) and mixed to the form of a slurry with aid of distilled alcohol as the mixing agent. This mixed slurry is then transferred into plastic jar containing glass balls. This plastic jar is then rotated using a roller for 24 hrs along with 2%PVA solution added as the binder. The ball milled slurry is then dried in an oven at 60°C. The thoroughly dried

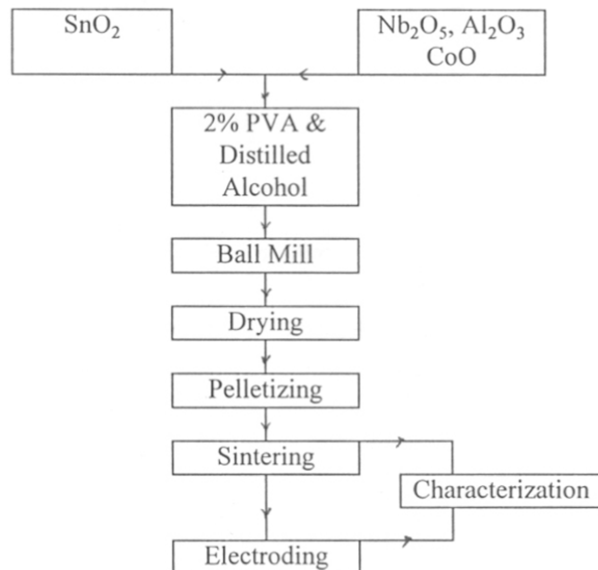

Figure 2.3 Block diagram for solid state synthesis of SnO_2 based varistor.

powder is then pelletized under a uniform pressure of 5000 psi. These pellets are then directly sintered at various temperatures and are now ready for further characterizations.

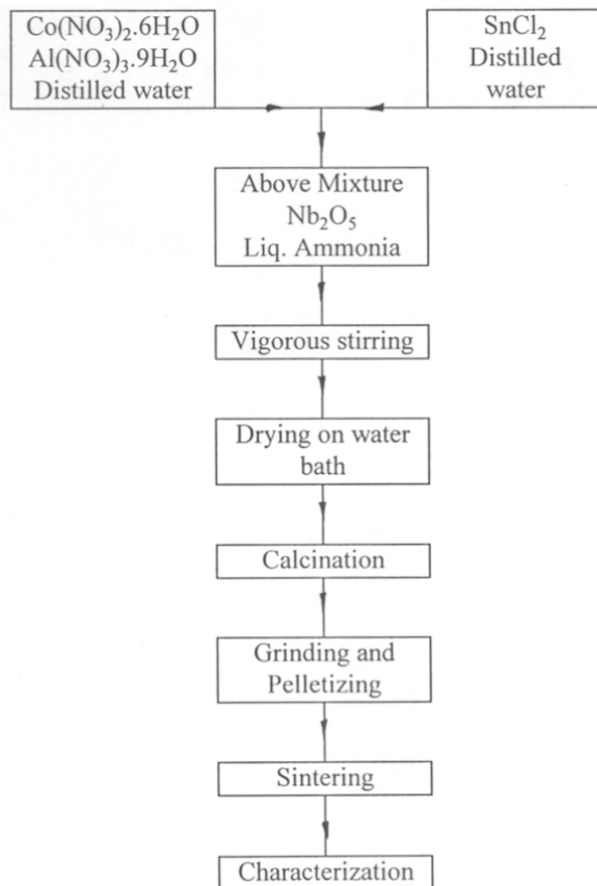

Figure 2.4 Block diagram for chemical synthesis of SnO_2 based varistor

2.2.2.2 Chemical synthesis route

Chemical synthesis of the same composition of SnO_2 based electroceramic voltage sensor is done to get a homogeneous distribution of dopants. Here also Sn:Co:Nb:Al is taken in the ratio 98.9:1:0.05:0.05. The processing steps of this chemical method of synthesis is given in the form a block diagram in figure**2.4**. The base materials used for this synthesis were $SnCl_2$, $Co(NO_3)_2.6H_2O$, Nb_2O_5 and $Al(NO_3)_3.9H_2O$. A solution containing $Co(NO_3)_2.6H_2O$, $Al(NO_3)_3.9H_2O$ is prepared in 1000ml distilled water. $SnCl_2$ is hydrolized in 600ml distilled water and was added to the above solution. The whole solution is continuously stirred. Nb_2O_5 is added to this stirred solution along with 18ml liquid ammonia. Sufficient amount of ammonia was added so that Co dopants gets completely precipitated. Care was taken not

to add more ammonia which can lead to the formation of soluble complexes. This mixture is continuously stirred for 3 hrs and then was allowed to settle down. A slight reddish precipitate along with the solution is dried on a water bath. This method of drying was employed to avoid the possible loss of dopants during filtration. The dried powder was then calcined at different temperatures.

Here also direct sintering is avoided since the evolution of large amount of gases destroys the formation of dense pellets. The calcined powder was then pelletized with the help of 2% PVA solution as a binder. These pellets were then sintered at various temperatures for 2hrs, These sintered pellets were then used for different characterizations.

2.3 PART-II Physico-chemical characterization

2.3.1 Density

Density of the sintered pellets were measured to understand the effect of sintering temperatures. The sintered pellets were lapped to uniform thickness with help of 400 mesh carborundum powder. The weight of the sample is accurately measured using a microbalance and the thickness and diameter of the pellets were found out using a screw gauge. The density was calculated on 3 to 4 samples of a given batch and an average value was taken. The variation was found to be negligibly small.

2.3.2 Thermal analysis (DTA/TGA)

The measurements of change in any property as a material is being heated or cooled (at a constant rate) is called Thermal analysis. Weight (Thermogravimetry) and heat content(Differential thermal analysis DTA) are examples of such properties which comes under the broad category of Thermal analysis. Both DTA and TGA were done on the base powders using a Seiko(TG/DTA 32) Thermal analyzer between room temperature and 900°C at a rate of 10°C.

2.3.3 Phase analysis by X-ray diffraction

X-ray diffraction is the most commonly used method for structure determination. This is because X-rays have wavelength nearly identical to the interatomic spacing in crystals(few

A°). Cu k_{α}(Ni filter λ = 1.54 A°) is the most commonly used X-ray radiation for crystal structure analysis.

Powder diffraction method is a widely used experimental technique for the determination of crystal structures. Here the powder is kept at the center of a cylindrical cassette. The detector is rotated around the cassette and the diffraction occurring at various angles are recorded. In this case rotation of the crystals is avoided.

The X-ray diffraction pattern of the electroceramic voltage sensors were taken with a Philips 1730 diffractometer. All the characterizations were done on sintered pellets and hence the orientation of certain phases will lead to changes in the relative intensity in the diffraction pattern. The x-ray patterns were taken in the range 10-60° and at 2000cps at a rate of 4°/minute. The X-ray patterns were analyzed using a commercial powder diffraction program (PDP 1.1)

2.3.4 Microstructural analysis by Scanning Electron Microscope

In this work, the SEM photographs were taken on the fractured surface of the varistor after coating the fractured surface with gold. The fractographs were taken with the aid of a Leica Cambridge 440 microscope. These fractographs were taken for the identification of the grain sizes, grain-grain boundary distribution (microstructural distribution). The grain sizes were found by counting the number of grains intercepted by a line of known length and taking the average of 3-4 measurements made across a given fractograph. The task was made easy with the in built ability of the SEM system by which one can measure the grain sizes by moving the cursor across the grain.

2.4 Part-III Electrical Characterization

2.4.1 Electroding

For electrical measurements the samples were given electrical contacts using silver paint. First the samples were lapped to required thickness and the thickness is accurately measured using a screw gauge. Then circular contacts of known diameter are given to the ceramic compacts using silver paint.

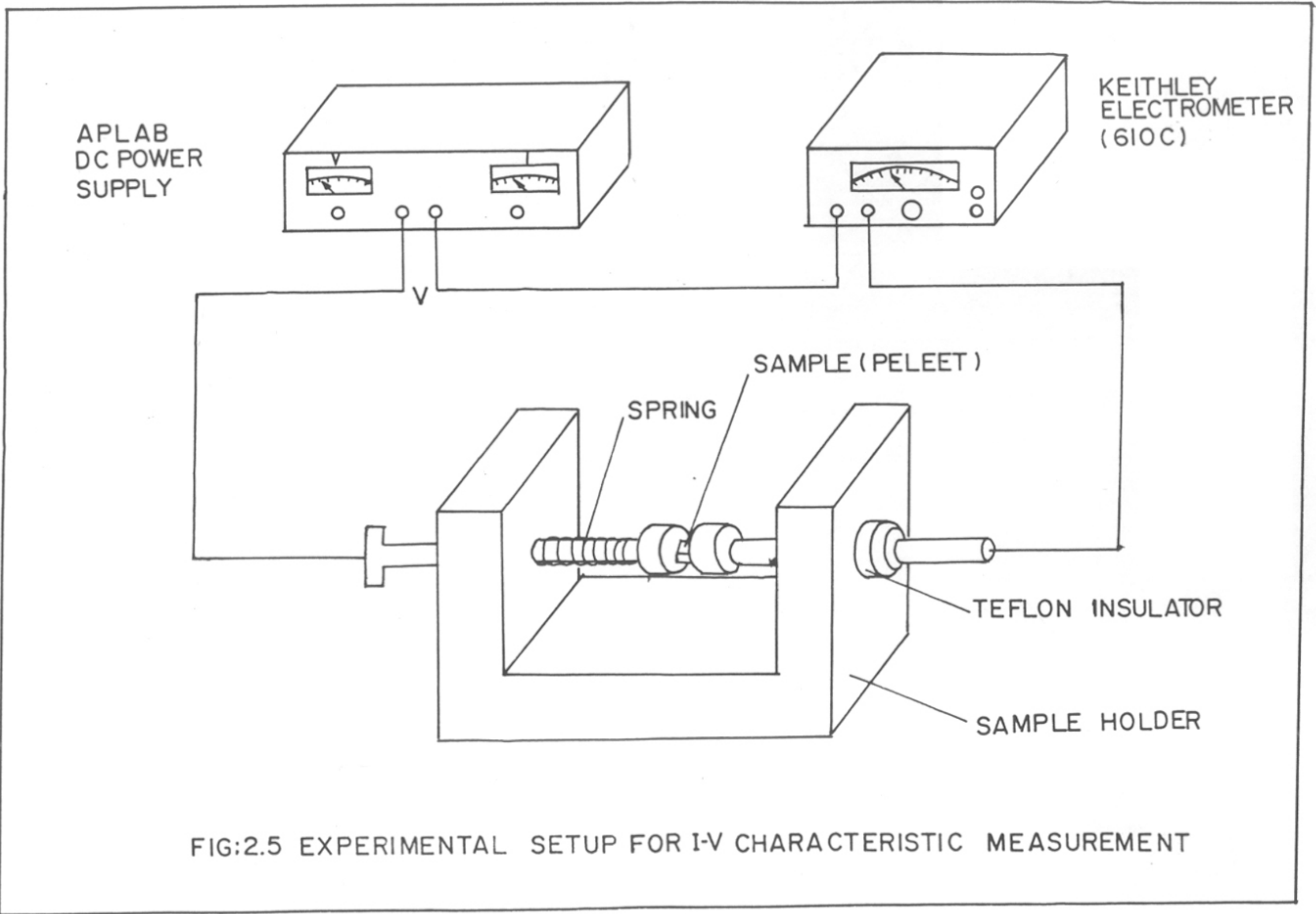

FIG:2.5 EXPERIMENTAL SETUP FOR I-V CHARACTERISTIC MEASUREMENT

The pellets along with silver paint is cured at 600°C for a few minutes to get good electrical contacts. This curing is done to burn away the organic binders used in the silver paint.

2.4.2 DC current-voltage characterization

The room temperature dc current-voltage characterization of the voltage sensors were done using the setup shown in figure**2.5**. The large range of currents are measured using a Keithley electrometer (610C) and the voltage sources used to give the bias were APLAB 7161 and 7323. These measurements were carried out up to a maximum current of 10mA since at high currents the chances of thermal breakdown are high. (It is always advisable to measure the current-voltage characteristics above this region using pulse voltage method). At each voltage point a certain time lag is given for the current to stabilize. A digital multimeter was used to measure the applied voltage accurately.

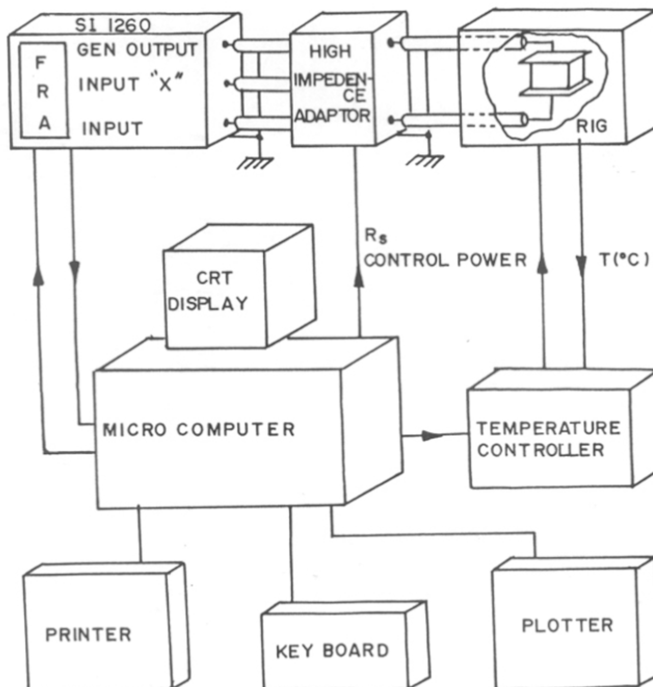

Figure 2.6 Block diagram for ac impedance measurements.

2.4.3 AC impedance measurements

For ac impedance measurements, a sintered pellet of 10mm diameter and 0.7mm thickness were used which were given electrical contacts as explained in the section**2.4.1**. For each set of measurements, the sample is kept between platinum electrodes working on a spring loaded arrangement. This fixture made of ceramic material is called the rig. This rig assembly is then inserted in an electrical furnace for high temperature measurements. The furnace temperature is controlled within an accuracy of (±1°C). The ac impedance data was recorded in the temperature range 25° to 300°C over the frequency range 100Hz-32MHz using a computer controlled Solartron 1260 impedance analyzer. Figure**2.6** gives the block diagram for a.c impedance measurements. For complex data analysis, Boukamp software package was used. These measurements were carried out to establish the equivalence between functional and electrical microstructure developed during synthesis.

The data obtained from the above said physical measurements along with the corresponding microstructural data will definitely give information about the influence of microstructure on the final performance parameters of the ceramic voltage sensor.

CHAPTER 3

TITANIUM DIOXIDE VARISTOR

3.1 Introduction

TiO_2 is an n-type wide band gap oxide semiconductor with an energy gap of ~3.1eV. It exists in three forms anatase, rutile and brookite[1,2]. The rutile structure is the high temperature structure (≥700°C) and is the thermally stable form. A brief description of the structure and physico-chemical properties of titania is given in section **1.16**. The wideband gap and the relatively open structure of rutile TiO_2 structure is a good base material for making a varistor since the intrinsic material characteristics aid doping of elements required to engineer the non-linear characteristics. The electrical conductivity of rutile TiO_2 is known to arise mainly due to the oxygen vacancies, titanium interstitials and other defects produced by small amount of impurities present in the material.

Few reports are already available on varistors based on TiO_2 [3-6]. In all these reports, TiO_2 varistors are made with the help of two kinds of dopants. The first one is the pentavalent dopant (e.g.Ta^{5+} and Nb^{5+}) to increase the conductivity of the TiO_2 grains. These dopants provide an extra electron to the lattice and thereby decrease the resistivity. The second group of dopants are the acceptors (eg: Ba^{2+}), which because of their ionic size will be segregating at the grain boundary. These acceptors will take away the electrons from the grains and thereby create a depletion layer of positive charges leading to energy barriers needed for non-linear current voltage behaviour.

3.2 Experimental results and Analysis

In our experiments Nb_2O_5 is added as the pentavalent dopant in this varistor composition. 0.25mol% of Nb_2O_5 is added to 100mol% TiO_2. The amount of Nb_2O_5 is fixed to 0.25mol% since according to data available, the lowest resistivity of Nb-doped TiO_2 occured around 0.25mol%. Either increase or decrease of Nb content from 0.25mol% have lead to an increase in resistivity. Sr is selected from the second group of dopants which are acceptor dopants. These dopants have ionic sizes larger than the Ti^{4+} ion size, hence these ions will preferentially segregate at the grain boundaries to avoid the large elastic energy associated with Sr^{2+} substitution of Ti^{4+}. Also, the grain boundary, which is a "defect in defect structure"[7] has enough vacancies to accommodate these larger ions. Sr was also added in a very small concentration to the above mixture of TiO_2 and Nb_2O_5. Bi^{3+} ions were added as

the third dopant species in this varistor system. Bi^{3+} is also an acceptor dopant which form volatile phase at low temperature itself. Second acceptor was chosen because with the use of a single acceptor, the performance parameters seem to be strongly interconnected and hence maneuvering one property adversely affected the second one. Therefore the improvement in performance parameters were found to be limited. Hence the second acceptor dopant Bi^{3+} was also tried. Bi^{3+} was also added in a very small concentration of 1mol%.

As described earlier, TiO_2 compacts with the dopants were synthesized to the final sintered form by the conventional ceramic route. The electrical characteristics and other measurements were carried out as described in Chapter.**2**. The experimental results arrived at and the discussion of the results are given in the following sections.

3.3 Current-voltage (I-V) characteristics

A typical current-voltage characteristics measured on these TiO_2 compacts/pellets are given in Figure **3.1**. The I-V curves of the samples sintered at 1100°C, 1200°C, 1250°C, 1300°C and 1350°C are given. The sample sintered at 1100°C showed negligible non-linear behaviour with an $\propto$ value of 1.6. The breakdown voltage (E_{1mA}), which is the voltage applied corresponding to 1mA current, cannot be found out in this case. The performance parameters ($\propto$ and E_{1mA}) found from the I-V curves for these TiO_2 compacts are given in Table **3.1**. The sample sintered at 1200°C also shows negligible non-linear behaviour, with a very small $\propto$ value of 1.7 and in this case also the breakdown voltage is not found within the limits of our experiment. The sample sintered at 1250°C exhibits improved non-linear behaviour with an $\propto$ value of 7.35. The breakdown voltage E_{1mA} for this sample is 120volts/mm. As the sintering temperature is increased to 1300°C, $\propto$ value also increased slightly to ~8.4 and the breakdown voltage decreases to 104 volts/mm. But as the sintering temperature is further increased to 1350°C, both $\propto$ as well as E_{1mA} decrease. The performance parameters at this temperature are $\propto = 5.5$ and $E_{1mA} = 70$ volts/mm.

When the above curves are closely analyzed, it can be seen that the sample sintered at 1100°C and 1200°C shows negligible non-linear behaviour. This may have something to do with the formation of an effective grain boundary region.

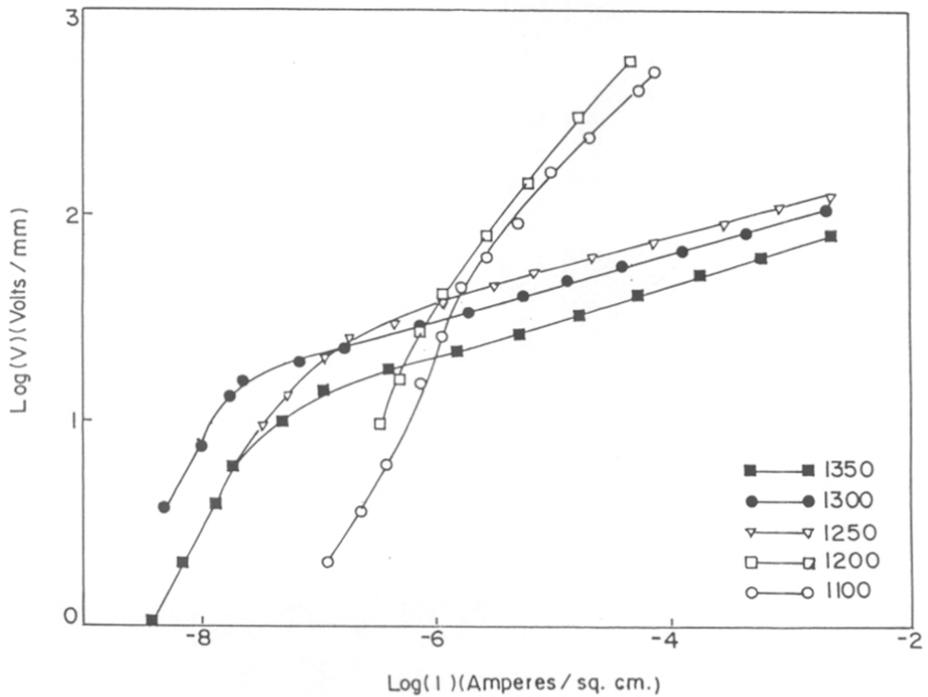

Figure3.1 Current-voltage characteristics of TNSB samples sintered at 1100°C, 1200°C, 1250°C, 1300°C and 1350°C.

The pre-breakdown region is to be analyzed because this is the region in the I-V curve which is controlled entirely by the grain boundary impedance. The current density in this region for the 1100°C and 1200°C samples are found be higher compared to other samples. The high current in this region means low impedance. i.e., low grain boundary impedance. This low grain boundary impedance points out that at this temperature(1100 & 1200) the grain boundary region is not well developed. At 1250°C, 1300°C and 1350°C, the grain boundary resistance are rather high ($\sim 10^8 \Omega$) pointing at the formation of well defined grain boundary region. The current-voltage characteristics hence leads to the conclusion that 1300°C is the optimum temperature for sintering, since this gives the maximum non-linear coefficient. The temperature around 1300°C is the temperature range at which an effective grain boundary is formed. The decrease of the non-linearity at 1350°C may related to the loss in the volatile Bismuth dopant at higher temperatures. The micro and macrostructural

properties of these sample are characterized by DTA/TGA, SEM, XRD etc and these results are given below.

Table 3.1 Performance parameters of TNSB samples

Sintering Temperature(°C)	Non-linear coefficient (∝)	Breakdown voltage (E_{1mA}) volts/mm
1100	1.6	--
1200	1.7	--
1250	7.35	120
1300	8.4	104
1350	5.5	70

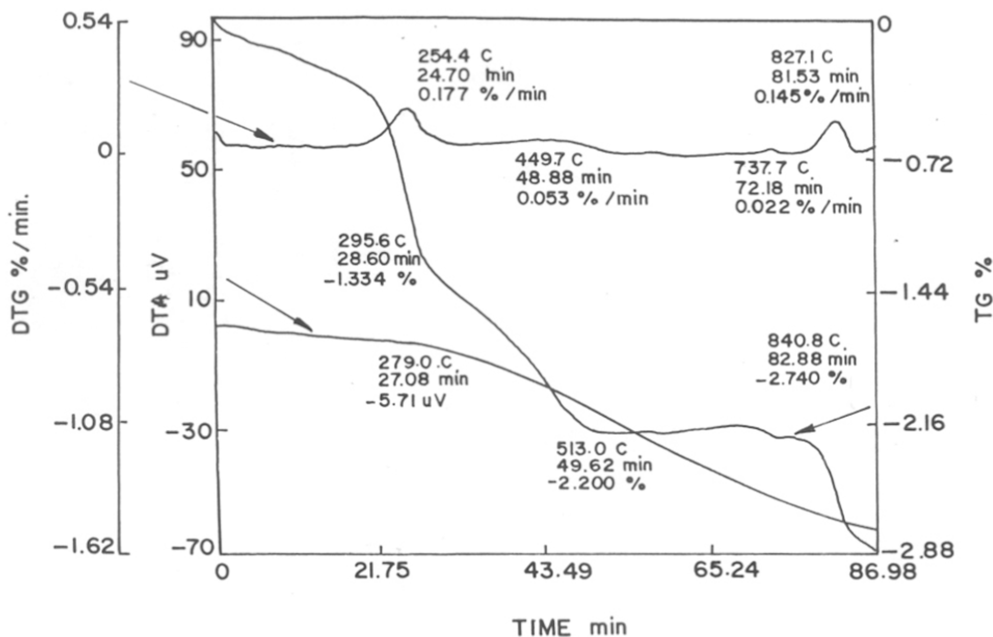

Figure3.2 DTA/TGA/DTG curves of TNSB powder (Measurement done at the rate of 10°C per minute).

3.4 DTA/TGA analysis

The well mixed TiO_2 powder with additives was air dried and small amount of it was subjected to DTA/TGA/DTG analysis in air from 30-900°C with a heating rate of 10°C/min. The DTA/TG/DTG curves are given in figure**3.2**. The TG curve showed endothermic losses in two steps in temperature regions 30-279°C and 280-600°C respectively. The frst loss is attributed to removal of absorbed water while second loss in the temperature 280-600°C is attributed to PVA binder burn out process. The change at 830°C is related to melting of Bi_2O_3 and loss due to its evaporation and leading to the formation of varistor powder.

3.5 Density

The density of these Sr-doped TiO_2 ceramics were found out by measuring the dimensions and weight of the compact discs. The density of samples versus the corresponding sintering temperature is given in figure **3.3**.

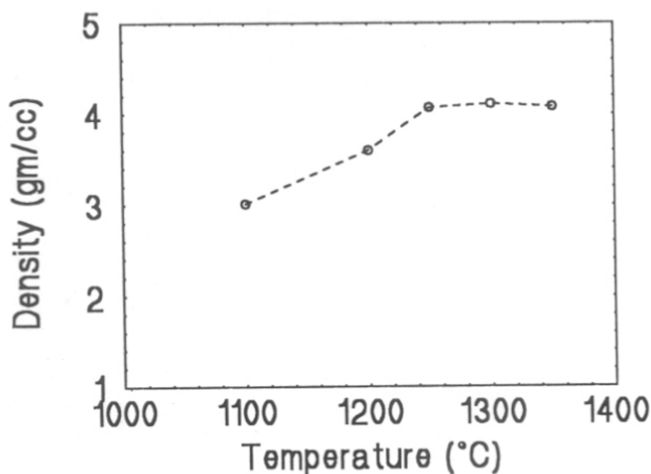

Figure3.3 Measured density vs corresponding sintering temperature of the TNSB pellets

The theoretical density of TiO_2 rutile phase is 4.25gm/cc. The sample sintered at 1100°C have a poor density of 3.01 gm/cc. At 1200°C the density increases to 3.6gm/cc. As the sintering temperature is further increased the density is also enhanced, reaching values of 4.07gm/cc and 4.11gm/cc for sintering temperature of 1250 and 1300°C, respectively. At

1300°C, the maximum density of 4.11gm/cc is attained. A further increase in sintering temperature to 1350°C decrease the density to 4.08gm/cc. The density values also follows the current-voltage characteristics, leading to the conclusion that the optimum temperature for sintering in this TiO_2 varistor composition is 1300°C and that higher densification is necessary to have optimum grain-grain boundary contacts.

It is well known that the oxygen diffusion which depends on the concentration of oxygen vacancies is the major factor that determines the sintering kinetics in TiO_2 ceramics. Hence it is concluded that at higher temperatures (≥ 1250°C) sufficient oxygen vacancies as well as titanium interstitial's are created. These oxygen vacancies will enhance oxygen diffusion enhancing the density of the compacts. This decrease in density at higher sintering temperature, above 1300°C, may be due to the loss of Bi dopants.

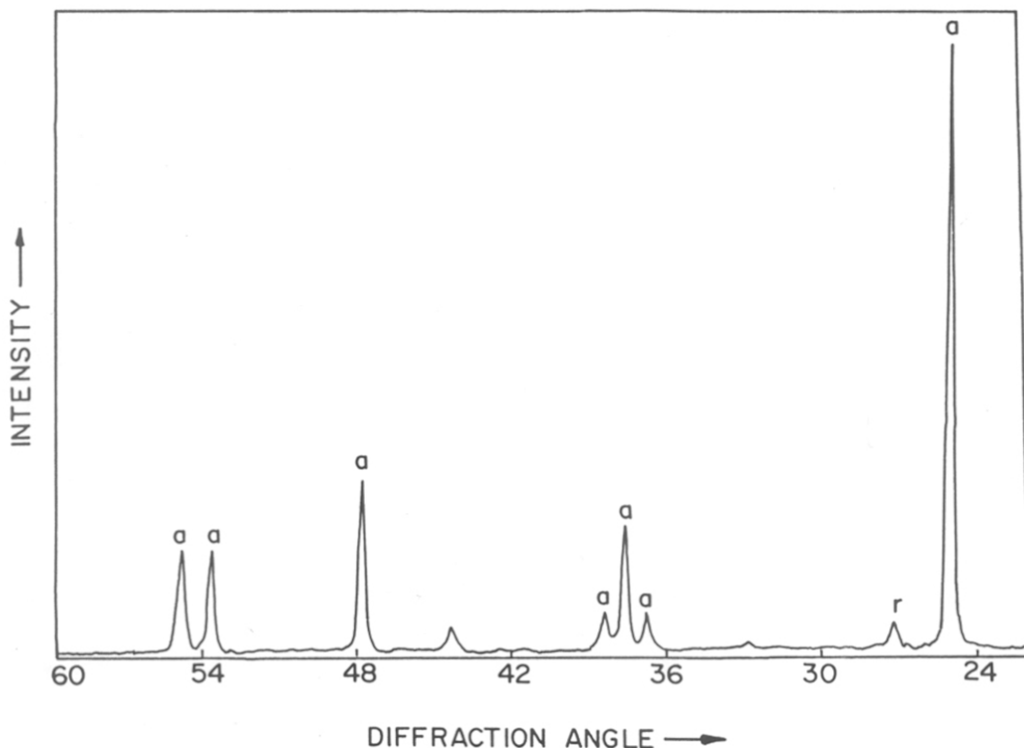

Figure 3.4 X-ray diffraction pattern of TNSB as dried powder showing anatase phase.

3.6 X-ray diffraction for Phase analysis

The samples are analyzed by X-ray diffraction to understand the phases evolved in the system as the sintering temperature increases. Figure **3.4** and **3.5** represent the X-ray diffraction pattern of these TiO_2 ceramics. Figure **3.4** is the X-ray diffraction pattern of the dried base composition. This shows the TiO_2 anatase phase(denoted by **a**) with a small trace of rutile phase(denoted by **r**). Since the amount of dopants are very small, the diffraction peaks corresponding to them are not found.

Figure **3.5** represents the X-ray diffraction pattern of the pellets sintered at 1100°C, 1250°C, 1300°C and 1350°C respectively. As the sintering temperature is raised to 1100°C , the evolution of rutile phase is seen. Table**3.2** represents the typical XRD peak positions, their relative intensity, corresponding hkl parameters of a TiO_2 rutile structure taken from the literature[JCPDS card No. 21-1276].

Table3.2 X-ray diffraction data of rutile TiO_2 from literature

d values	2θ	I / I_1	h k l
3.247	27.44	100	1 1 0
2.487	36.08	50	1 0 1
2.297	39.18	8	2 0 0
2.188	41.22	25	1 1 1
2.054	44.04	10	2 1 0
1.6874	54.32	60	2 1 1
1.6237	56.64	20	2 2 0
1.4797	62.74	10	0 0 2
1.4528	64.04	10	3 1 0
1.4243	65.48	2	2 2 1
1.3598	69.00	20	3 0 1
1.3465	69.78	12	1 1 2

The sample heated at 1100°C has all the major peaks corresponding to rutile structure [with major intensity peaks at 2θ = 27.45, 36.08, 41.22, 54.32 etc.]. There are small additional peaks corresponding to secondary phases which are formed during the reaction between the dopants with TiO_2. At 1100°C the secondary phases (represented by S) have very small intensity. The secondary peak occurring at 30.2 correspond to $Bi_2Ti_2O_7$.

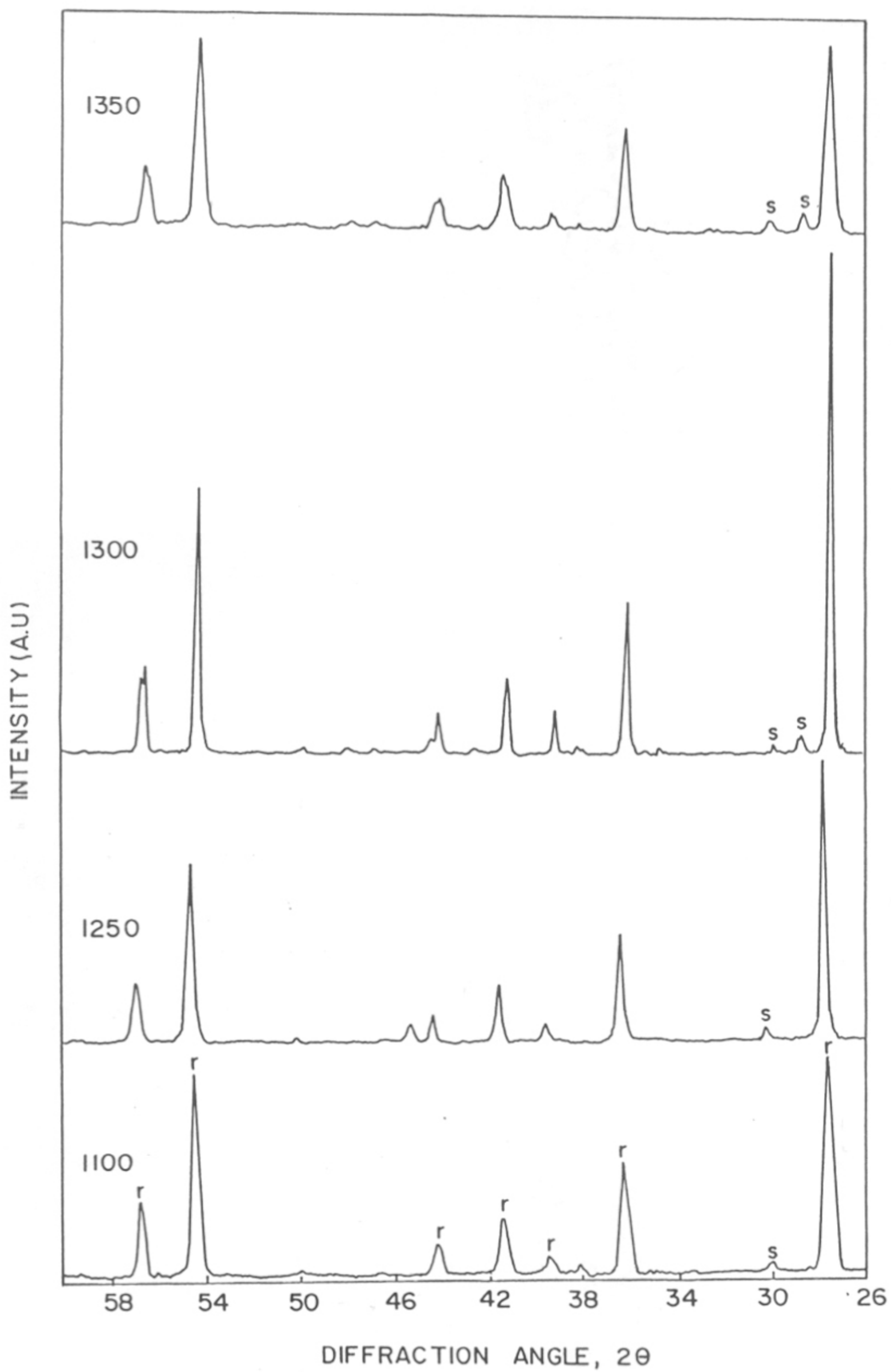

Figure 3.5 X-ray diffraction pattern of the TNSB pellets sintered at 1100°C, 1250°C, 1300°C and 1350°C

As the temperature is further increased to 1250°C, similar spectrum is obtained. At 1300°C another peak at 28.4° corresponding to $SrTi_4O_9$ is obtained. At 1350°C, the X-ray diffraction pattern looks similar to that observed at 1300°C. Hence it is concluded that these secondary phases are the phases which form the grain boundary layers. Also, there may exist $\propto$-Bi_2O_3 phase as found in the case of ZnO varistors. These phases are expected to create effective grain boundaries leading to double Schottkey barriers and hence the non-linear behaviour is attained. As the sintering temperature is raised to 1250°C and above, the intensity of the peaks corresponding to secondary phases have increased. Since the maximum intense peaks corresponding to rutile phase are very sharp, they must be representing TiO_2 grains and the secondary phases of Sr and Bi are expected to segregate at the grain boundaries and thereby make a better intergranular layer.

3.7 Scanning-Electron Micrographs of fractured surface

The TiO_2 ceramics sintered at 1100°C, 1200°C, 1250°C, 1300°C and 1350°C were characterized by the SEM. These micrographs were taken on the fractured surface and is given in figure**3.6**. The fractograph of the sample sintered at 1100°C shows grains of size less than 1μm and lot of voids are also seen. The grains are of needle shape and are distributed randomly. These voids were expected since the density of the sample is very small. As the sintering temperature increases , the grain size also increases. The average grain size of these samples is ~1μm. As the temperature of sintering is increased to 1250°C, the grain size increased to ~2μm. In this case, well defined uniform grain are seen unlike the sample at 1100°C. The grain size again increases to ~3μm. as the sintering temperature is further increased to 1300°C. At 1350°C the average grain size is around 6μm.

Table 3.3 Grain sizes and E_{gb} of TNSB samples

Sintering temperature (°C)	Grain size (μm)	E_{gb} (Volts)
1100	<1	-
1200	~1	-
1250	~2	0.240
1300	3	0.314
1350	6	0.415

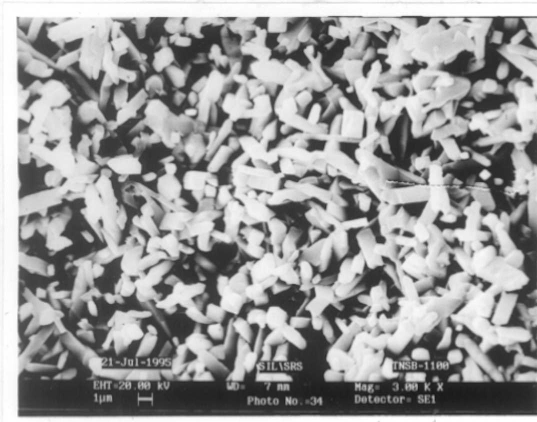

(a)

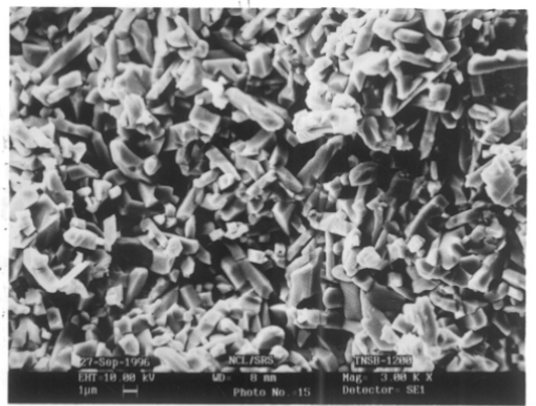

(b)

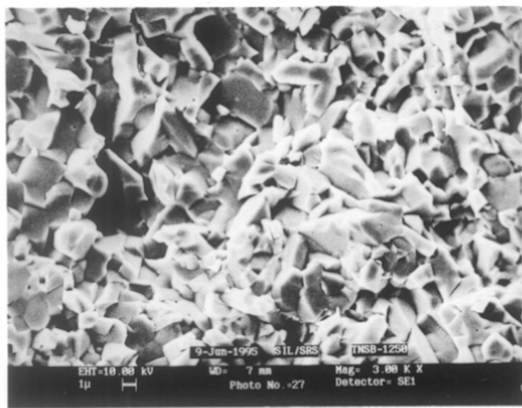

(c)

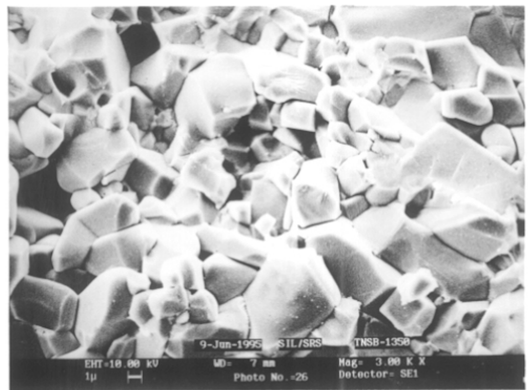

(d)

Figure3.6 Scanning electron micrographs of TNSB samples sintered at (a)1100°C, (b)1200°C, (c)1250°C, and (d) 1350°C

From the grain size obtained from the fractographs, the breakdown voltage per grain boundary for these TiO_2 samples were found out using the relation (1.5) given in Chapter**1**. The breakdown voltage (E_{gb}) thus obtained is given in Table**3.3** along with the grain size.

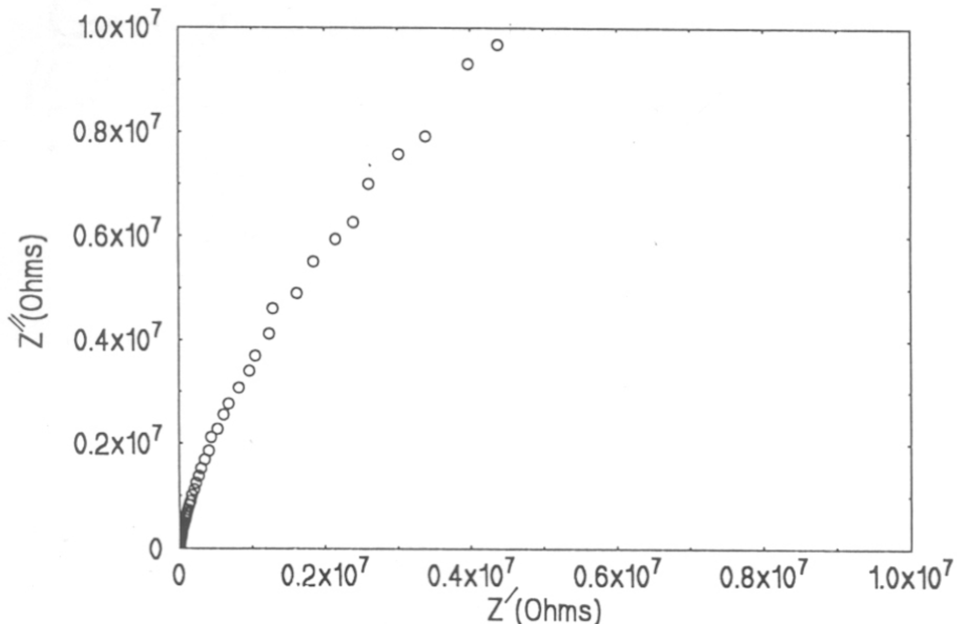

Figure 3.7 Impedance plots of TNSB(1300) sample measured at RT

3.8 Impedance Analysis

The a.c impedance analysis of the TiO_2 varistors are done within the frequency range of 10Hz to 32MHz. Figure**3.7** is the impedance plot (Z' vs Z'') measured at room temperature for the Sr doped TiO_2 sample sintered at 1300°C. The room temperature measurement lack a proper semicircular nature and thereby making it difficult to distinguish between the grain and grain boundary contributions. Hence the impedance spectra were recorded at higher temperatures also(up to T≈300°C).

Figure **3.8** represents the impedance plots of the sample measured at 100°C, 160°C, 200°C, 260°C and 300°C. As the measurement temperature increases, a clear semicircular plot

emerges due to the decrease in total resistance. The decrease in resistance is due to the fact that the material is highly semiconducting. At 300°C a full semicircle is seen. But these figures also fail to give an expected semicircular nature corresponding to the grains at the higher frequency side. This is due to the fact that the grain boundary contribution to the total resistance is very large compared to that due to the grains. Hence the semicircle corresponding to the grains is submerged in the circle representing the grain boundaries. Therefore, separating out the individual components by fitting the semicircle is not possible.

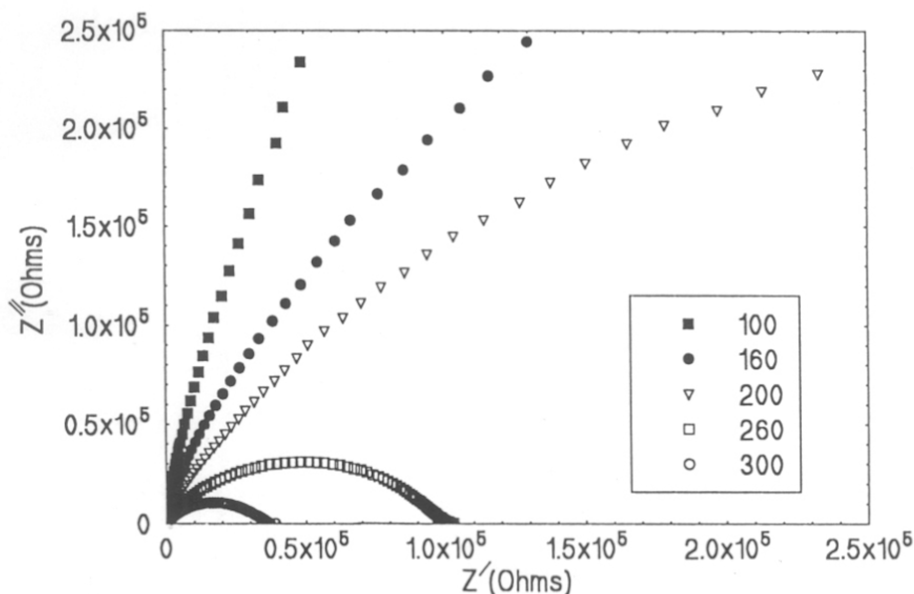

Figure 3.8 Impedance plots of TNSB(1300) sample measured at different temperatures.

This is the case in the other samples also which were sintered at 1250°C and 1350°C also. The impedance plots at different temperatures for TNSB samples sintered at 1250°C and 1350°C are given in Figures **3.9** and **3.10**.

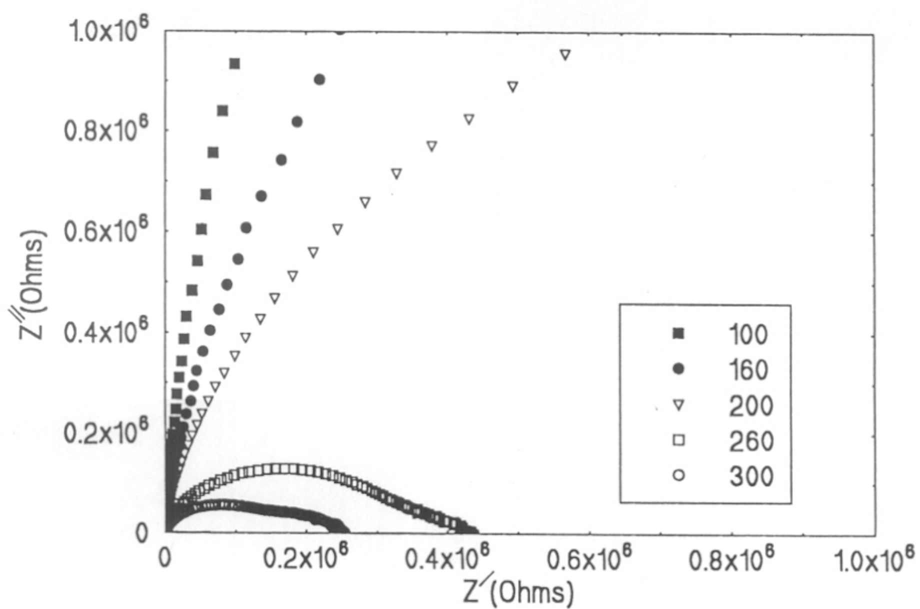

Figure 3.9 Impedance plots of TNSB(1250) sample measured at different temperatures.

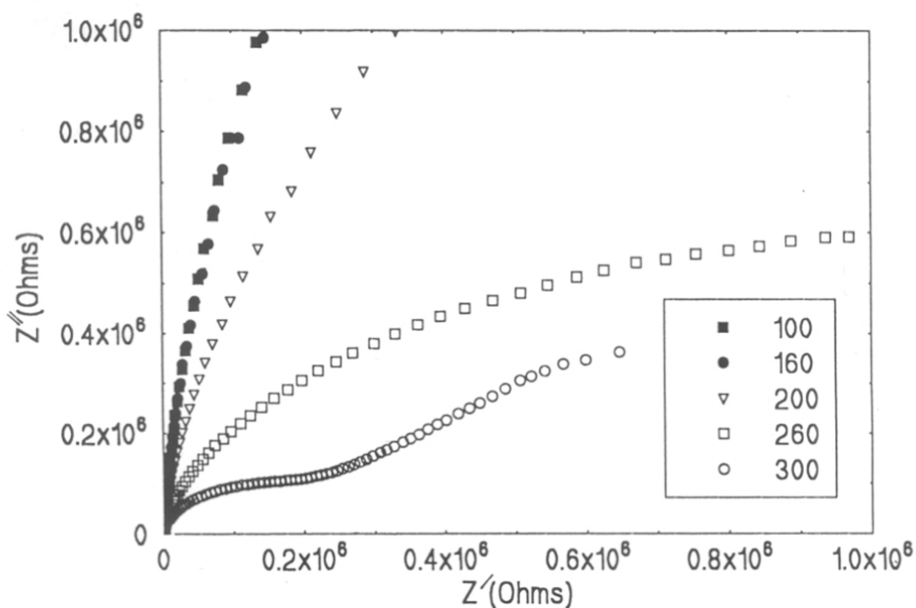

Figure 3.10 Impedance plots of TNSB(1350) sample measured at different temperatures.

Since the separation of the contributions from grain and grain boundaries is not possible from the above plots, the Bode diagrams were plotted to analyze the above data.

3.9 Bode plots

The Bode plots represent the logarithm of modulus of resistivity ($\log(|\rho|)$) against as the logarithm of frequency ($\log(f)$). The following approximations are taken to separate out the grain and grain boundary contributions.

$$\log_{f\to 0}|\rho| = \log_{f\to 0}(|\rho_{gb}|+|\rho_g|) = \log_{f\approx 0}(\rho_{gb}) \qquad \text{-------------------(3.1)}$$

since $\rho_{gb} >> \rho_g$, and

$$\log_{f\to\infty}(|\rho|) = \log(\rho_g) \qquad \text{--------------------(3.2)}$$

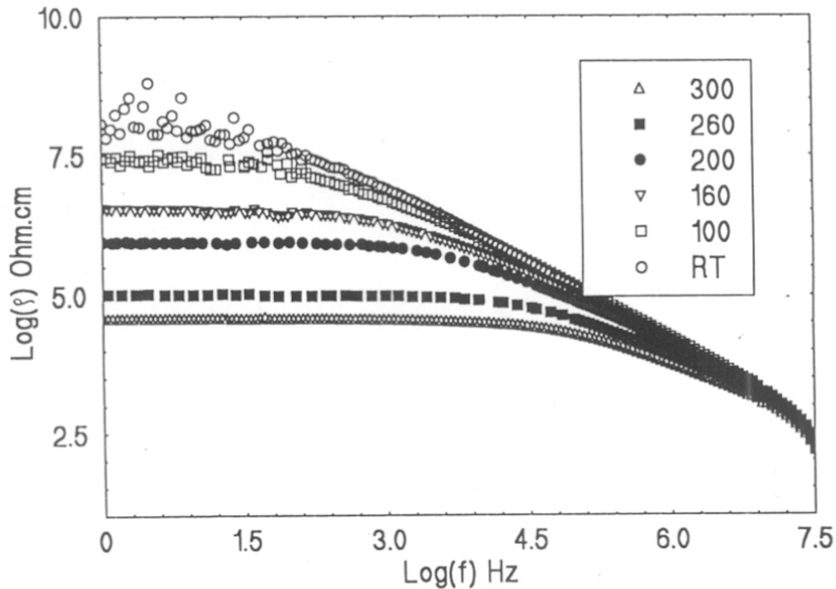

Figure 3.11 Bode plots of resistivity vs frequency for TNSB1300 sample at different temperatures.

The lowest frequency point is taken as the grain boundary resistivity and the highest frequency point as the grain resistivity. This is in accordance with the method used by

Longo *et al*[8]. The room temperature Bode plot shows a lot of fluctuation at the low frequencies. As the measurement temperature increases, the data points stabilize.

The Bode plots for the resisitivity(ρ) vs frequency of the sample sintered at 1300°C is given in Figure **3.11** and Bode plots between Phase angle and frequency for the same sample is given in figure**3.12**.

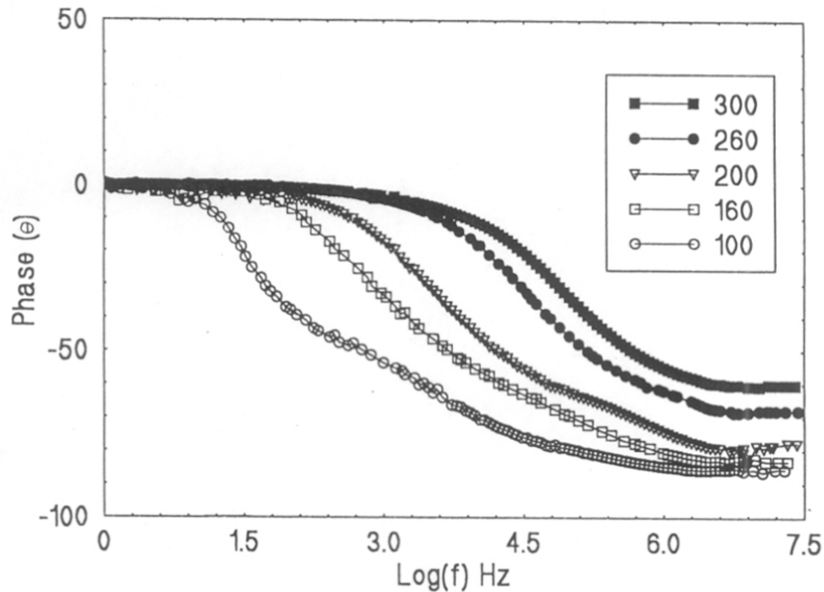

Figure 3.12 Bode plots of Phase vs frequency for TNSB1300 sample at different temperatures

Figure**3.11** shows that as the frequency increases there is a drastic drop in resistivity values [from ~10^8Ω.cm to 100Ω.cm]. This itself is an evidence for the presence of a grain boundary phase between the grains. At low frequencies, the sample exhibit a capacitance like behaviour, grain-grain boundary-grain structure, giving high resistance to the current flow. As the frequency increases, the resistance drastically decreases. i.e., the capacitive impedance ($X_c = 1 / \omega C$) decreases. At the highest frequency, the impedance corresponding to grain boundary will be negligible (i.e. X_c decrease) and the total resistivity will be contributed only by the grains. The above conclusion is further justified by the change in

phase with the frequency shown in figure**3.12.** The phase angle was 0° at low frequencies. But at the highest frequency point it has changed to -90°. This indicates the presence of a capacitive like behaviour.

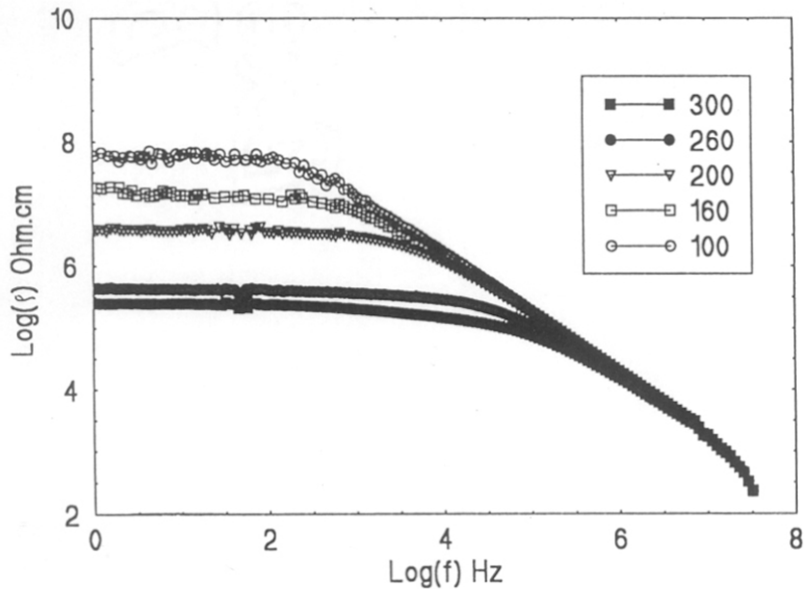

Figures 3.13 Bode plots of resistivity vs frequency for TNSB1250 at different temperatures.

Figures **3.13** and **3.14** are the corresponding Bode plots for the samples sintered at 1250°C and 1350°C respectively. These samples also shows similar behaviour to the 1300°C sintered samples and thereby indicating the presence of a grain boundary phases. The grain and grain boundary resistivities along with the corresponding grain boundary capacitance found from the above Bode plots are given in Table**3.4.**

In each of the cases, activation energy of the grain boundaries is estimated to find out whether there is any relation with the corresponding non-linear behaviour. The grain boundary resistivity measured at different temperatures were plotted in the Arrhenius curves shown in figure**3.15**.

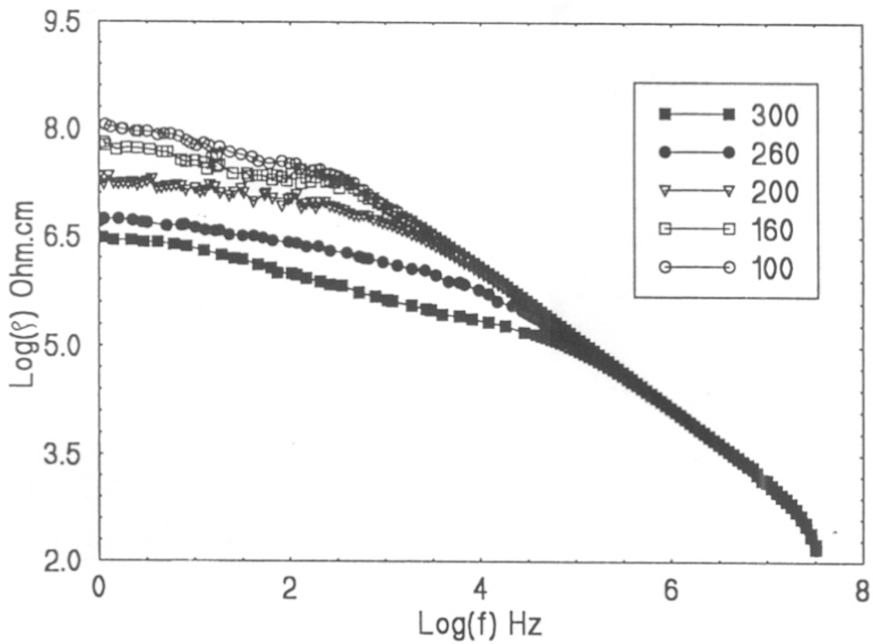

Figures 3.14 Bode plots of resistivity vs frequency for TNSB1350 at different temperatures

Table 3.4 ρ_g, ρ_{gb} and C_{gb} values of TNSB samples from impedance plots.

Sample	Measurement Temperature (°C)	ρ_{gb} (Ohm.cm)	ρ_g (Ohm.cm)	C_{gb} (f.cm^{-2})
1250	100	7.76×10^{7}	229.08	--
	160	1.62×10^{7}	229.08	9.81×10^{-12}
	200	3.98×10^{6}	239.88	8.17×10^{-12}
	260	4.47×10^{5}	234.42	7.80×10^{-12}
	300	2.57×10^{4}	223.87	5.40×10^{-12}
1300	100	2.82×10^{7}	204.17	2.465×10^{-11}
	160	3.31×10^{6}	199.53	1.746×10^{-11}
	200	8.71×10^{5}	190.54	1.746×10^{-11}
	260	1.02×10^{5}	165.96	1.707×10^{-11}
	300	3.72×10^{4}	138.04	1.554×10^{-11}
1350	100	8.52×10^{7}	154.86	--
	160	5.75×10^{7}	154.86	1.71×10^{-11}
	200	1.82×10^{7}	154.86	8.75×10^{-12}
	260	5.49×10^{6}	173.78	4.19×10^{-12}
	300	5.02×10^{6}	181.97	5.77×10^{-12}

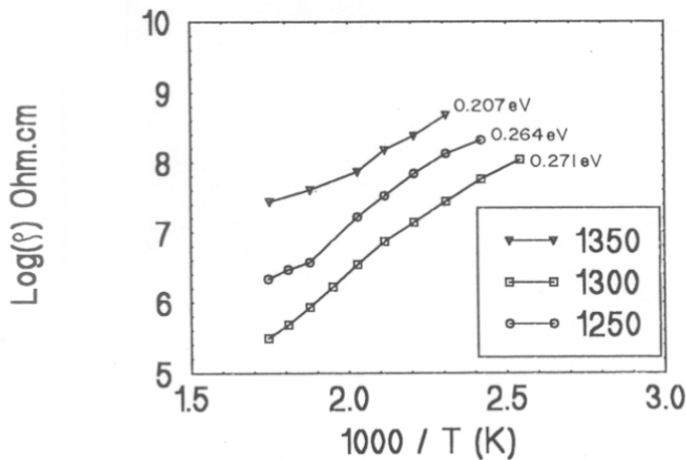

Figure 3.15 Arrhenius plots of TNSB samples plotting resistivity vs 1000/T

The grain boundary resistivity and the temperature is related by the following Arrhenius equation

$$\rho_{gb} = \rho_{gbo} \exp(-E_A / K_B T) \qquad \text{------------------(3.3)}$$

where K_B is the Boltzmann constant, E_A the activation energy, T is the measuring temperature in °K, and ρ_{gbo} is the grain boundary resistivity at 0°K.

From equation (3.3)

$$\log(\rho_{gb}) = -E_A / K_B T \qquad \text{------------------(3.4)}$$

The slope of the curve log (ρ_{gb}) vs 1/T gives the value corresponding to E_A/K_B and hence the activation energy is calculated. The activation energy thus calculated from figure**3.15** is indicated near to corresponding curve. It is seen that the 1300°C sintered sample have the largest activation energy of 0.271eV. The 1250°C sintered sample have almost equal activation energy of 0.264eV and the 1350°C sintered sample have a grain boundary activation energy of 0.207eV. This is similar to the variation in non-linear coefficient values measured from the I-V characteristics. Hence the large value of grain boundary activation

energy points at a better intergranular grain boundary region leading to superior current-voltage characteristics.

3.10 TiO_2 voltage sensors doped with Ca^{2+}, Ba^{2+}, Mg^{2+} in place of Sr^{2+}

In this section, the effect of Ca^{2+}, Ba^{2+} and Mg^{2+} dopants on the I-V characteristics when they replace Sr^{2+} in the previously described TiO_2 voltage sensor. Ca, Ba and Mg added separately in the same concentration as Sr^{2+}. These samples are denoted as TNCB, TNBB and TNMB. All the samples were prepared by the conventional ceramic route as described in section **2.2.1**.

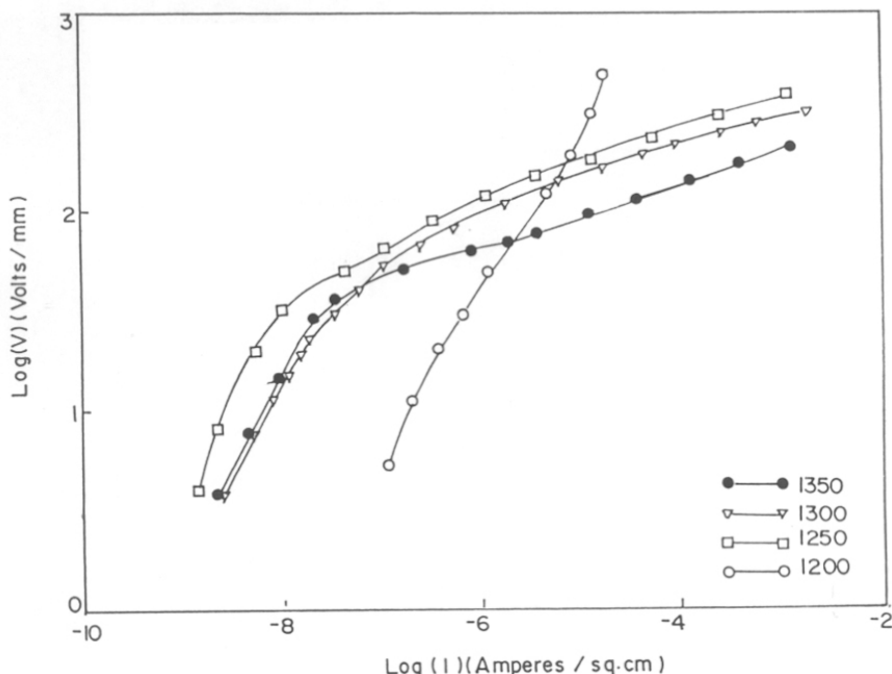

Figure 3.16 Current-voltage (I-V) characteristics of TNBB samples.

3.10.1 Current-voltage (I-V) characteristics

The current-voltage characteristics of TNBB samples are given in figure**3.16**. The TNBB samples do show relatively good non-linear behaviour, similar to TNSB samples. The TNBB sample sintered at 1200°C doesn't show any non-linear behavior. As the sintering

temperature is raised to 1250°C, the sample exhibited good non-linear behaviour with an ∝ =5.74 and E_{1mA} = 380volt/mm. Similar to TNSB samples, TNBB samples also gave the best non-linearity when the sample was prepared at the sintering temperature of 1350°C. At this temperature ∝=7.04 and E_{1mA} = 309volts/mm. As the sintering temperature is further increased to 1350°C, both ∝ and E_{1mA} decreases to 5.85 and 245volts/mm, respectively. The decrease in breakdown voltage with increase in sintering temperature is a direct consequence from the corresponding increase in grain size.

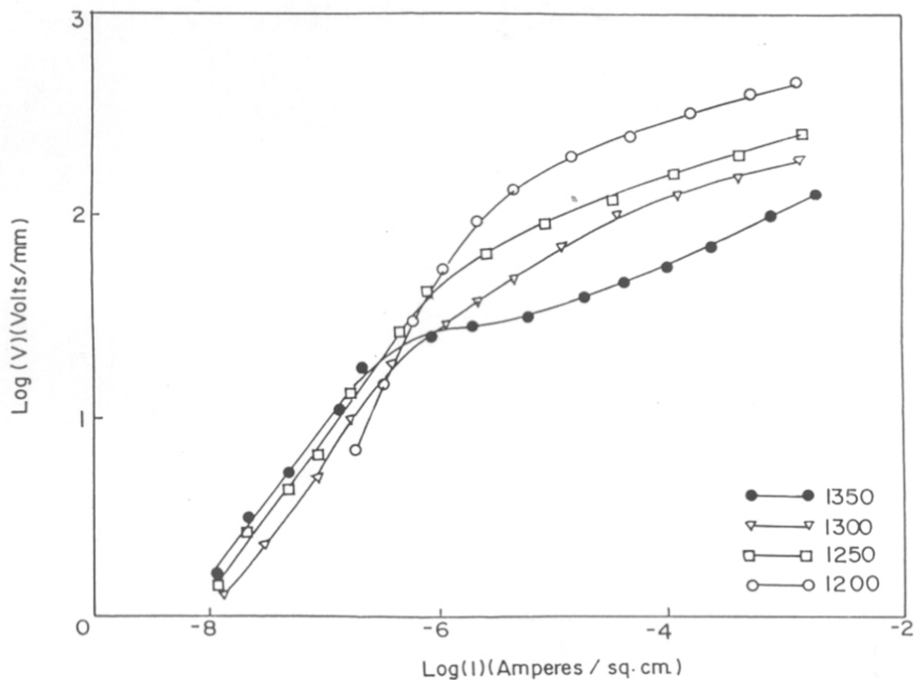

Figure 3.17 Current-voltage (I-V) characteristics of TNCB samples

Figure **3.17** represents the current-voltage (I-V) characteristics exhibited by TNCB samples sintered at different temperatures. One difference between the Ba or Sr doped sample with this sample is that TNCB sample shows non-linear behaviour at 1200°C sintering temperature also. In this case ∝ =4.97 and E_{1mA} = 446volts/mm. As the sintering temperature is increased to 1250°C, the ∝ value increased to 5.05 and E_{1mA} = 251volts/mm. At 1300°C also, there is not much change in ∝ value. i.e., ∝=5.07 an the corresponding

breakdown voltage is E_{1mA}=186volts/mm. As the sintering temperature is further increased to ∝ decrease to 3.8 and E_{1mA} to 122volts/mm. As in the previous cases, the increase in grain size with sintering temperature leads to a corresponding decrease in the breakdown voltage. The TNCB samples also shows similar non-linear behaviour to TNSB and TNBB samples eventhough the breakdown voltages of these samples differ. This difference in breakdown voltages is due to inhomogeneous mixing as well as the chemical nature of dopants.

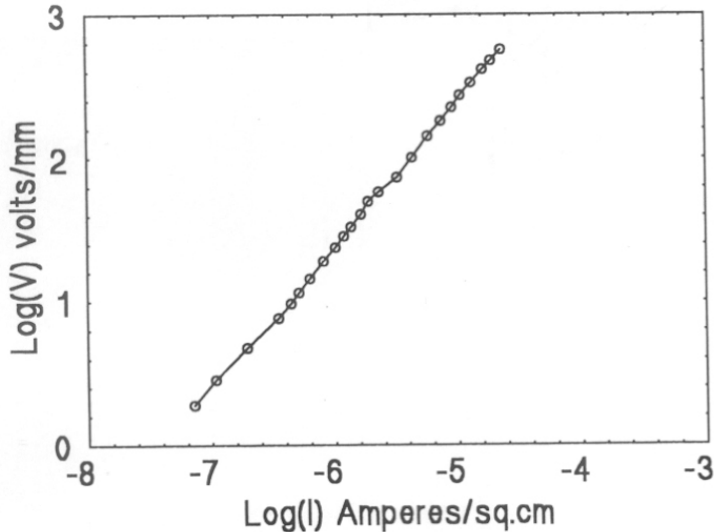

Figure 3.18 Current-voltage (I-V) characteristics of TNMB sample

Table 3.5 Performance parameters of TNBB, TNCB and TNMB samples

Sample name	Sintering temperature(°C)	non-linear coefficient (∝)	Breakdown voltage (E_{1mA}) volts/mm
TNBB	1200	1.40	--
	1250	5.75	380
	1300	7.04	309
	1350	6.87	155
TNCB	1200	4.97	446
	1250	5.05	251
	1300	5.07	186
	1350	3.81	112
TNMB	1250	1.04	--

Figure **3.18** represents the current-voltage behaviour of TNMB sample sintered at 1250°C. This sample doesn't show non-linear characteristics at the sintering temperature range employed in this study. The I-V curve exhibited a linear behaviour with an ∝ value of 1.04. At other sintering temperatures, the I-V curves exhibited more or less the same behavior as given in figure **3.18**. The performance parameters obtained for the TNBB, TNCB and TNMB samples, as found from the I-V characteristics, are given in Table**3.5**

TNBB, TNCB and TNMB samples were further characterized by XRD, SEM and the results are discussed below.

3.10.2 Density

Ba doped samples(TNBB)

The density of the Ba doped samples are determined by measuring the weight and dimensions of the disc shaped samples. As the sintering temperature increases, the density also increases. At 1200°C, the density is very low, 3.75 gm/cc. When the temperature is increased to 1250°C, the density increases to 3.94 gm/cc. At 1300°C and 1350°C, this value remains more less as constant, i.e., 3.92gm/cc and 3.91gm/cc respectively. A slight decrease in the density of 1300 and 1350°C can be due to the loss of Bi which vaporizes at higher temperatures.

Ca doped samples(TNCB)

The density of the Ca doped samples also exhibit similar behaviour to Ba dopes samples. At sintering temperature 1200°C, the sample have a density of 3.8gm/cc. The increase of sintering temperature to 1250°C increases the density to 3.91 gm/cc. At 1300°C, the maximum density of 3.94gm/cc was attained. A further increase in temperature decreases the density to 3.9gm/cc. This decrease in density at the high temperatures is due to the loss in Bi at high temperatures.

Mg doped sample(TNMB) The TNMB sample sintered at 1250°C had a poor density of 3.56gm/cc. Since the sample doesn't give any nonlinear nature, other density values are not reported here.

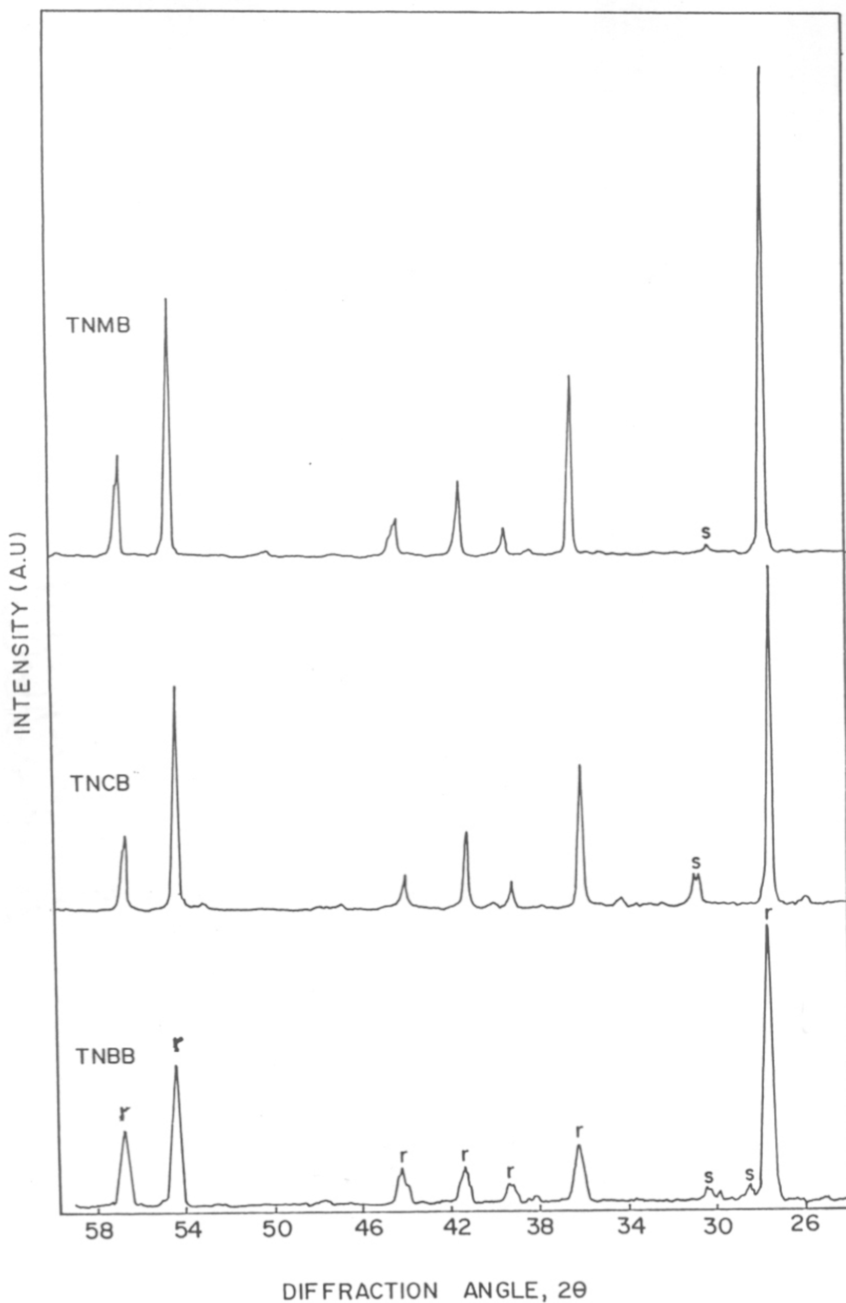

Figure 3.19 X-ray diffraction pattern of TNBB, TNCB and TNMB samples sintered at 1250°C

3.10.3 Phase analysis by X-ray diffraction

Figure **3.19** represents the X-ray diffraction pattern of the Ca, Ba and Mg doped TiO_2 varistors sintered at 1250°C. The X-ray diffraction pattern of Ba and Ca doped samples show similar pattern to the Sr doped samples exibiting the rutile structure of TiO_2. The secondary phases (at 30.2°) are seen in the diffraction pattern which are similar to that described in Sr doped sample. The X-ray diffraction pattern also points out that there is no difference in the crystal structure behaviour nature of these TiO_2 varistors irrespective of whether the dopant is Ca, Ba or Sr. The Mg doped sample also shows similar X-ray diffraction pattern.

3.10.4 Scanning Electron micrographs of fractured surface

a). <u>Ba doped samples</u>

Figure **3.20** shows the SEM picture of the TNBB sample which shows a clear grain boundary phase. This is a clear evidence that grain boundary phase is formed during sintering.

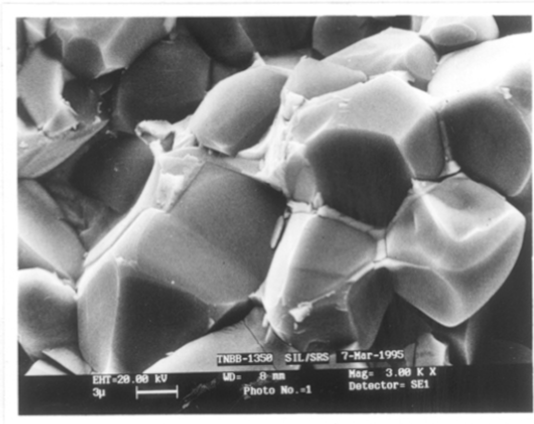

Figure 3.20 SEM fractograph of the TNBB sample

Figure **3.21** shows the SEM fractographs of the Ba doped TiO_2 varistors sintered at different temperatures. The samples sintered at 1200°C shows needle shaped particle of ~1μm size. There are large number of voids reflected in the density of the sample. As the sintering temperature increases, the grain size increases to ~2μm. Also the grain shape changes from a rectangular one to a more square one. At 1250°C also, voids were seen. At 1300°C, the

average grain size further increases to 3μm and the grain size distribution is more uniform. At 1350°C, the grain size again increases to 6μm and one can see well defined grains.

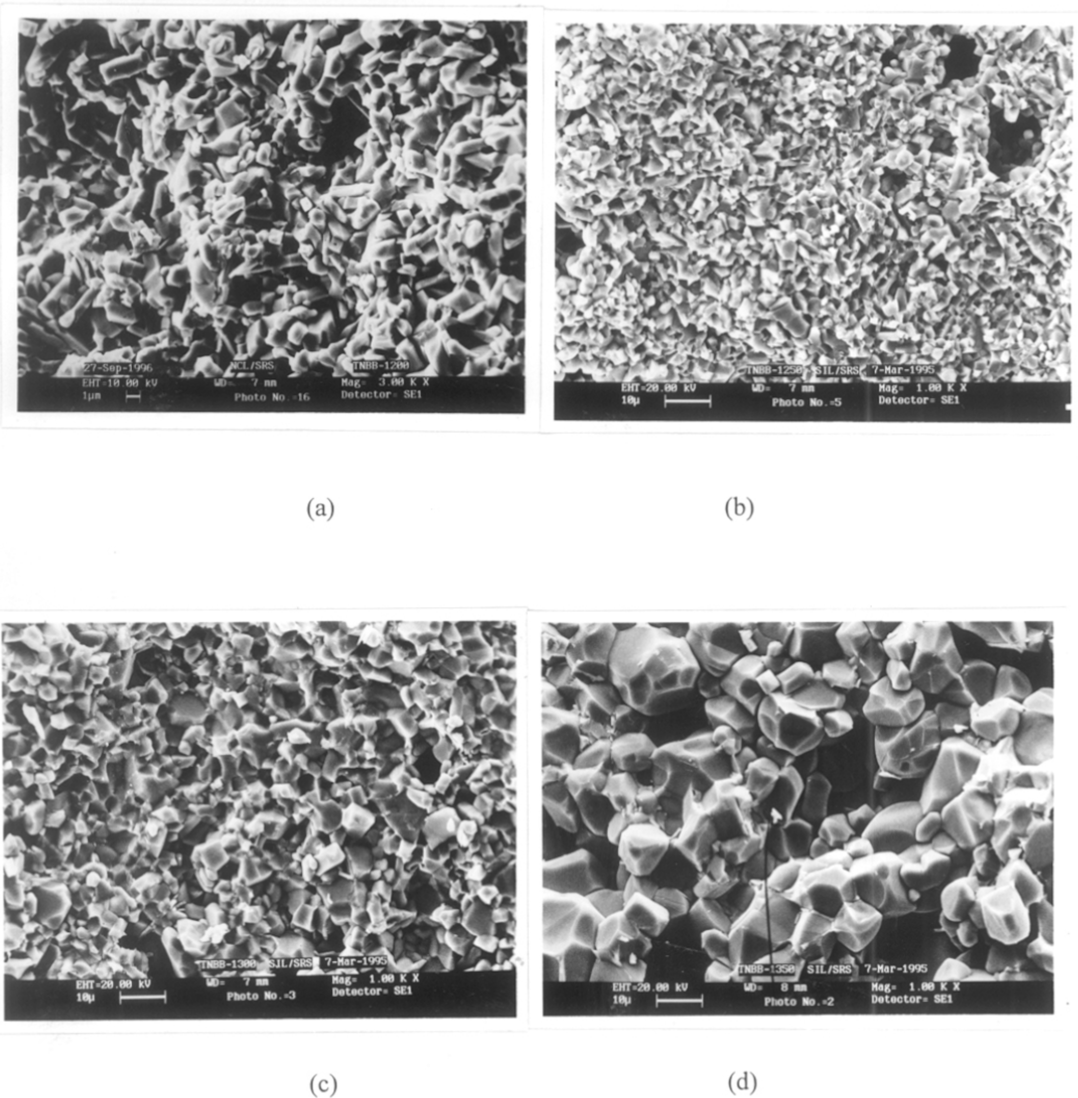

Figure 3.21 SEM fractographs of TNBB samples sintered at (a)1200°C, (b)1250°C, (c)1300°c and (d) 1350°C

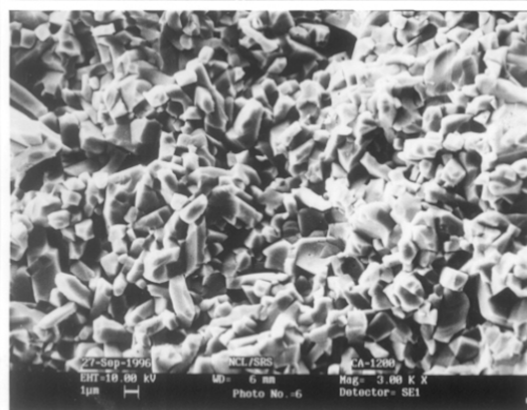

(a)

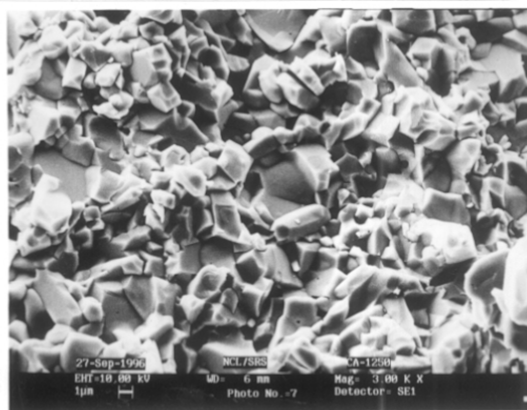

(b)

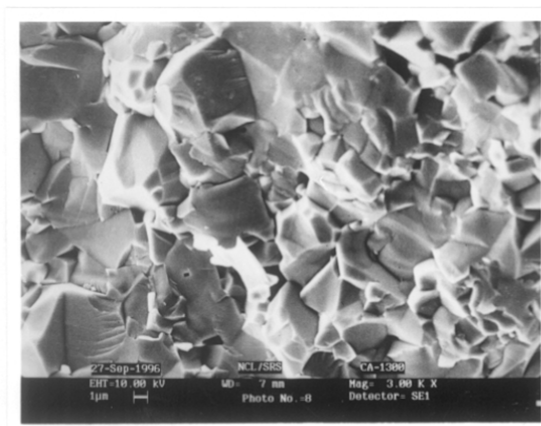

(c)

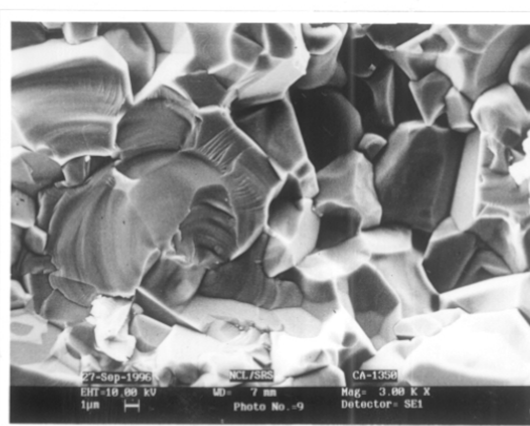

(d)

Figure 3.22 SEM fractograph of the TNCB samples sintered at (a)1200°C, (b)1250°C, (c)1300°C and (d)1350°C.

b). Ca doped samples

The SEM fractographs of the Ca doped samples are given in figure **3.22**. It shows similar behaviour to the previously described Sr and Ba doped samples. At 1200°C, the sample shows ~1μm grains with a large number of voids. As the temperature is increased to 1250°C, the grain size also increases to ~2μm. At 1300°C, the average grain size again increases to ~4μm and at 1350°C, the average grain size is ~6.5μm. But at this temperature the grain size distribution is non-uniform. Abnormal grain growth is seen at certain sections of the sample.

From the SEM micrographs of the samples doped with Sr or Ba or Ca, microstructural distribution remains more or less the same.

(c) Mg doped sample

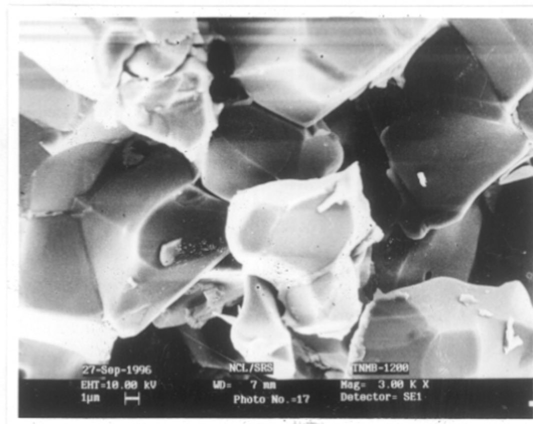

Figure 3.23 SEM fractograph of the TNMB sample sintered at 1250°C

Since the Mg doped sample didn't show any non-linear behaviour characteristics, only the SEM fractograph of the Mg sample sintered at 1250°C is shown in figure**3.23**. It had a larger grain size than the other samples (Sr,Ba, Ca doped). At 1250°C, the average grain size is ~5.5μm. This increase in grain size may be due to the fact that Mg acts as a grain growth enhancer in TiO_2 system.

The grain size observed from the micrographs for the above 3 samples are given in Table **3.6.**

Table 3.6 Grain sizes* of the TNBB, TNCB and TNMB samples

Sample	1200°C	1250°C	1300°C	1350°C
TNBB	~1	~2	~3	~6
TNCB	~1	~2	~4	~6.5
TNMB	--	~5.5	--	--

*Grain sizes given in μm.

3.11 Chemically synthesized TiO_2 voltage sensor.

The chemical method of synthesis of TiO_2 voltage sensor doped with Sr^{2+} was described in Chapter**2**. The electrical contacts were given and other measurements were done similar to the ceramic samples.

3.11.1 Current-voltage (I-V) characteristics

Figure**3.24** plots the current-voltage characteristics of the chemically prepared sample which were sintered at 1200°C, 1250°C, 1300°C and 1350°C respectively. The I-V curves were plotted in the log-log scale and the performance parameters obtained from this I-V data are given in Table**3.7**.

Table 3.7 Performance parameters of the chemically synthesized TiO_2 varistor.

Sintering temperature (°C)	non-linear coefficient (∝)	Breakdown voltage E_{1mA} (volts/mm)
1200	4.69	100
1250	8.13	66
1300	6.94	57.5
1350	3.25	40.7

At 1200°C, the sample gave relatively good non-linear behaviour with an ∝ value of 4.69 and the breakdown voltage is E_{1mA} = 100volts/mm. As the sintering temperature is increased to 1250°C, ∝ value also increases to 8.13 and E_{1mA} decreases to 66 volts/mm. The 1250°C sintered sample gave the best non-linear coefficient. Compared to the 1200°C sample, the 1250°C sample have a lower prebreakdown current. This indicates a better grain boundary impedance and hence a better energy barrier.

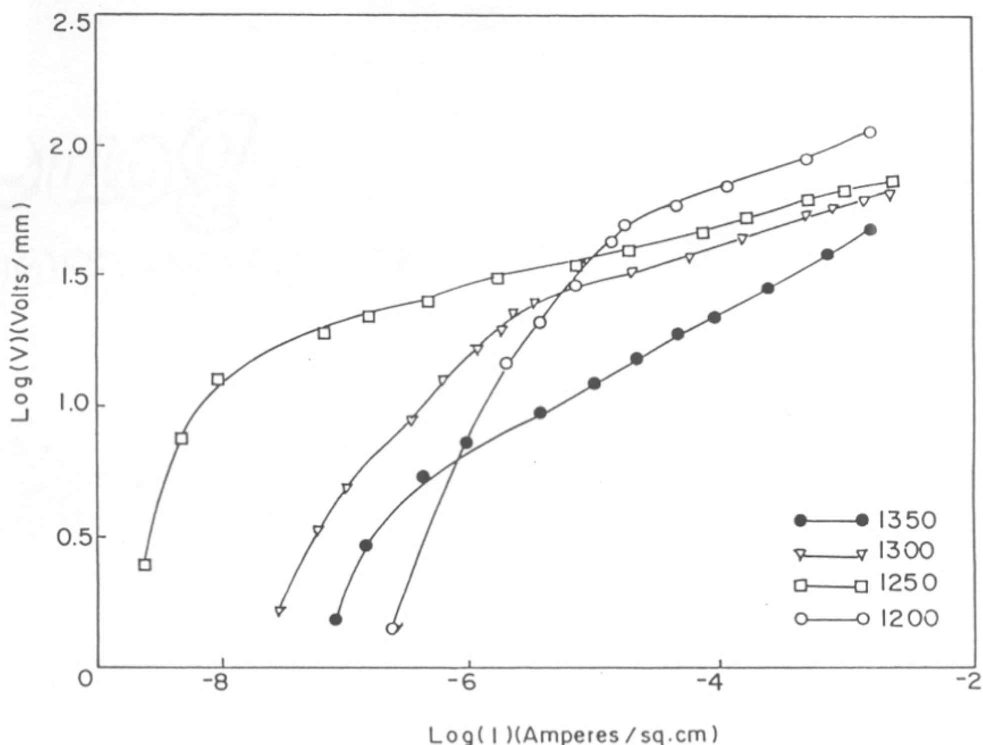

Figure 3.24 Current-voltage (I-V) curves of the chemically synthesized TiO_2 voltage sensors

As the sintering temperature is increased to 1300°C, ∝ and E_{1mA} decrease to 6.94 and 57.5 volts/mm respectively. This decrease is a direct consequence of the increase in grain size with increase in sintering temperature. At 1350°C, the non- linearity still diminishes with an ∝ value of 3.25 and breakdown voltage E_{1mA} = 40.73volts/mm. Compared to 1250°C sintered sample, all the other three sample have higher prebreakdown currents indicating inferior grainboundary region or inferior energy barrier to electronic conduction.

3.11.2 DTA/TGA analysis

The well mixed as-dried chemically prepared powder was subjected to DTA/TGA/ DTG analysis and the corresponding curves are shown in Figure **3.25**. The DTA curve showed endothermic loss(9.87%) in the temperature range 30-190°C, which is due to loss of adsorbed and bound water. The second endothermic loss (9%) in the temperature range 190-730°C is attributed to decomposition of titanium hydroxide and formation of TiO_2. The thermal change at 730-820°C is due to loss of Bi due to evaporation and leading formation of TiO_2 powder.

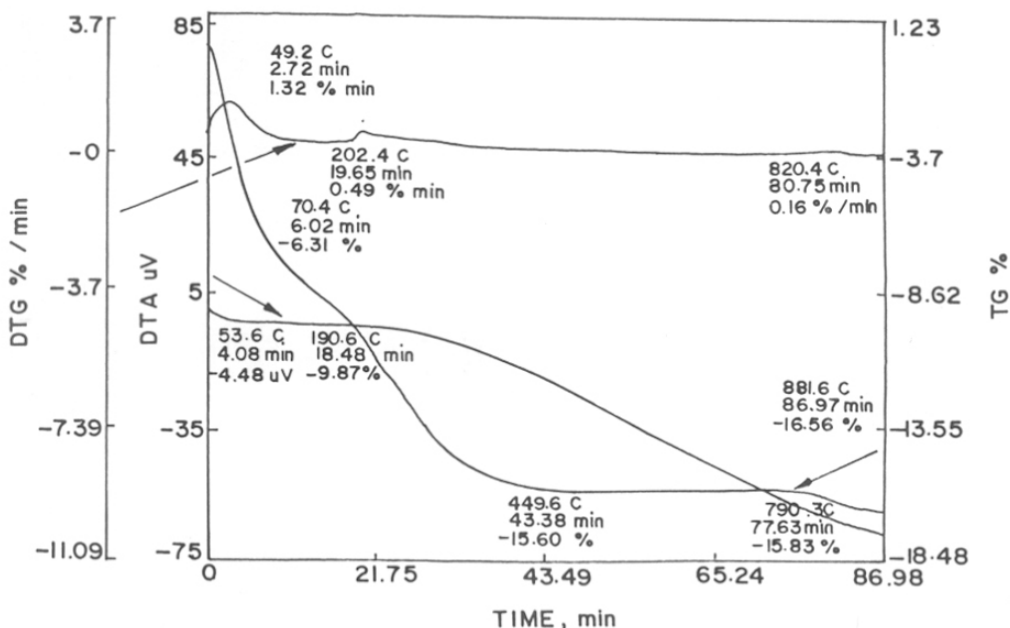

Figure 3.25 DTA/TGA/DTG curves of the chemically prepared TiO_2 varistor powder.

3.11.3 Density

Density of this chemically prepared samples are found by measuring the mass and the dimensions of the sintered pellets. Surprisingly, all the samples showed poor density. At 1200°C, the density was found to be 3.44gm/cc. As the temperature is increase to 1250°C, the density also increases slightly to 3.47gm/cc. At 1300°C, the density further increases to 3.51gm/cc. When the sintering temperature is 1350°C, the density was found to decrease to 3.34gm/cc. The amorphous(hydrolyzed) powder was difficult to press into dense compacts

resulting in poor density at the green stage. No attempt was made to optimise either the sintering conditions or use of densifying additives. The poor density of these samples may also be due to the evaporation of Bi dopants which acts as a good densifying agent in TiO_2. Since there are two stages of heating, i.e., calcining at 500°C and sintering at various temperatures, there may be considerable loss of Bi. This low density is probably the reason for no improvement in the non-linear behaviour.

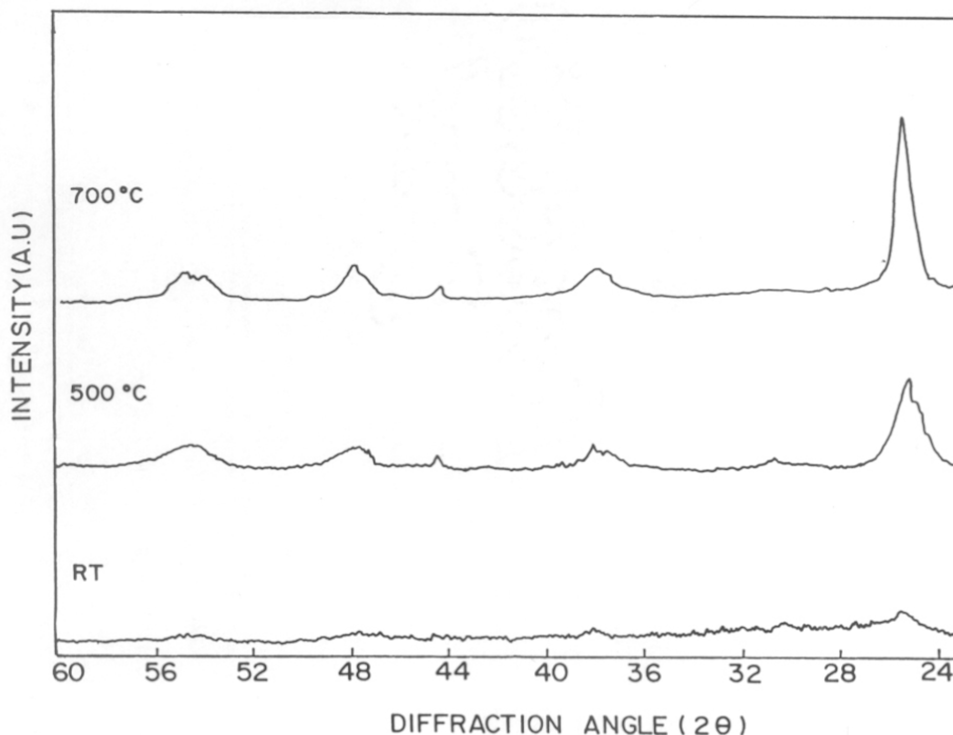

Figure 3.26a X-Ray Diffraction patterns of the chemically prepared sample at RT, 500°C and 700°C.

3.11.4 Phase analysis by X-ray diffraction

Figure **3.26a** is the X-ray diffraction pattern of the chemically prepared sample, i.e., those of the as dried powder as well as those calcined at 500°C and 700°C. At RT, dried powder exhibits an amorphous nature as shown by the unresolved structure in the X-ray diffraction

pattern except the small broad peak at 2θ = 25°. At 500°C, the anatase phase is clearly defined in the XRD peaks. The peaks are more sharpened in this case indicating the increase

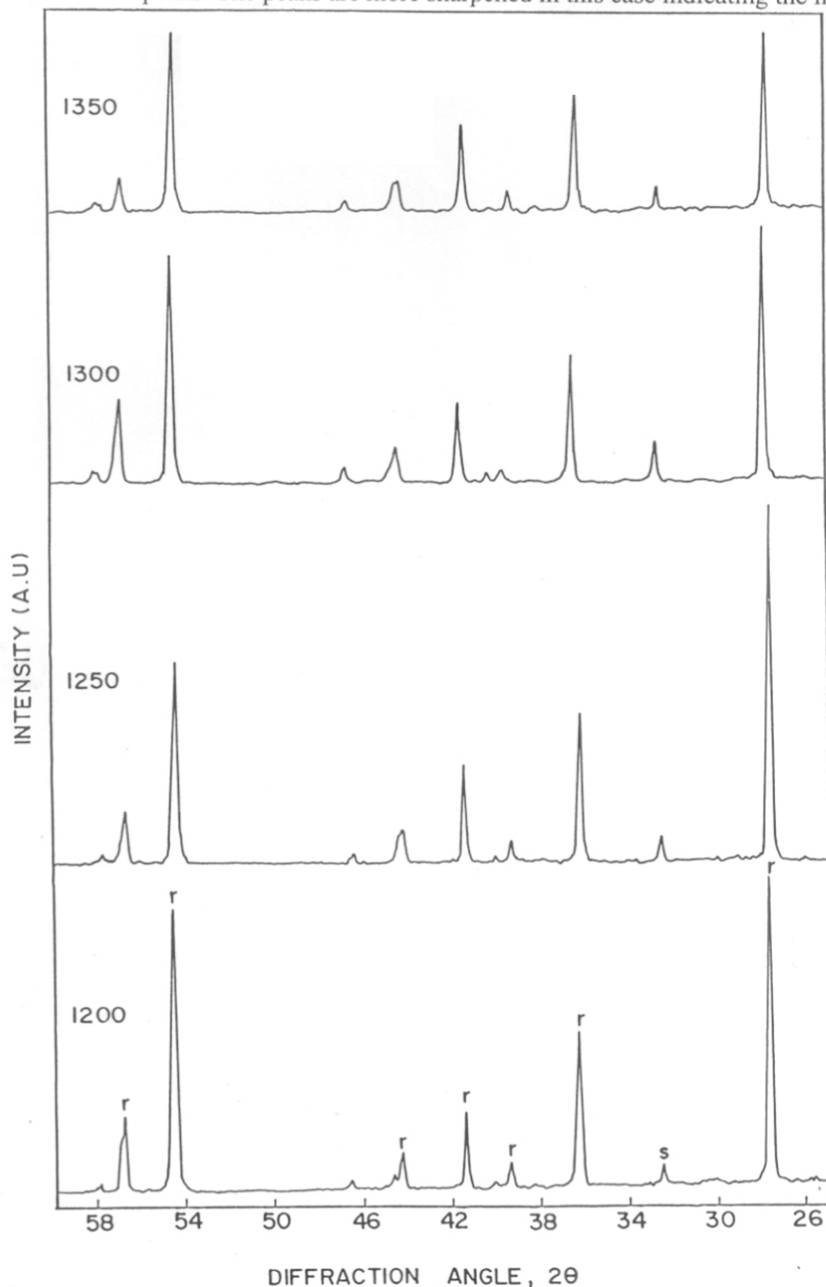

Figure 3.26b X-Ray Diffraction patterns of the chemically prepared sample sintered at 1200,1250,1300 and 1350°C.

ion particle size. As the calcining temperature is increased to 700°C, the particle size increases and hence sharper peaks corresponding to anatase phase is seen.

Figure **3.26b** is the X-ray diffraction pattern of the samples, first calcined at 500°C and then sintered at 1200°C, 1250°C, 1300°C and 1350°C respectively. All the samples shows the TiO_2 rutile phase with small amounts of secondary phase at 33°C. The secondary phases at 30.2° and 28°, corresponding to $Bi_2Ti_2O_7$, observed in the case of Sr doped sample prepared by ceramic route is absent in this case. This is due to the loss of Bi during the 2 stages of heating.

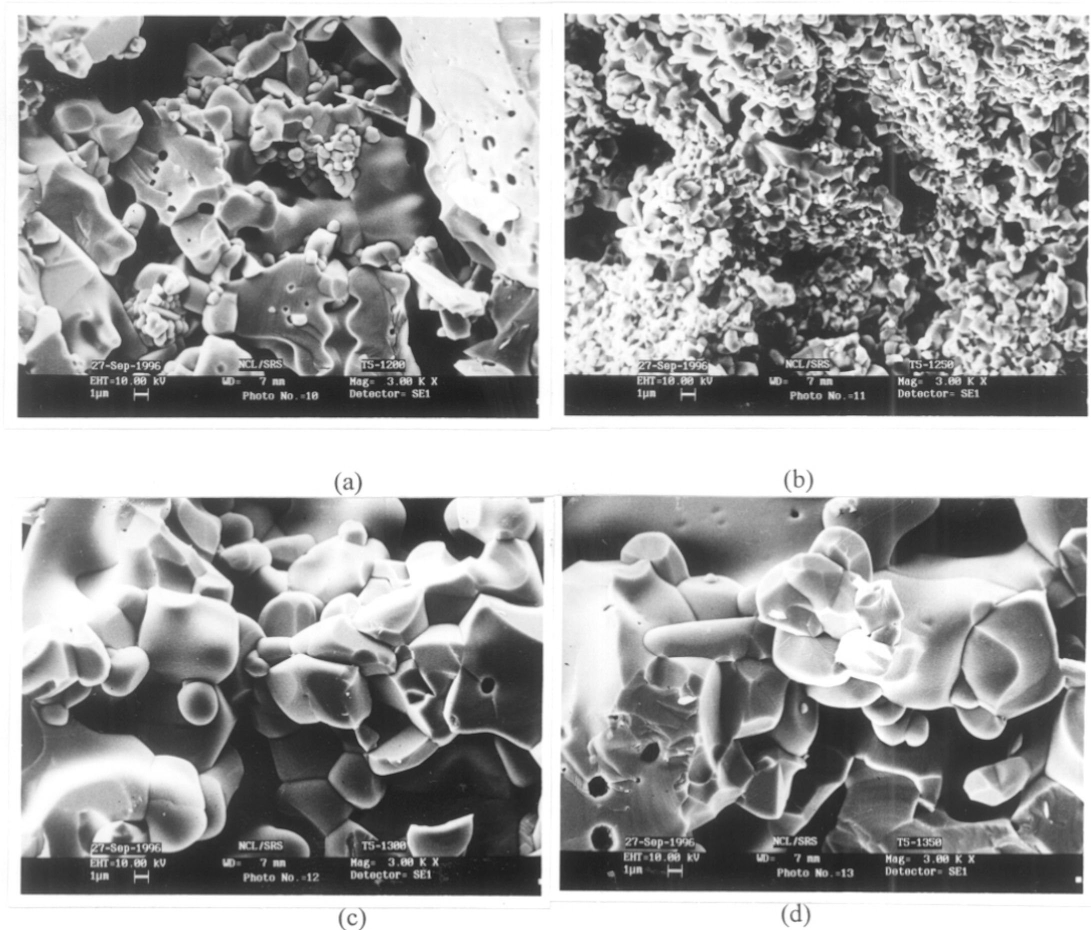

Figure 3.27 Scanning Electron micrographs of chemically prepared samples sintered at (a)1200°C, (b)1250°C, (c)1300°C and (d)1350°C.

3.11.5 Scanning Electron Micrographs of fractured surface

Figure **3.27** is the SEM fractographs of chemically prepared samples sintered at 1200°C, 1250°C, 1300°C and 1350°C. All the samples have voids seen in it pointing at the low density of the samples. Very small grains $<1\mu m$ and bigger grains $\sim 4\mu m$ are also seen at certain section of the sample sintered at 1200°C. At 1250°C, most of the grains are 1μm in size, but abnormally large grains are also seen. Voids are also seen at certain sections of the sample. As the sintering temperature isincreased to 1300°C, the average grain size increases to 3.5μm. Here also larger grains are seen. Voids are also present in this sample. Similar behaviour is shown by the 1350°C sintered sample with an average grain size of 6μm. The microstructure of the chemically prepared sample was found to be non-uniform and the large amount of voids present in the sample is the reason for low density.

The micrographs shown in figure **3.27** points at a non-uniform microstructure with a large number of voids. This non-uniform microstructure is the reason for the poor performance parameters observed in the current-voltage behaviour of the respective samples.

3.12 Discussion

The current-voltage characteristics of the Sr doped TiO_2 varistor have proved to be relatively good non-linear resistors with low breakdown voltages. 1300°C was found to be the optimum temperature for sintering. This is related to the formation of an effective grain boundary barrier layer or energy barrier. The addition of donor and acceptor dopants are the major factors which determines the creation of the effective grain boundary.

The donor dopant, Nb, doesn't have any precipitated effect, as found from XRD and SEM, and they dissolve in TiO_2 lattice. Nb^{5+} replaces Ti^{4+} to give an extra electron to the conduction process, and thereby increase the conductivity.

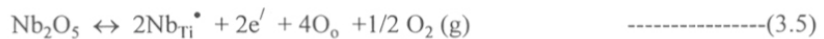

$$Nb_2O_5 \leftrightarrow 2Nb_{Ti}^{\bullet} + 2e' + 4O_o + 1/2\, O_2\,(g) \qquad \text{----------------(3.5)}$$

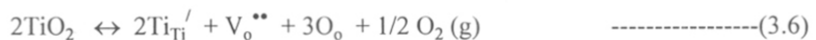

$$2TiO_2 \leftrightarrow 2Ti_{Ti}' + V_o^{\bullet\bullet} + 3O_o + 1/2\, O_2\,(g) \qquad \text{-----------------(3.6)}$$

The electron usually combines with regular titanium lattice ion and form Ti_{Ti}'. The dissolution of niobium into TiO_2 ceramics increased the concentration of e' which is

equivalent to $Ti_{Ti}^{/}$ and local oxygen partial pressure, which in turn tend to decrease the concentration of oxygen vacancies.

The presence of Nb^{5+} which has a valence greater than Ti^{4+}, leads to the presence of one Ti^{3+} ions, to preserve the charge neutrality of the system. Since the electron affinity of Ti^{4+} is greater than that of Nb^{5+}, charge neutrality is preserved by creation of Nb^{5+}-Ti^{3+} pair. Since the dielectric constant of TiO_2 is large (~100), the binding energy of the pair is small [8]. Once the Ti^{3+} is freed from the impurity center, it contributes an electron to the conduction band. Thus Nb^{5+}-Ti^{3+} bound pair can be considered as a donor level.

Also during sintering, most commonly TiO_2 is reduced, creating a non-stoichiometric excess of Ti. This produces either oxygen vacancies or titanium interstitials. Since the rutile structure is quite loosely packed, the presence of Ti interstitials are possible. A Ti interstitial have four extra electrons. Among these only one electron is bound to the interstitial, the remaining three are bound to nearest neighbor Ti sites. Thus a Ti interstitial acts as a quadruple donor. Hence both Nb doping and reduction of TiO_2 increase the conductivity of TiO_2 grains.

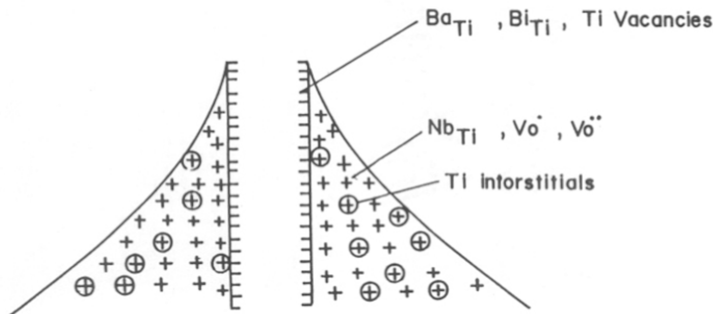

Figure 3.28 Defect model for TiO_2 varistor

The second group of dopants are the acceptor dopants. Sr^{2+} and Bi^{3+} with lesser valence than Ti^{4+} are the acceptor dopants in this case. These acceptor dopants are selected according to their ionic size. Both Sr^{2+} and Bi^{3+} (0.96 A^{o}) have ionic size larger than Ti^{4+} (0.61A^{o})[9]. These dopants with larger ionic radii and lower valence prefer to segregate at the grain boundary in order to relieve the large elastic energy caused by ionic radii

mismatch. These segregated ions act as acceptors which locally compensate the donors. This results in increase in grain boundary resistivity.

$$SrO \leftrightarrow Sr_{Ti}^{//} + V_o^{\bullet\bullet} + O_o^{x} \qquad \text{----------(3.7)}$$

These oxygen vacancies ($V_o^{\bullet\bullet}$) are very important factor which controls the sintering kinetics. It is well known that oxygen vacancies control grain growth. Hence Sr acts as a grain growth enhancer in this case. At the same time, according to Equation (3.5), addition of Nb leads to increase in oxygen partial pressure which decrease the concentration of oxygen vacancies and inhibits grain growth. Hence Nb acts both as a donor an a grain growth inhibitor. Sr acts as an acceptor and a grain growth enhancer.

Now, it is clear that defects, both intrinsic and extrinsic, exist in TiO_2 varistor system. Hence the formation of energy barrier can be explained by a defect model as explained by Gupta *et al*[10] in the case of ZnO voltage sensors.

Figure **3.28** represents the defect model diagram for Schottkey barrier at the grain boundary. The depletion layer comprising the barrier consists of positively charged ions. These include the pentavalent substitutional ions $[Nb_{Ti}^{\bullet}]$ and the native oxygen vacancies $V_o^{\bullet}$ and $V_o^{\bullet\bullet}$ and also the very small amount of titanium interstitials. These positively charged ions extend from both sides of the grain boundary into the adjacent grains and are compensated by a layer of negatively charged ions at the acceptor ions ($Ba_{Ti}^{//}$ and $Bi_{Ti}^{/}$) and the native Ti vacancies. Electrical neutrality in the bulk of the crystal is maintained at equilibrium with the negative charges on the grain boundary being balanced by an equal and opposite space charge penetrating some distance into the TiO_2 grains. This negative charge at the interface and corresponding +ive charged layer in the grains create an effective energy barrier to the conduction of electrons across the grain boundary. Both the intrinsic and the impurity controlled defects can produce an effective energy barrier at the grain boundary (Double Schottkey barriers). This in turn will lead to non-linear behaviour[12].

During sintering process, the larger acceptor ions, Sr^{2+} and Bi^{3+}, segregate at the grain boundary. It has already been proved experimentally[13] that there is no effect on the current-voltage characteristics by extending the sintering time above 2hrs, since the

segregation of strontium have reached a saturation level and the quantity of strontium segregation approaches steady values.

Above 1300°C, the loss of Bi, which acts as a volatilizing liquid phase, is more. Hence a decrease in density is observed. This will decrease the amount of acceptor dopants at the grain boundary. The decrease in the negative space charge at the grain boundary interface will lead to reduction of barrier height and hence reduction in non-linear behaviour. Hence 1300°C is the optimum sintering temperature at which the correct amount of Ba and Bi segregation occurs, leading to an excellent grain boundary layer and thereby better non-linear behaviour.

The change in the energy barrier or the formation of energy barriers at different temperatures were examined further by the impedance analysis. The activation energy of the grain boundary region found out from the impedance analysis agree to the fact that 1300°C is the sintering temperature to get optimum non-linear characteristics. Greater the activation energy means more effective the grain boundary barrier layer. This is in agreement with other works reported in the literature[13-15]. The 1300°C sintered sample gave the maximum activation energy. At 1350°C, the activation energy was 0.201eV which is the energy required for a charge to jump within the TiO_2 lattice [17], and hence no efficient boundary barrier exists at 1350°C. This can only be due to the loss of Bi at higher sintering temperatures.

The impedance analysis also gives the evidence of an insulating grain boundary phase which gives rise to a capacitor like structure. This capacitor like structure gives high impedance to conduction at low frequencies and its resistance becomes negligible at high frequencies. Hence the impedance analysis gives the evidence for a grain-grain boundary like structure existing in these TiO_2 ceramics.

The substitution of Sr^{2+} by Ca^{2+} or Ba^{2+} doesnot give any large degree of change in the non-linearity coefficients. Eventhough there is a difference in the breakdown voltage, the difference cannot be related to any particular property of the dopant, like ionic size. The difference may be attributed to the nonuniform distribution of dopants which is quite reasonable considering the reproducibility problems in ceramic route of synthesis. Ionic size of the dopant ions Ca, Sr and Ba[9] are considerably larger than Ti^{4+} that they prefer to

occupy the grain boundary position and acts as acceptor centers. Hence among Sr, Ba and Ca dopants, anyone can be chosen since it doesn't make much of an influence on the non-linear coefficient of the varistor.

The breakdown voltage per grain boundary was calculated in the case of Sr doped TiO_2 varistors after measuring the grain size. For the optimum sample, that sintered at 1300°C, the E_{gb} was found to be 0.32volt . For other temperatures it is slightly different. This value of 0.3volt/grain boundary is considerably smaller than that observed in the case of ZnO varistors (~3volts/gb)[18,19]. The difference in the grain boundary breakdown voltage at various sintering temperature can be attributed to the presence of some ohmic grain boundaries. i.e. non-uniform distribution of insulating grain boundary layers. This behaviour is similar to that observed in the case of ZnO varistors[20].

The Mg^{2+} doped sample doesnot show any non-linear current-voltage behaviour. Mg^{2+} ionic size (0.72A°) is relatively similar to Ti^{4+} (0.61A°) and Mg^{2+} can go into the TiO_2 lattice and thereby neutralizes the enhanced conduction behaviour brought about by Nb^{5+} doping. Mg^{2+} ions in the lattice sites act as an acceptor and increase the resistivity of the TiO_2 grains and thereby the non-linear behaviour is destroyed.

The chemically prepared composition of Sr doped TiO_2 varistor gave no improvement in the non-linear nature eventhough it gave similar non-linear coefficient values. The density of the sintered samples were found to be very low. The density of the sample is very important in determining the varistor characteristics since a close grain to grain contact is necessary to form the necessary energy barrier. This has been found true in both ZnO and SiC varistors[21,22]. Large amount of Bi, which acts as a good densifying agent is this system, is lost during two stages of thermal treatment. Bi_2O_3 have a low melting point of 825°C which is considerably lower than the sintering temperature of 1200°C and above. Hence during calcining itself, Bi will start migrating to the surface of the sample[23] and as the temperature goes higher, a part of it vaporizes causing loss of Bi from the sample affecting the required ratio.

3.13 Conclusions

TiO_2 based ceramics with Sr, Nb and Bi dopants sintered at 1300°C gave excellent non-linear current-voltage characteristics with a low breakdown voltage. A relatively good non-linear coefficient of α=8.4 and a very low breakdown voltage of 0.31volts/grain boundary is attained in this sample[24]. This low breakdown voltage of the varistor will be useful for the material to be used in microelectronic devices.

Other dopants such as Ca^{2+} and Ba^{2+} doesnot make much changes in the non-linear behaviour of the TiO_2 varistor. Eventhough it exhibits different breakdown voltages, there is no direct relation for these breakdown voltage value with the ionic size of these dopants. The difference exhibited by the Sr^{2+}, Ca^{2+} or Ba^{2+} doped TiO_2 varistors is a direct consequence of the inhomogeneous distribution of the insulating grain boundary layers.

The chemical synthesis of the TiO_2 varistors doesnot show any improvement in the non-linear behaviour due to the low density of the sintered samples. If a suitable method is developed to synthesis homogeneously doped TiO_2 varistors by the chemical method which have good density (~95%), improved non-linear behaviour is expected.

The impedance analysis is a good technique to understand the grain-grain boundary behaviour. Arrhenius plots of the grain boundary resistivity give the activation energy which gives an idea about the formation of the effective energy barrier. More detailed analysis by impedance spectroscopy is needed to understand the TiO_2 system completely. Also, degradation phenomenon in this system have to be studied. A detailed study on the degradation will help in determining how much these TiO_2 varistors are commercially viable in future.

References

1. R.G.Breckenbridge and W.R.Hosler., *Phys.Rev.*, **91**, 793(1953).
2. P.Kofstad., *J.Less-Common.Mat.*, **13**, 635(1967).
3. M.F.Yan and W.W.Rhodes., *Appl.Phys.Lett.*, **40**, 536(1982).
4. J.Pennewiss and B.Hoffmann., *Mater.Lett.*, **9**, 219(1990).
5. J.M.Wu and C.H.Lai., *Mater.Lett.*, **15**, 35(1992).
6. S.L.Yang and J.M.Wu., *J.Mater.Res.*, **10**, 345(1995).
7. R.W.Baluffi., *Mater.Res.Soc.Bull.*, **XVI**, 23(1991).
8. D.Atler., "Semiconducting ceramic compounds" in Physics of Electronic ceramics., **Part A,** 29, Ed.by L.L.Hench and D.B.Dove., Marcel Dekker, INC. NewYork (1971)
9. R.D.Shannon., *Acta.Cryst.*, **A32**, 751(1976).
10. T.K.Gupta and W.G.Carlson., *J.Mater.Sci.*, **20**, 3487(1985).
11. T.K.Gupta., *J.Amer.Ceram.Soc.,* **73**, 1817(1990).
12. S.L.Yang and J.M.Wu., *J.Mater.Sci.Lett.*, **14**, 748(1995).
13. S.L.Yang and J.M.Wu., *J.Amer.Ceram.Soc.*, **76**, 145(1993).

14 S.A.Pianaro, E.C.Pereira, L.O.S.Bulhoes, E.Longo and J.A.Varela., *J.Mater.Sci.*, **30**, 133(1995).

15. S.L.Yang and J.M.Wu., *J.Amer.Ceram.Soc.*, **78**, 2203(1995).
16. J.M.Wu and C.J.Chen., *J.Mater.Sci.*, 23, 4157(1988).

17 G.D.Mahan, L.M.Levinson and H.R.Philipp., *J.Appl.Phys.*, **50**, 2799(1979).

18. E.Olsson and G.L.Dunlop., *J.Appl.Phys.*, **66**, 3666(1989).

20 M.Bartkowiak, G.D.Mahan, F.A.Modine and M.A.Alim., *J.Appl.Phys.*, **79**, 273(1996).

21. M.C.S.Nobrega and W.A.Mannheimer., *J.Amer.Ceram.Soc.*, **79**, 1504 (1996).
22. M.Ura., "Ceramic Substrates"., p243 in *Fine Ceramics.*, Ed.by S.Saito. Elsevier, NY, 1988.
23. S.R.Sainkar, S.Badrinarayanan, A.P.B.Sinha and S.K.Date., *Appl.Phys.Lett.*, **39**, 65(1981).
24. P.N.Santhosh, D.K.Kharat and S.K.Date., *Mater.Lett.*, **28**, 37(1996).

CHAPTER 4

TIN DIOXIDE VARISTORS

4.1 Introduction

Tin dioxide exhibits a structure nearly identical with the rutile structure of titania[1]. The experimental data related to the transport and optical properties has proved it to be an n-type wide band gap semiconductor. The band gap of SnO_2 is ~3.5 eV [2,3]. These aspects of tin dioxide are suitable for it to be taken seriously as the base material of a voltage sensor. The rutile structure of SnO_2 provides an open lattice structure which can accommodate the dopants, similar to the wurtzite structure of ZnO and rutile structure of TiO_2.

Nb_2O_5 is added in very small concentration (0.05 mol%) as a dopant. Nb^{5+} have an ionic radii similar to Sn^{4+} and hence it is expected to occupy the lattice position. Hence, similar to the case of TiO_2, Nb_2O_5 is added to increase the conductivity of SnO_2 grains. At the same time, there will remain the perfect local environment of oxygen octahedra surrounding Sn^{4+} ions.

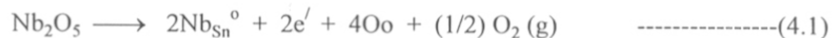

$$Nb_2O_5 \longrightarrow 2Nb_{Sn}^{o} + 2e^{/} + 4O_o + (1/2)\,O_2\,(g) \qquad \text{----------------(4.1)}$$

This relation shows that the substitution of Sn^{4+} by Nb^{5+} will provide with an additional electron to the lattice and thereby increase the conductivity. Also, Nb doping inhibits the grain growth to a certain extent.

Tin dioxide doesnot densify during sintering. This is due to the high vapor pressure of SnO_2 at high temperatures. Thus, the evaporation-condensation mechanism controls the sintering of tin dioxide[4], according to the relation

$$SnO_2 \longrightarrow SnO\,(g) + (1/2)\,O_2 \qquad \text{------------------(4.2)}$$

According to literature data[5] transition metal oxides can be used as densifying agents. In this case, CoO was taken as the densifying agent. A very small percentage of CoO(1 mol%) was added to SnO_2 as the densifying agent. According to the following reaction

$$CoO \longrightarrow Co_{Sn}^{//} + V_O^{\bullet\bullet} + O_o \qquad \text{------------------(4.3)}$$

the substitution of Sn atoms by Co leads to the formation of oxygen vacancies and these vacancies help in the process of densification of this SnO_2 ceramic. This conclusion is drawn from the known theory and experimental literature available related to doped SnO_2.

Since the ionic radii of Al^{3+} is comparable to the ionic radii of Sn^{4+}, the probability of Al^{3+} substituting Sn^{4+} is large. Al_2O_3 added to the SnO_2 matrix also acts as a densifying agent, according to the reaction

$$Al_2O_3 \longrightarrow 2Al_{Sn}^{/} + V_O^{\bullet\bullet} + 2O_o + (1/2)O_2(g) \qquad \text{-------------------(4.4)}$$

Doping of SnO_2 with Al_2O_3 has resulted in a more homogeneous microstructure.

In our experiments, SnO_2, CoO, Nb_2O_5 and Al_2O_3 were taken in the molar ratio 98.9:1:0.05:0.05 in their powder form and synthesized in the conventional ceramic process described in chapter.**2**. These samples were referred to as SCNA samples The sintered samples were then analyzed and the experimental results are given below..

4.2 Current-voltage (I-V) characteristics

The current-voltage characteristics of the SnO_2 samples were measured with the system described in section **2.4**. The SnO_2 samples were sintered at different temperatures 1200°C, 1230°C, 1250°C, 1300°C and 1350°C for 1 hr duration. These temperatures were chosen after a lot of preliminary probing experiments on sintering at various temperature/time intervals were analyzed. The I-V characteristics of these samples are given in figure **4.1** on a log-log scale. Typical thickness of the sample was 0.7mm and the electrode area on both sides of the compact was $0.4cm^2$. The performance parameters of these samples are given in Table **4.1**.

The sample sintered at 1200°C didnot show any non-linear behaviour within the limits of our experimental setup and from the figure it is clear that they have high leakage currents. The sample sintered at 1230°C do show an improvement in non-linear behaviour with a non-linear coefficient $\propto \approx 17$ and a breakdown voltage E_{1mA} = 1230 volts/mm. As the sintering temperature is further increased to 1250°C, the $\propto$ value also increases to 24. At the same time, the breakdown voltage is decreased. i.e., $E_{1mA} \approx 700$ volts/mm.

Further increase in sintering temperature to 1300°C reduces the non-linearity of this varistor to $\propto \approx 11$ and the breakdown voltage at this temperature is 380 volts/mm. Increase in the sintering temperature to 1350°C further reduces the non-linear coefficient and the breakdown voltage, i.e., $\propto = 10$ and $E_{1mA} = 355$volts/mm. The I-V characteristics pointed out that 1250°C is the optimum temperature of sintering.

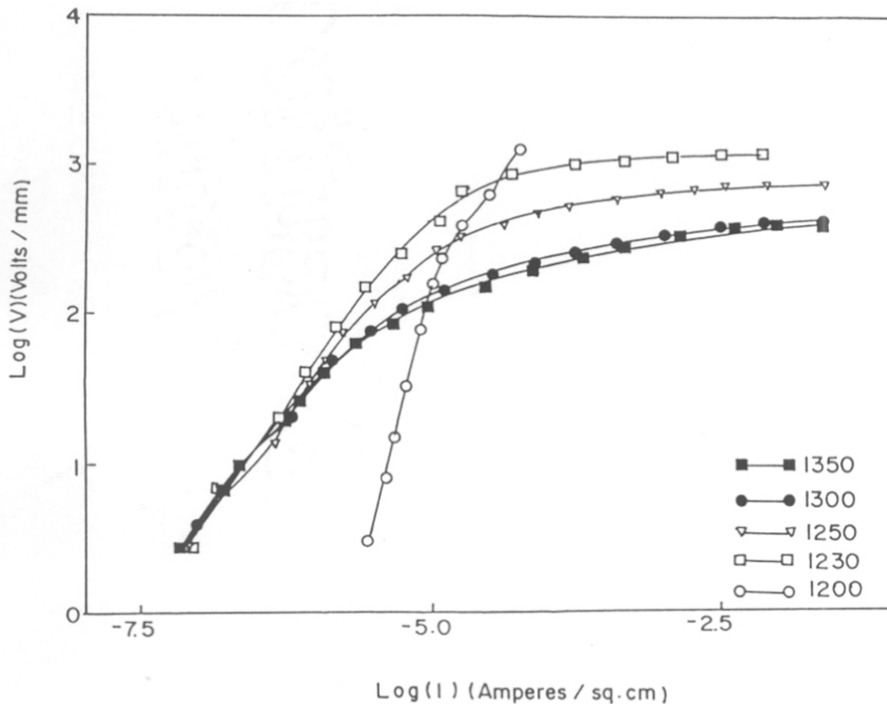

Figure 4.1 Current-voltage (I-V) characteristics of SCNA samples.

Table 4.1 Performance parameters of SCNA samples

Sintering temperature (°C)	Non-linear coefficient ($\propto$)	Breakdown voltage (E_{1mA}) volts/mm
1200	--	--
1230	17	1230
1250	24	700
1300	11	380
1350	10	355

The non-linear coefficient of all the samples were estimated in the same range of currents. In this case the current range for the calculation of ∝ is 1mA to 10mA and the breakdown voltage was taken as the voltage corresponding to 1mA.

In the case of samples sintered at 1200°C the prebreakdown current or the leakage current is large (>10^{-6} amperes/cm^2). All the other samples , i.e., sample sintered at 1230°C, 1250°C, 1300°C and 1350°C have lower pre-breakdown current (~10^{-8} amperes/cm^2). The linear low-current region represents the grain boundary characteristics. A well defined grain boundary or energy barrier will lead to better non-linear characteristics. The pre-breakdown characteristics show that for the sample sintered at 1200°C, the grain boundary resistance is considerably smaller than the corresponding resistances of the samples sintered at higher temperatures. Hence it is concluded that a sintering temperature of 1230°C and above is needed for the formation of highly resistive grain boundary regions and thereby an effective energy barrier. Also the samples sintered at 1250°C gave the maximum ∝ value of 24. Sintering above and below this temperature yielded inferior non-linear current-voltage characteristics. The reason for this optimum properties for our dopant concentration may be related to the efficiency of the grain boundary region. Figure **4.2** shows the variation of breakdown voltage and non-linear coefficient with the sintering temperature.

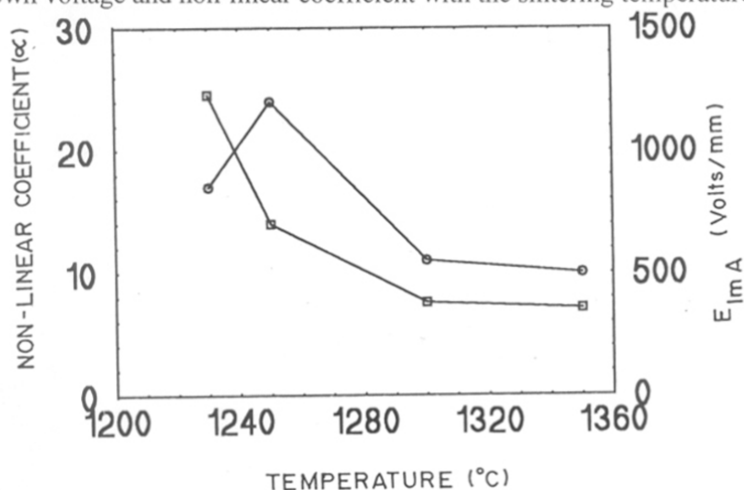

Figure 4.2 Plot of E_{1mA} and ∝ vs sintering temperatures for the SCNA sample.

The breakdown voltage decreased with increasing sintering temperature. This is understandable since the grain size increases with increasing sintering temperature. As the grain size increases, the number of grains and grain boundaries within the unit thickness of the sample decrease. Further analysis of the SCNA samples were done by analyzing the density, X-ray diffraction patterns and Scanning electron micrographs to find the microstructural behaviour. These results are discussed in the following sections.

4.3 Density

For all the sintered samples, the density was found by the method mentioned in section**2.3**. The variation in sample density against the sintering temperature is given in figure **4.3**. There is a clear increase in sintered density when the sintering temperature is increased. The density at 1200°C is 5.5 gm/cc. At 1250°C it is 5.75 gm/cc, at 1300°C it is 6.06 gm/cc and at 1350°C it is 6.15 gm/cc. For a good varistor behaviour, a good grain to grain contact is necessary. Hence the addition of CoO to SnO_2 is necessary to increase the density of the material and thereby leading to a better grain-grain contacts.

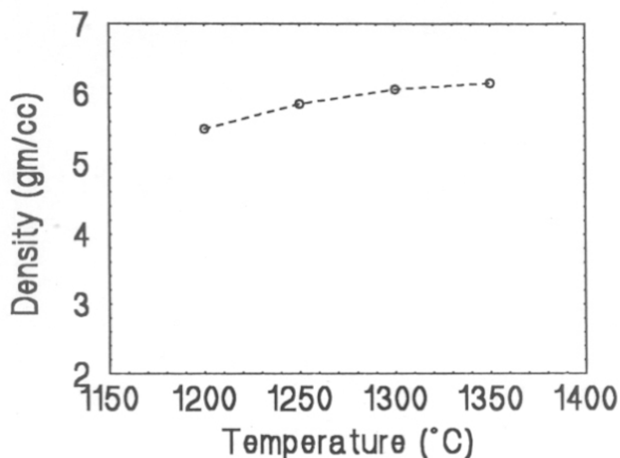

Figure 4.3 Density vs sintering temperature(°C) of SCNA samples.

Reports are available [6] where the density was further increased up to 95% by sintering at still high temperatures of ~1450°C. But since the non-linear behaviour of SnO_2 ceramics

diminishes at temperatures above 1300°C, the sintering temperature was restricted up to 1350°C and no further measurements were carried out during the course of this work.

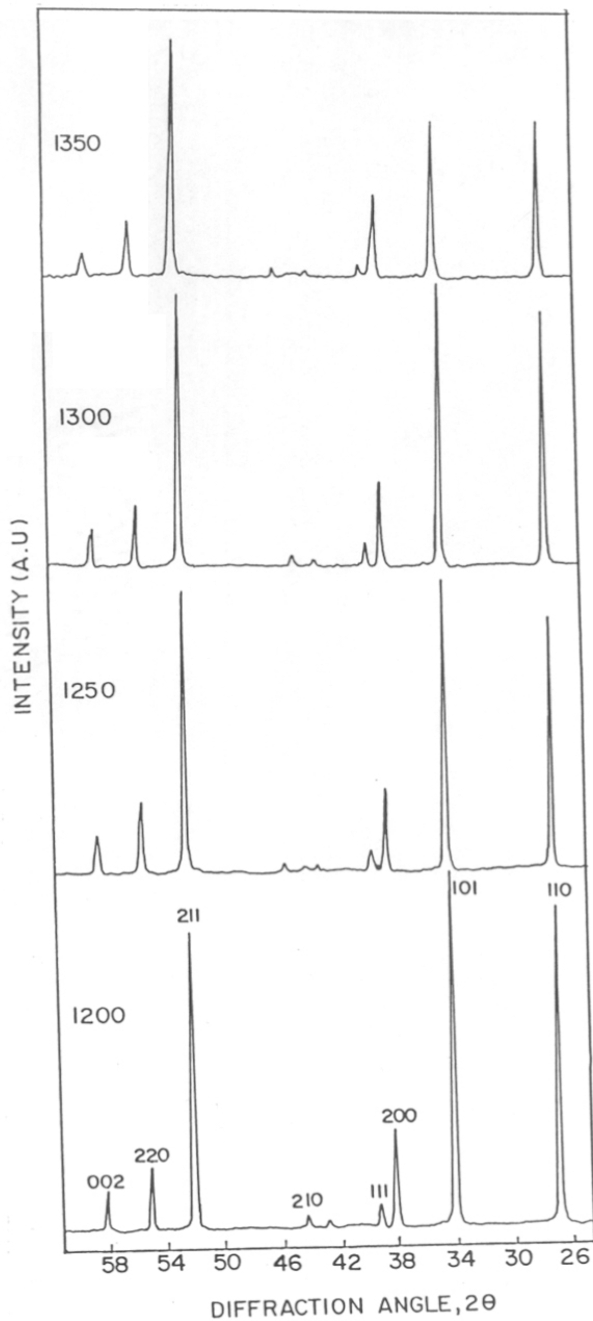

Figure4.4 X-ray diffraction pattern of SCNA samples sintered at different temperatures(°C)

4.4 X-Ray diffraction analysis.

The X-ray diffraction patterns of SCNA samples sintered at various temperatures are given in figure **4.4**. All the samples, i.e. those sintered at 1200°C, 1250°C, 1300°C and 1350°C show the diffraction peaks corresponding to SnO_2 rutile structure. The typical XRD peak positions, their relative intensity, hkl parameters are given in Table **4.2** and the rutile structure of SnO_2 is given in figure **4.5**.

Table 4.2 X-ray diffraction data of rutile SnO_2 from literature [8]

d values	2θ	I / I_1	h k l
3.351	26.578	100	1 1 0
2.644	33.875	81	1 0 1
2.369	37.949	25	2 0 0
2.309	38.975	6	1 1 1
2.120	42.611	2	2 1 0
1.765	51.751	65	2 1 1
1.675	54.757	18	2 2 0
1.593	57.834	8	0 0 2
1.498	61.889	14	3 1 0
1.439	64.727	18	1 1 2
1.415	65.963	16	3 0 1
1.215	78.688	12	3 2 1

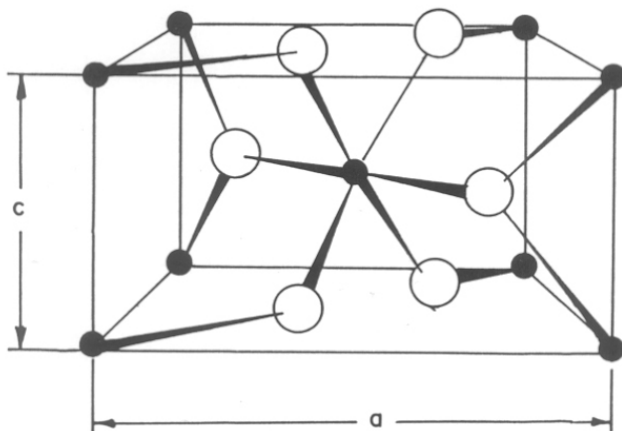

Figure 4.5 Crystal structure of SnO_2 (rutile). Large circles indicate oxygen atoms and small circles indicate tin atoms.

The XRD patterns of SCNA samples donot show any additional peaks corresponding to secondary phases which are expected to develop during the sintering process. Also the concentration of dopants is too small to form a secondary phase to be detected by XRD. In addition, the ionic sizes of the dopants, Al^{3+} (0.535) Nb^{5+}(0.65) and Co^{2+} (0.65), are smaller than Sn^{4+}(0.69)[7] and hence these ions occupy the lattice position. Since no liquid phase forming materials are added (like Bi), no separate phases are formed.

4.5 Scanning electron micrographs of fractured surface

The Scanning electron micrographs of all the SCNA samples were taken to understand the grain-grain boundary microstructure. The pellets were fractured and the fractured surface were analyzed using SEM after coating that surface with gold. The scanning electron micrographs of the SCNA samples sintered at 1200°C, 1250°C, 1300°C and 1350°C are given in figure **4.6**.

The grain sizes obtained for each sample are given in Table **4.3**. From the Table, it is seen that the grain size increases with increasing sintering temperature.

Table 4.3 Grain sizes of SCNA samples obtained from SEM

Sintering temp.	1200	1250	1300	1350
Grain size(μm)	~1	~3	~6	~7.5

For the SCNA sample sintered at 1200°C, the average grain size is ~1μm. As the sintering temperature is increased to 1250°C, a clear increase in grain size is seen. Average grain size at this temperature is ~3μm. A further increase in grain size is observed when the temperature is increased to 1300°C. The average grain size is 6μm at this temperature. At 1350°C, a further increase up to 7-8μm is seen. This increase of the grain size have a clear effect on the current-voltage characteristics of the varistor. The breakdown voltage decreases with increasing sintering temperature. Unlike the fractographs of TiO_2 varistors given in Chapter.**3**, the grains in this case have platelet like nature. A clear separation of individual grains is not observed and there are large number of voids resulting in lower density.

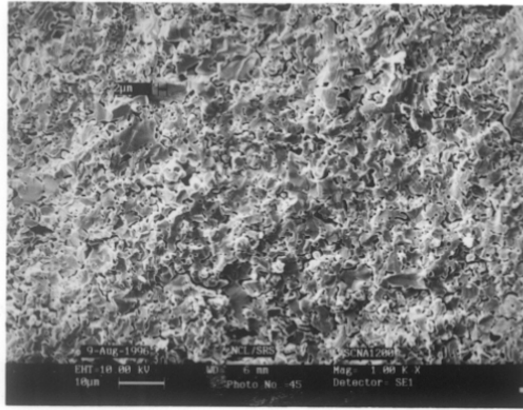

(a)

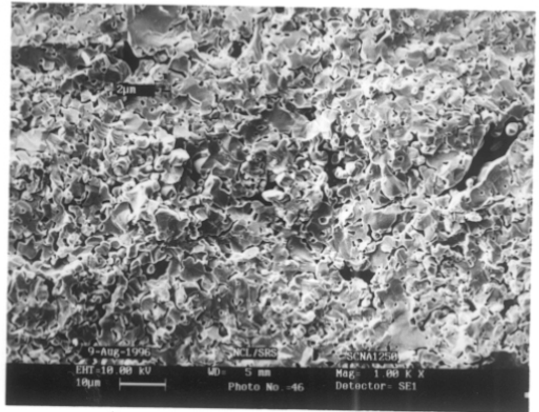

(b)

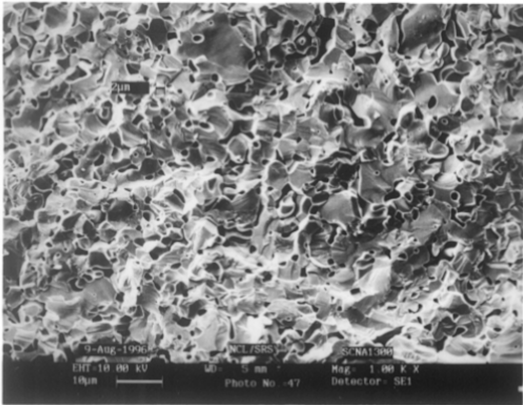

(c)

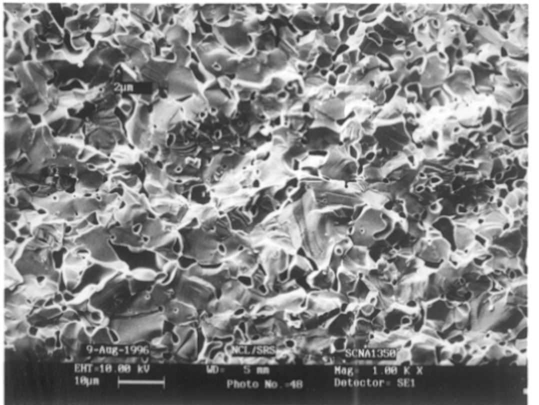

(d)

Figure4.6 Scanning electron micrographs of SCNA samples sintered at (a)1200°C (b)1250°C, (c)1300°C, and (d) 1350°C.

In typical ZnO and TiO_2 varistors, grain boundary phases are observed in the micrographs. But in this SnO_2 varistor, no clear grain boundary phases are seen. This may be due to the absence of low temperature melting dopants like Bi_2O_3 and the known effects of liquid phase sintering.

4.6 Impedance analysis

Impedance analysis of all the samples were done by the method described in chapter.**2**. An a.c voltage of 100mV was applied in all the measurements. A frequency range of 10Hz to 32MHz was employed for the measurements.

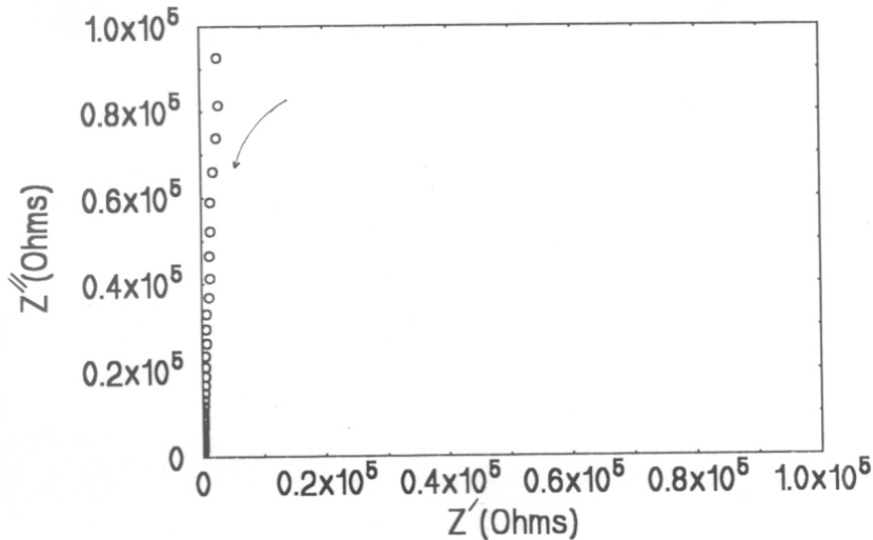

Figure 4.7a Impedance plot of SCNA1250 sample measured at room temperature.

Figure **4.7a** represents the Z' vs Z'' curves (Z' - the real component, Z'' -the imaginary component) of the impedance plots of the SCNA sample sintered at 1250°C. This is the sample which gave the best non-linear characteristics. Figure **4.7a** is the Z' vs Z'' plot of the SCNA sample taken at room temperature. The increase in frequency is from right to left as shown in figure. This curve shows only a part of a very large semicircle. This happens because of a very large resistance of the sample (> 10^8 ohms). Major contribution to this resistance is due to the grain boundary resistance. Also, there is a lot of disturbance in the measured data at the low frequencies and hence a clear evaluation of the data in the low frequency region at this measuring temperature is not possible. The contribution to these plots from the grain boundary phase is so much larger than the minor contribution from the grains and hence the grain contribution to the total impedance cannot be separated out.

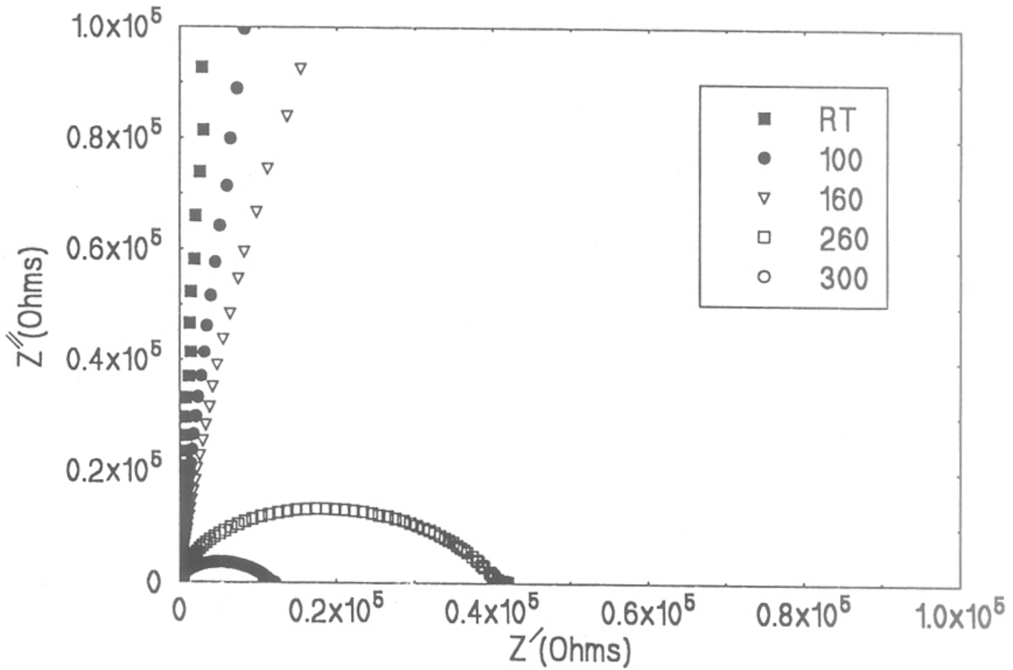

Figure 4.7b Impedance plots ($Z^{/}$ vs $Z^{//}$) of SCNA1250 sample measured at different temperatures.

Therefore, to have a better understanding of the individual contributions from grain and grain boundaries, high temperature data, RT to 300°C, was also recorded. Figure **4.7b** represents the $Z^{/}$ vs $Z^{//}$ pots of these SCNA samples measured at 100°C, 160°C, 260°C and 300°C . Since the material is a high resistance (insulating) material, it is seen that the grain boundary resistance decreased with increasing temperature. With increasing temperature, a clear semicircular pattern in the $Z^{/}$ vs $Z^{//}$ plots emerged.

The impedance data recorded at 300°C shows a well defined semicircle. The resonant point of these circles is ~10^3Hz and hence belongs to the contribution from the grain boundary. But even at this temperature, a semicircular like nature at the high frequency region representing the grain impedance is absent. This may be due to the considerable difference between the grain (~100Ω) and grain boundary impedance(~10^8Ω) values. Even at 300°C the grain boundary impedance is considerably larger than the grain impedance so that the

semicircle corresponding to grain at the high frequency region is submerged inside the semicircle corresponding to the grain boundary.

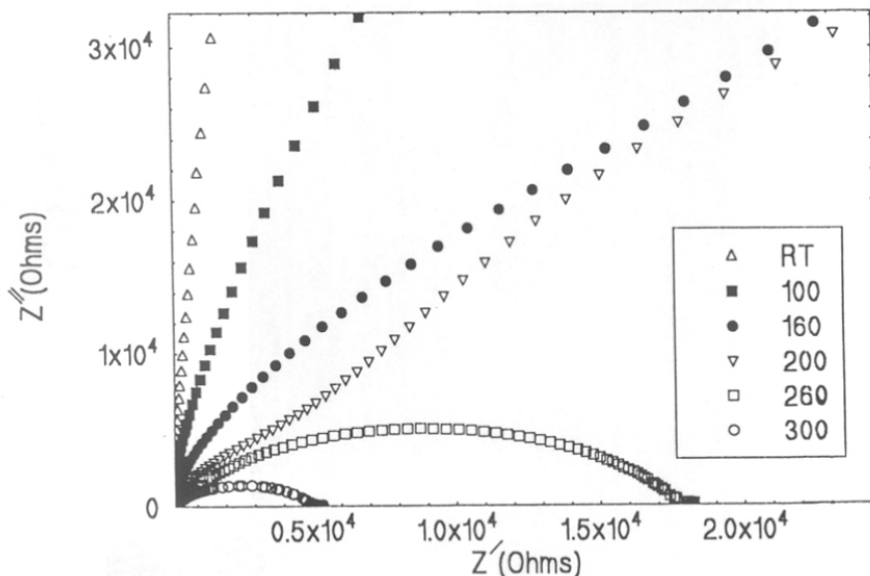

Figure 4.8 Impedance plots ($Z^{/}$ vs $Z^{//}$) of SCNA1300 sample measured at different temperatures

Similarly, the impedance plots of SCNA samples sintered at 1300°C and 1350°C were also recorded. The room temperature and other high temperature data of these samples are given in figures **4.8** and **4.9** respectively. In these figures, it is also seen that the grain boundary contribution to the total impedance is much greater than the grain contribution so that only one semicircle corresponding to the grain boundary is seen.

A semicircular fit of this curve gives the contribution from each part approximately. The low frequency intercept of the real part will represent the grain boundary contribution and the high frequency point will give the grain contribution at the measurement temperature. Since the semicircles are not well defined at room temperature and in some cases up to 150°C, the estimation of the different contributions to the total resistance of the sample is not possible with the above impedance plots. The semicircle corresponding to the

contribution from the grains are not seen even at the measuring temperature of 300°C. Hence, the analysis of the different contributions are done using the Bode plots.

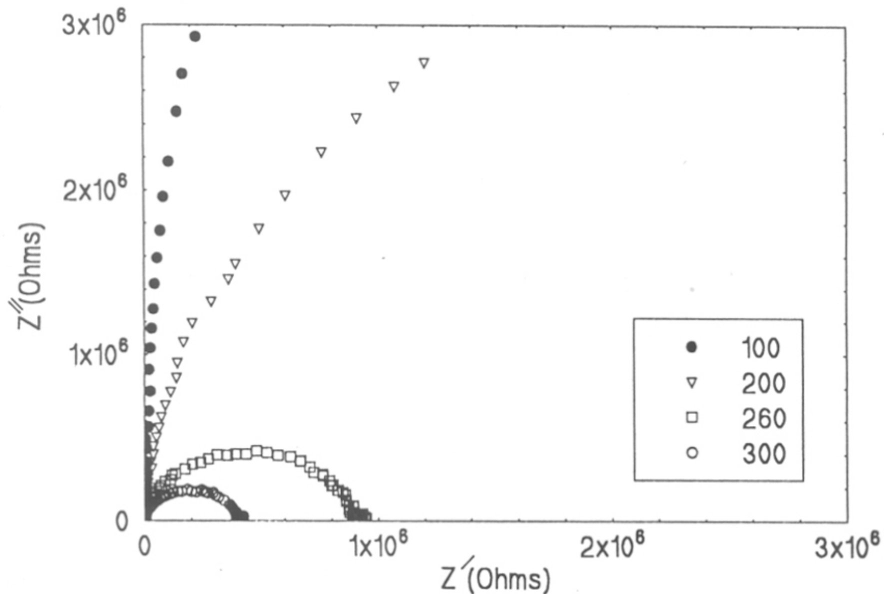

Figure4.9 Impedance plots (Z' vs Z'') of SCNA1350 sample measured at different temperatures

4.7 Bode plots

Bode plots are the curves plotted between the logarithm of modulus of resistivity ($\log|\rho|$) and the logarithm of the frequency(log(f)). These plots are made in the log-log scale since the measurements frequency is on a large range (10Hz to 32MHz) and the impedance also change over a large range ($10^9\Omega$.cm to 100Ω.cm).

Figures **4.10a** and **4.10b** are the Bode plots of the SCNA samples sintered at 1250°C and measured at different temperatures. (i.e. RT,100°C, 160°C, 200°C, 260°C and 300°C). Figure **4.10a** is the Bode plot for the SCNA sample measured at room temperature. Since the room temperature measured sample shows a lot of fluctuating points, it is difficult to

get a well defined value of the grain boundary resistivity from this curve. This data was not used further in the calculation of activation energy and its analysis.

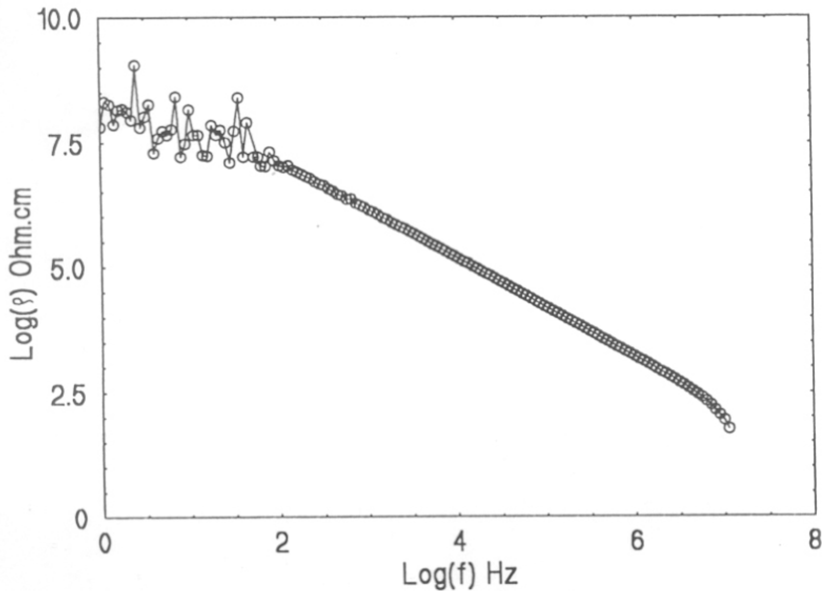

Figures 4.10a Bode plots for resistivity vs frequency of SCNA1250 sample measured at room temperature.

To find the grain and grain boundary contribution from the Bode plots, the following relations were employed

$$\log_{f\to 0}|\rho| = \log_{f\to 0}|\rho_{gb} + \rho_g| = \log|\rho_{gb}| \qquad \text{------------------(4.5)}$$

since $\rho_{gb} >> \rho_g$

and

$$\log_{f\to\infty}|\rho| = \log|\rho_g| \qquad \text{-------------------(4.6)}$$

ie, the low frequency point of the Bode plot corresponds to the grain boundary part for the total impedance and the high frequency point will give the grain resistivity.

From the Bode plots it is seen that there is a drastic drop in the resistivity (from ~10^8 Ωcm) as the frequency changes from 10Hz to 10^6Hz (to ~10Ωcm). This is a clear indication that a grain boundary like structure exists which leads to a capacitor like behaviour. Hence it is confirmed that a semiconductor-insulator-semiconductor (S-I-S) structure exists in these SnO_2 ceramics and it is the reason for the high non-linear behaviour exhibit by these materials. This S-I-S structure is similar to two electrodes separated by a dielectric material. At low frequencies, there is practically no conduction across the electrodes of a capacitor and hence a high resistance behavior is exhibited at low frequencies. As the frequency increases, the capacitor begins to conduct and hence the decrease in resistivity is seen. Hence, these results from the Bode plots is an indication of the existence of the grain boundary and its effects as a dielectric capacitor.

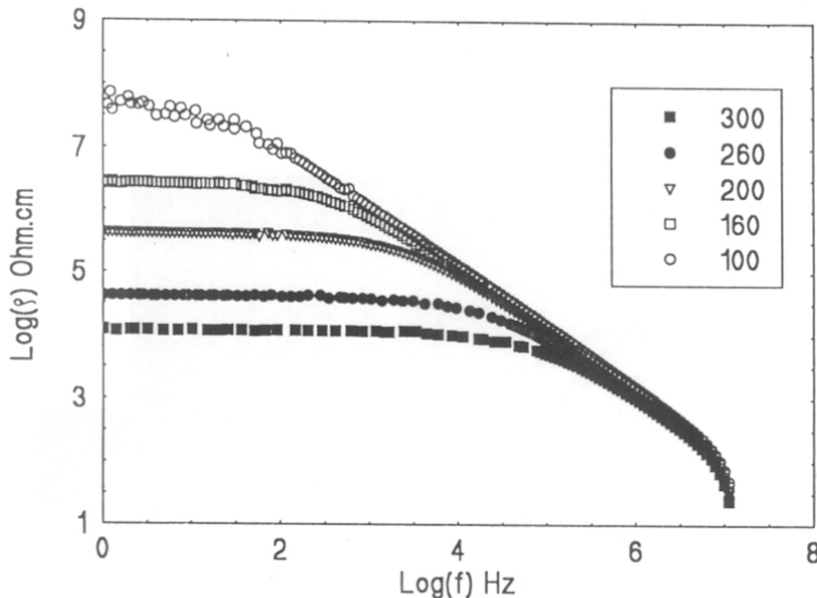

Figures 4.10b Bode plots for resistivity vs frequency of SCNA1250 sample measured at different temperatures.

The above results are further justified when the phase was plotted at different frequencies. The phase calculated at different frequencies for the above sample is shown in figure **4.11**.

The phase angle was 0° at low frequencies. But at the highest frequency point it has changed to -90°. This is also an indication of the capacitance like behaviour.

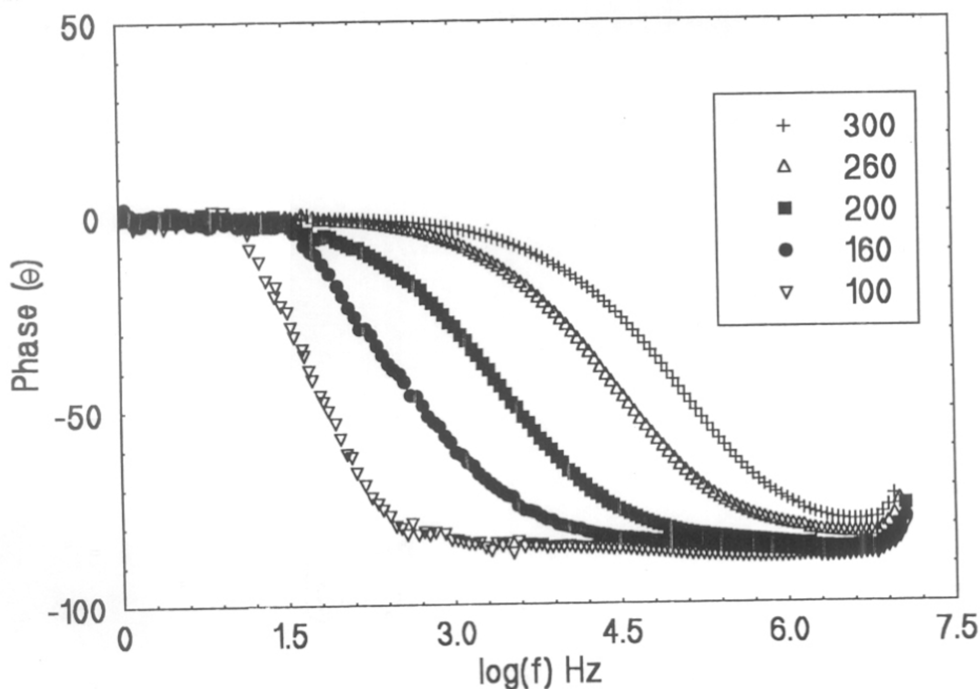

Figure4.11 Bode plots for Phase vs frequency of SCNA1250 sample measured at different temperatures.

Figures **4.12** and **4.13** represent the Bode plots of SCNA samples sintered at 1300°C and 1350°C respectively. The figures represent the measurement done at different temperatures from RT to 300°C. These curves also show drastic change in resistivity behaviour with respect to change in frequency indicating the presence of the grain-grain boundary structure in all these samples. The corresponding phase angle when plotted against the frequency gave the same behaviour as given in figure **4.11** justifying the conclusion of the formation of grain boundary.

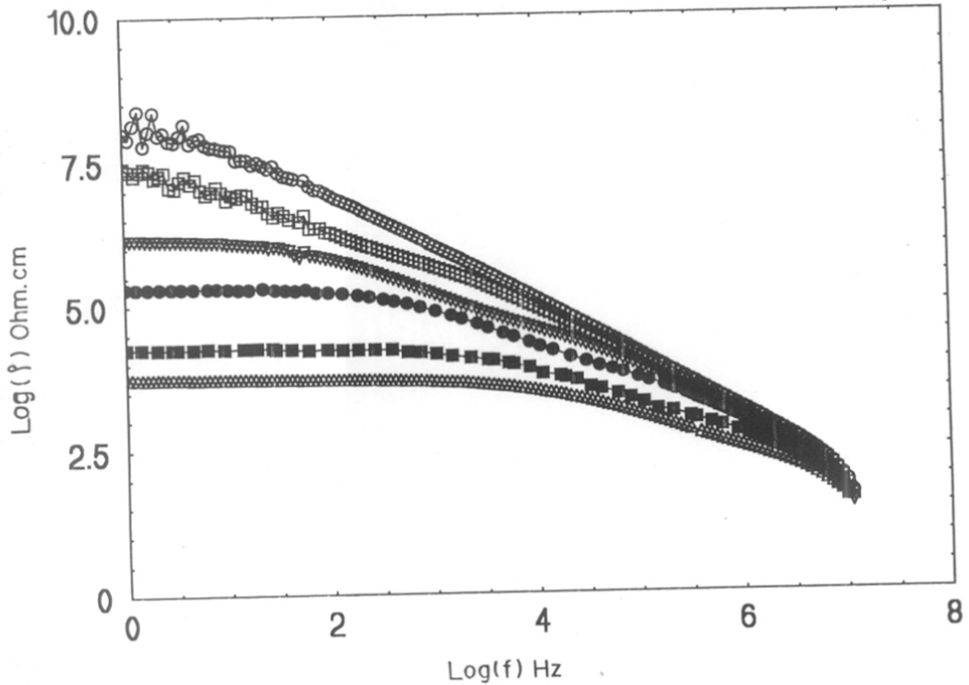

Figure4.12 Bode plots for resistivity vs frequency of SCNA1300 sample measured at different temperatures.

As far as the initial resistivity(i.e.,at low frequency) is concerned, all the samples have a similar value. This can be seen in the Table **4.4** which gives the grain and grain boundary resistivity values of the above the SCNA samples sintered at 1250°C, 1300°C and 1350°C. These parameters were found out from the Bode plots using the approximations given in equations (4.5) and (4.6). The corresponding grain boundary capacitances were found from the relation

$$C_{gb} = 1 / (\rho_{gb} .\omega) \quad \text{for } \tan(\theta) = 1 \qquad \text{--------------------(4.7)}$$

where $\omega = 2\Pi f$, f is the frequency at which θ becomes 45°.

From this analysis we can arrive at an equivalent circuit which consists of R_g in series with the parallel connection of R_{gb} and C_{gb}. Figure **4.14** represents the equivalent circuit of the

SnO_2 varistor. Hence the microstructure of the SnO_2 varistor is assumed to be a series combination of the impedance contributions from the grains and the grain boundaries.

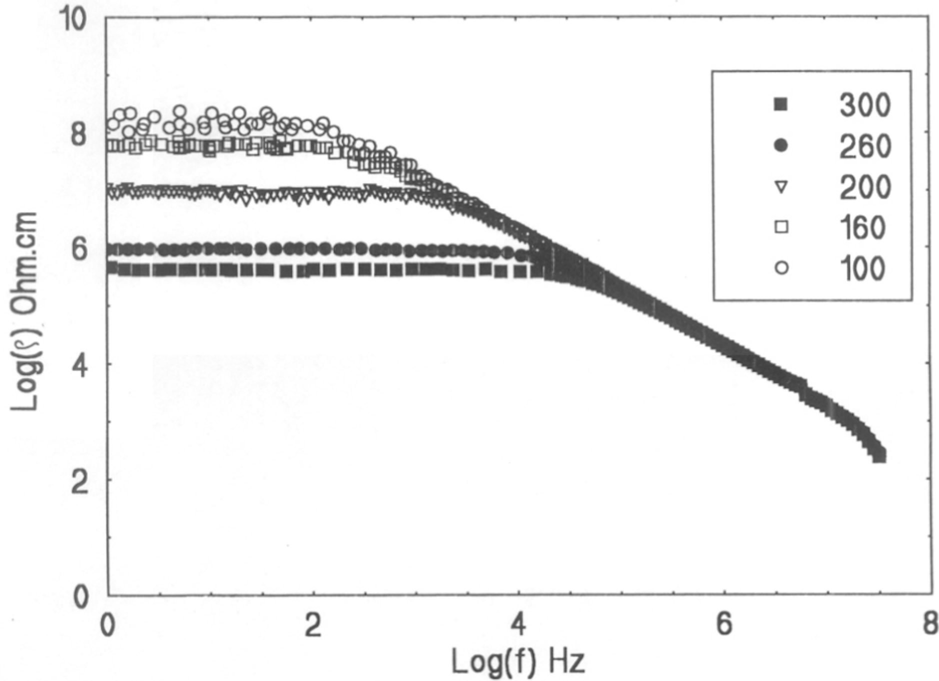

Figure 4.13 Bode plots for resistivity vs frequency of SCNA1350 samples measured at different temperatures

The resistivity at a particular measuring temperature is defined by the Arrhenius relation

$$\rho = \rho_o \exp[-E_A / K_B T] \qquad \text{--------------------(4.8)}$$

where ρ_o is the resistivity at 0°K, T is the temperature in Kelvin, K_B is the Boltzmann constant and E_A is the activation energy.

The activation energy of the grain boundary can be found out by plotting the logarithm of the grain boundary resistivity against (1 / T) and taking the slope of the curve.

Table 4.4 Grain resistivity, grain boundary resistivity and grain boundary capacitance's obtained from Bode plots

Sample	Measurement temperature (°C)	ρ_{gb} (Ohm.cm)	ρ_g (Ohm.cm)	C_{gb} (f.cm^{-2})
SCNA1250	100	5.623×10^7	48.97	6.41×10^{-11}
	160	2.860×10^6	41.70	1.29×10^{-10}
	200	4.365×10^5	36.30	1.26×10^{-10}
	260	4.161×10^4	28.18	1.23×10^{-10}
	300	1.148×10^4	23.96	1.21×10^{-10}
SCNA1300	100	2.13×10^7	39.81	6.05×10^{-11}
	160	1.44×10^6	33.88	3.57×10^{-10}
	200	1.99×10^5	30.91	4.10×10^{-10}
	260	1.83×10^4	38.01	4.28×10^{-10}
	300	5.25×10^3	46.17	6.48×10^{-10}
SCNA1350	100	9.12×10^7	281.84	--
	160	4.46×10^7	263.02	1.15×10^{-11}
	200	1×10^7	257.03	8.11×10^{-12}
	260	9.33×10^5	239.88	8.35×10^{-12}
	300	4.16×10^5	239.88	8.18×10^{-12}

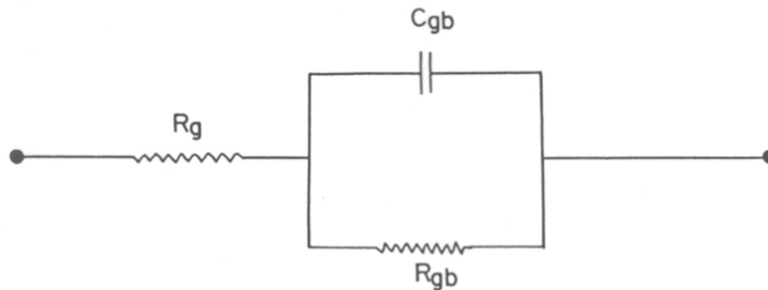

Figure 4.14 Equivalent circuit

Figure **4.15** represents the Arrhenius plots of the log(ρ) vs 1000 / T for the SCNA samples sintered at 1250°C, 1300°C and 1350°C. The data points corresponding to measurements below 100°C were avoided due to the large distribution/fluctuation in data points at these temperatures. The activation energy found out from the above Arrhenius plots are given in Table **4.5**.

Table 4.5 Activation energy of SCNA samples

Sintering temp. (°C)	1250	1300	1350
Activation energy (eV)	0.347	0.342	0.31

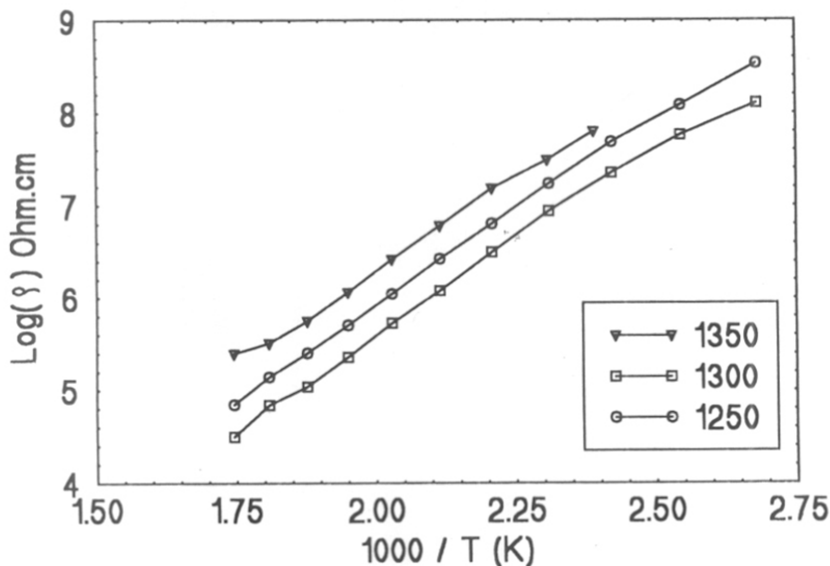

Figure 4.15 Arrhenius plots of resitivity vs temperature of SCNA samples.

The sample sintered at 1250°C gave a large activation energy of 0.347eV followed by 0.342eV for the sample sintered at 1300°C. The smallest activation energy of 0.31eV was found for the sample sintered at 1350°C. These values agree well with the corresponding values of ∝ obtained from the current-voltage characteristics.

4.8 Effect of other Co concentrations

CoO was added to the SnO_2 ceramics as a densifying agent. In the main composition described previously(SCNA), 1mol% of Co was added. To study the effect of the variation in Co concentration on the I-V characteristics, two more compositions were studied.

In the first composition, 2 mol% CoO was added as the densifying agent resulting in Sn:Co:Nb:Al = 97.9:2:0.05:0.05 sample. The concentration of Nb and Al were added at the same molar ratio as the SCNA sample and the purpose of these dopants remains the same.

This composition is termed S2CNA. In the second compositon, 0.05 mol% CoO was added as the densifying agent resulting in Sn:Co:Nb:Al = 99.4:0.5:0.05:0.05 sample. Here also the concentration of Nb and Al are similar to the other two compositions. This composition is abbreviated as S05CNA.

Both S2CNA and S05CNA samples were prepared by the conventional ceramic route described in Chapter.2. These samples were then characterized by I-V measurements, Density, SEM and XRD. These results are given below.

4.8.1 Current-voltage(I-V) characteristics

Figure **4.16** represents the current-voltage characteristics of the S05CNA samples sintered at 1200°C, 1230°C, 1250°C, 1300°C and 1350°C. The performance parameters obtained from these I-V data are given in Table **4.6**.

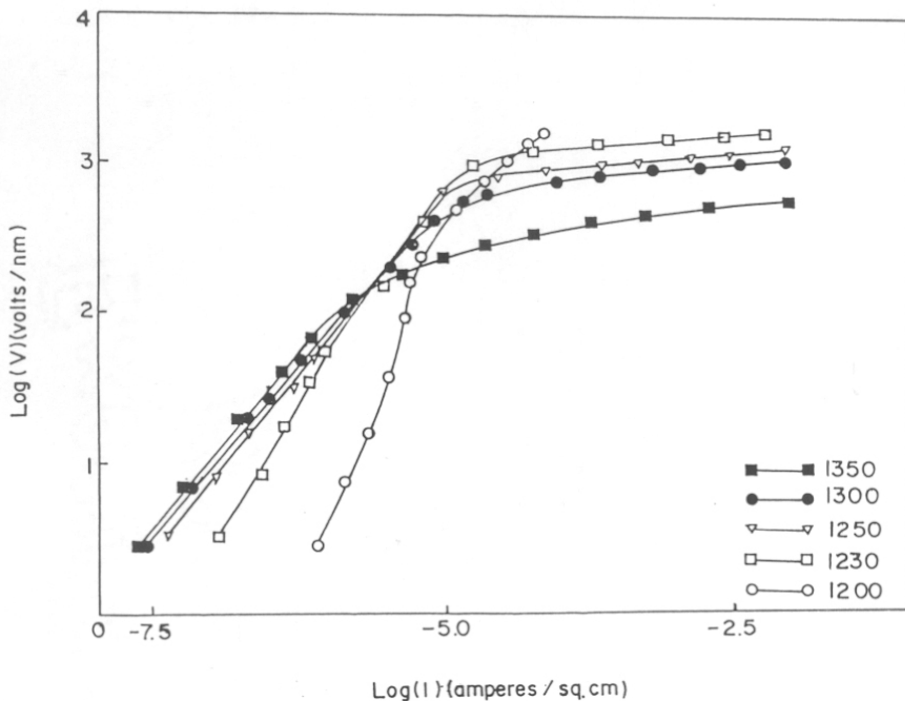

Figure4.16 Current-voltage characteristics of S05CNA samples.

Table4.6 Performance parameters of S05CNA samples

Sinetring temperature (°C)	Non-linear coefficient(∝)	Breakdown voltage (E_{1mA}) volts/mm
1200	--	--
1230	19	1480
1250	17	1070
1300	16	955
1350	15	510

The sample sintered at 1200°C doesnot show any non-linear behaviour similar to the behaviour observed in SCNA sample. The sample sintered at 1230°C exhibited the good non-linear behaviour with a non-linear coefficient ∝~19 and a breakdown voltage E_{1mA} = 1480Volts/mm. As the sintering temperature is further increased, both ∝ and E_{1mA} decrease as can be seen from the Table **4.6**. In this sample also, similar to SCNA samples, a sintering temperature more than 1230°C is needed to get good non-linear behaviour. This may be related to the formation of an efficient energy barrier above 1200°C.

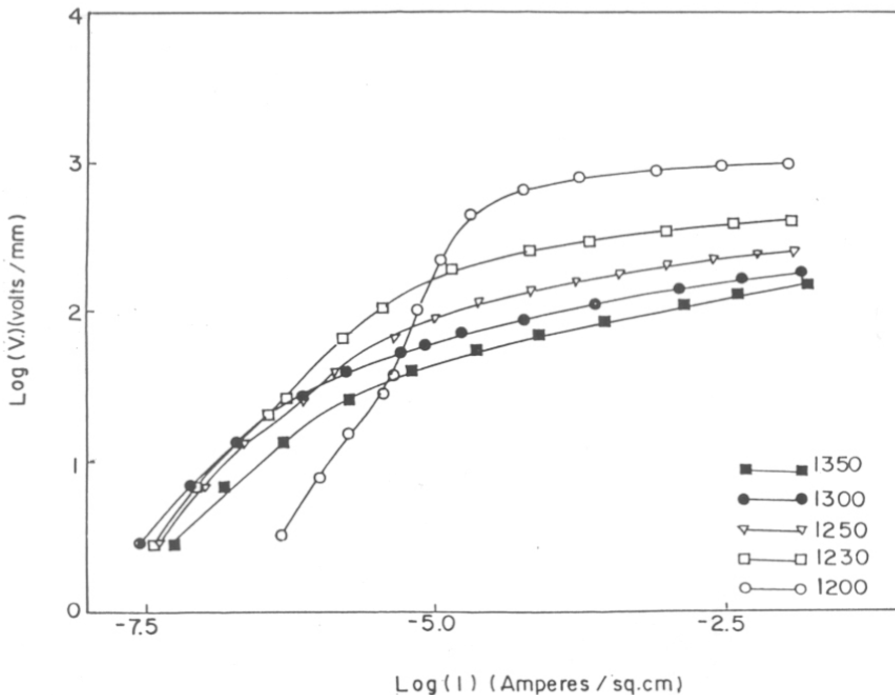

Figure 4.17 Current-voltage characteristics of S2CNA samples

Table 4.7 Performance parameters of S2CNA samples

Sinetring temperature (°C)	Non-linear coefficient(∝)	Breakdown voltage (E_{1mA}) volts/mm
1200	15.6	1020
1230	13.8	407
1250	10	240
1300	7.9	160
1350	7.2	126

Figure **4.17** represents the current-voltage characteristics of the S2CNA samples at 1200°C, 1230°C, 1250°C, 1300°C and 1350°C. The performance parameters obtained from this figure are given in Table **4.7**. From the table, it is clear that the sample sintered at 1200°C shows the best non-linear behaviour unlike the SCNA and S05CNA samples. At this temperature the performance parameters are $\propto \approx 15.6$ and E_{1mA} = 1020 Volts/mm. Further heating of the sample at higher temperature reduces both the ∝ and E_{1mA} values. This means that for S2CNA sample, the most effective energy barrier is created at 1200°C itself.

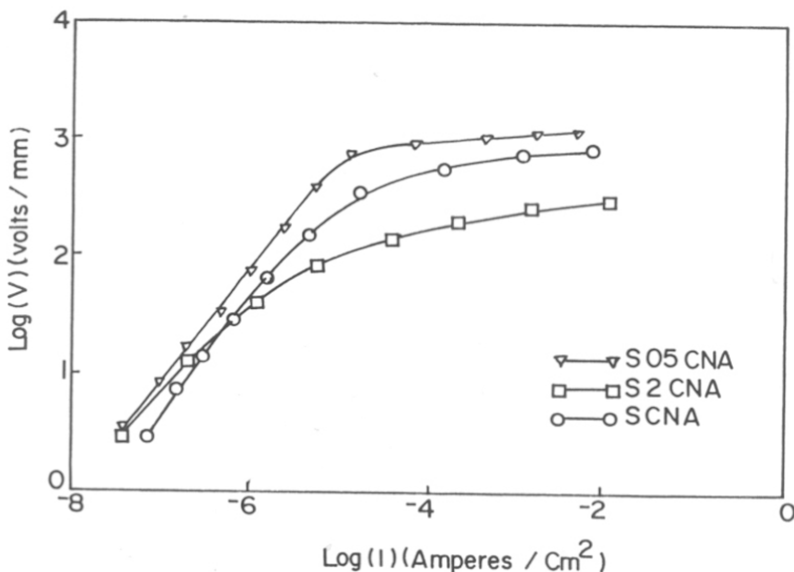

Figure 4.18 Current-voltage characteristics of S05CNA, SCNA and S2CNA samples sintered at 1250°C.

The most important aspect of S2CNA sample is that the breakdown voltage is reduced drastically compared to SCNA and S05CNA samples. This can be seen from the figure **4.18** which plots the I-V data for S05CNA, SCNA and S2CNA samples, all sintered at 1250°C. This may be related to the grain-grain boundary distribution and other microstructural aspects.

4.8.2 Density

Figure **4.19** represents the variation in sintered density as a function of temperature for the S05CNA and S2CNA..

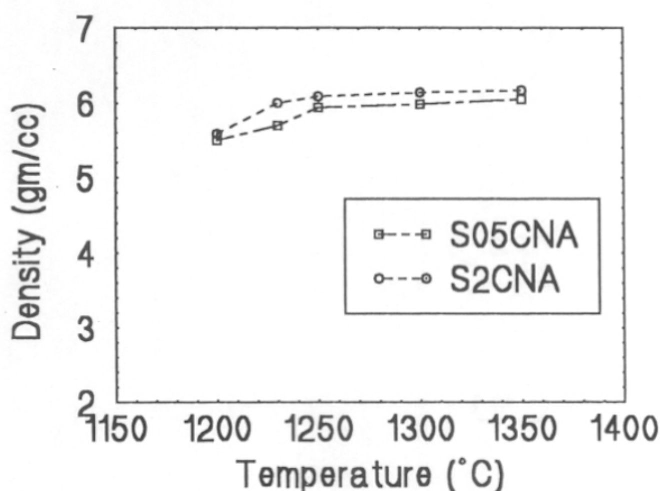

Figure 4.19 Measured density vs temperature of S05CNA and S2CNA samples.

Similar to the behaviour observed in SCNA sample, the density of the samples increases with increasing temperature The sample S05CNA have a maximum density of 6.05gm/cc at 1350°C whereas S2CNA sample have a maximum density of 6.17gm/cc at 1350°C. Comparing with the density values obtained in SCNA samples, the increase in Co concentration resulted in the increase the density in S2CNA samples.

4.8.3 X-ray diffraction for phase analysis

Figure **4.20** shows the X-ray diffraction pattern of S2CNA and S05CNA samples sintered at 1250°C. These are chosen as representative samples, since all the X-ray diffraction patterns show only the characteristic peaks corresponding to SnO_2 rutile structure. No peaks

corresponding to any other secondary phases are seen. This is also similar to the pattern observed in the case of SCNA samples. The relative intensity of the peaks differ since the XRD patterns were recorded on pellets where the orientation of the planes are likely to occur. The structural parameters of the S05CNA, SCNA and S2CNA samples are identical. This is understandable since the dopants added are of similar ionic sizes to Sn^{4+} ions and their concentrations are very small.

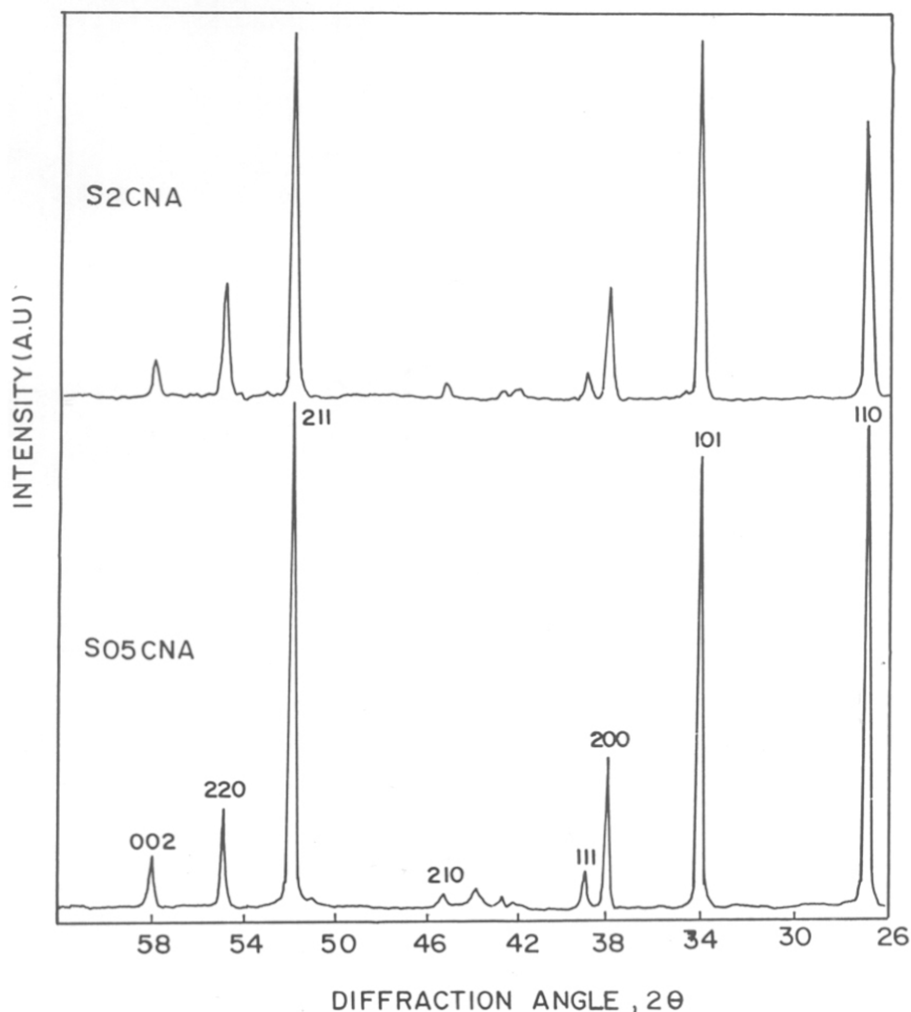

Figure 4.20 X-ray diffraction pattern of S05CNA and SCNA samples

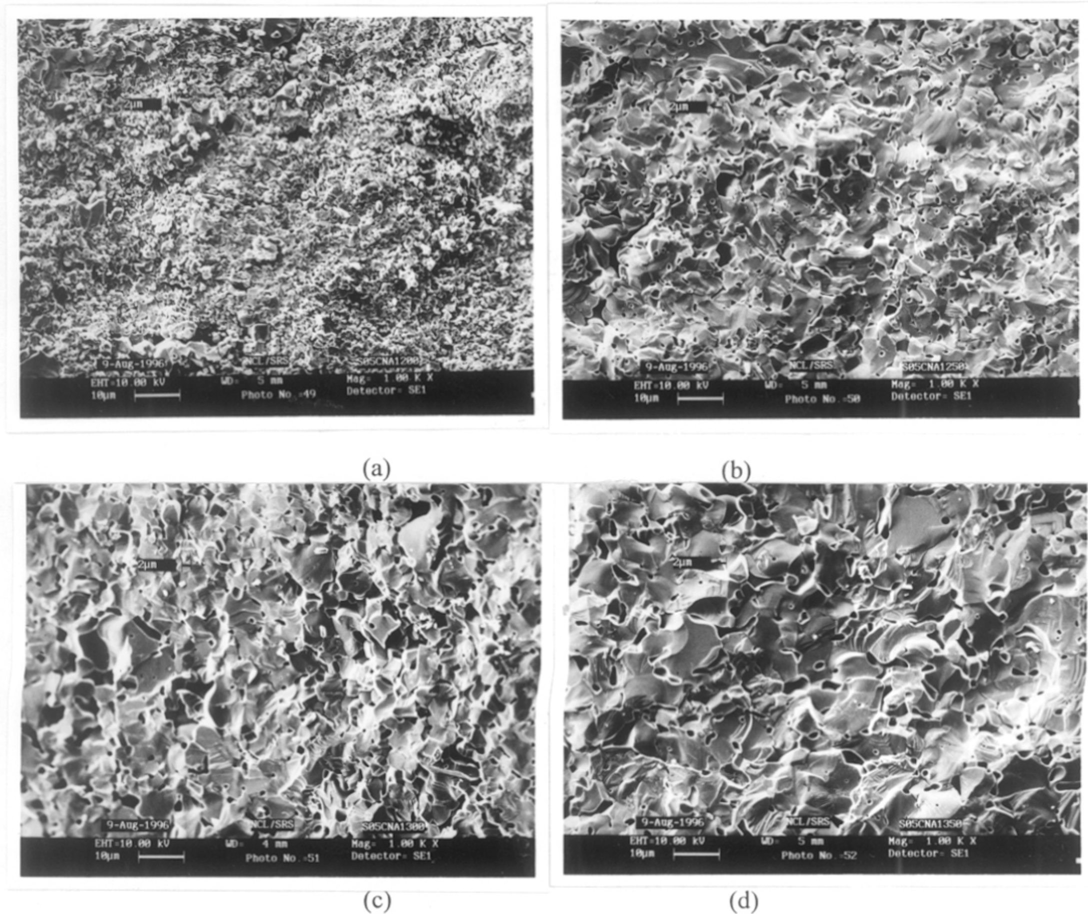

Figure4.21 SEM fractographs of S05CNA samples sintered at (a) 1200°C, (b) 1250°C, (c)1300°C and (d) 1350°C.

4.8.4 Scanning Electron Micrographs of fractured surface

Figures **4.21** and**4.22** show the fractographs of the S05CNA and S2CNA samples. Both samples show the typical behaviour of increase in grain size with increasing temperature. The S2CNA sample sintered at 1200°C shows more densification (less pores) compared to the S05CNA sintered at the same temperature. The grain size of both the samples are approximately equal (<2μm), similar to that observed in SCNA samples. As the sintering temperature is increased, the increase in grain size in S2CNA sample is larger compared to S05CNA samples.

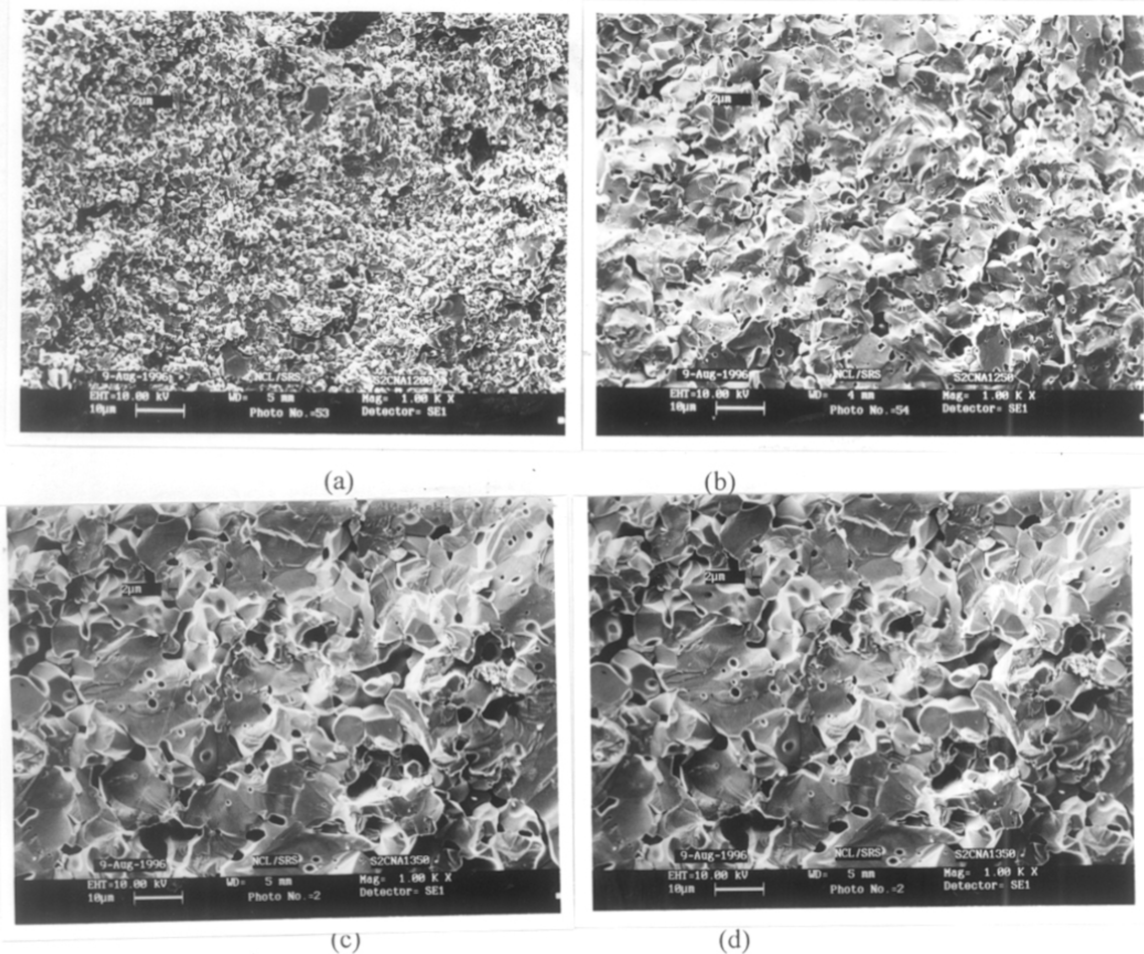

Figure 4.22 SEM fractographs of S2CNA samples sintered at (a) 1200°C, (b) 1250°C, (c)1300°C and (d) 1350°C.

Table 4.8 Grain sizes (µm)of S05CNA and S2CNA samples

Sample	1200°C	1250°C	1300°C	1350°C
S05CNA	1	2.5	5	7.5
S2CNA	1	4	7	8

The grain sizes observed at each sintering temperatures of S2CNA and S05CNA samples are given in Table **4.8**. It seems that at lower Co concentration (<1mol%), there is no influence of Co on the grain size distribution. But as the Co concentration increases, its effect on the grain size distribution is more, ie, it enhances grain growth. But this

enhancement of grain size is surely not the reason for the decrease in breakdown voltage observed in S2CNA samples. This is obvious since the grain size distribution in S05CNA and S2CNA doesnot differ much, but their breakdown voltage do differ. Hence Co must be introducing interfacial states which have a definite effect on the breakdown characteristics.

4.9 Chemically synthesized SCNA samples

As described in Chapter.1, the sample composition of SnO_2 varistor (SCNA) was synthesized by a chemical route to obtain homogeneous distribution of dopants. The chemical route of synthesis employed is described in Chapter.2. The following sections describe the experimental results and analysis of these samples which are abbreviated as SCNAC.

4.9.1 Current-voltage (I-V) characteristics

The current-voltage measurements carried out on the SCNAC samples sintered at 1200°C, 1250°C, 1300°C and 1350°C are given in figure **4.23** and the corresponding performance parameters are given in Table **4.9**.

The sample sintered at 1200°C didn't show any non-linear behaviour within the range of our measurements. The thickness of the pellet used in this particular case was only 0.5mm. Since decreasing the thickness further leads to large errors, the thickness was limited to 0.5mm. But from the nature of the I-V curve in the low current linear region, a tendency towards definite non-linearity is seen. This fact is supported by the fairly high grain boundary resistance of the sample (as indicated by the very low current in the pre-breakdown region). Hence the chemical synthesis seems to decrease the sintering temperature when compared to the ceramic route of synthesis.

At the sintering temperature 1250°C, an excellent non-linear behaviour is shown by this SnO_2 ceramic. A non-linearity coefficient as high as 72 is obtained in this case. This is 3 times higher than the same composition prepared by the ceramic route. The breakdown voltage of the sample is also increased to 1380 Volts/mm. The non-linearity coefficient of this sample is taken in the same range as the ceramic route prepared sample (1mA to 10mA).

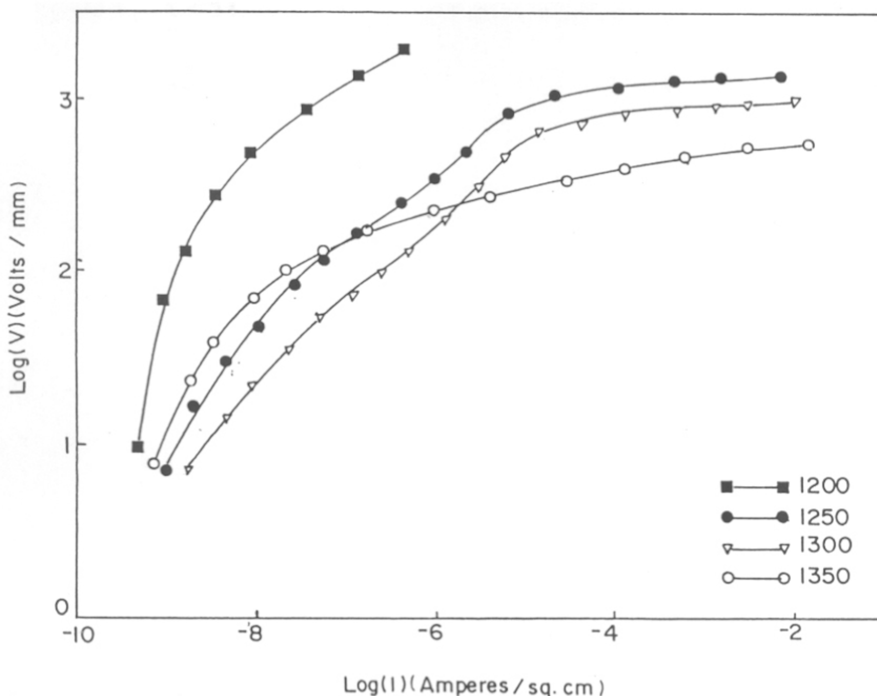

Figure 4.23 Current-voltage characteristics of SCNAC samples

At 1300°C, the sample still shows non-linear behaviour, but with $\propto \approx 37$ lesser than the sample sintered at 1250°C. This trend is similar to that observed in the sample prepared by the ceramic route also. The breakdown voltage in this case is E_{1mA} = 890volts/mm, which is brought about by the increase in grain size. Similarly, a decrease in the non-linear coefficient and breakdown voltage is observed when the sintering temperature was further increased to 1350°C. For this sample $\propto$ = 17.4 and E_{1mA}= 490 volts/mm.

Table 4.9 Performance parameters of SCNAC samples

Sintering temperature (°C)	Non-linear coefficient ($\propto$)	Breakdown voltage (E_{1mA}) volts/mm
1200	--	--
1250	72	1380
1300	37.7	890
1350	17.4	490

The homogeneous mixing of dopants by chemical synthesis have improved the property of the SnO_2 voltage sensor considerably. The microstructural and structural changes, if any, brought about by the chemical synthesis route is checked by taking the DTA/TGA curves, SEM fractographs, X-ray diffraction and measuring the density.

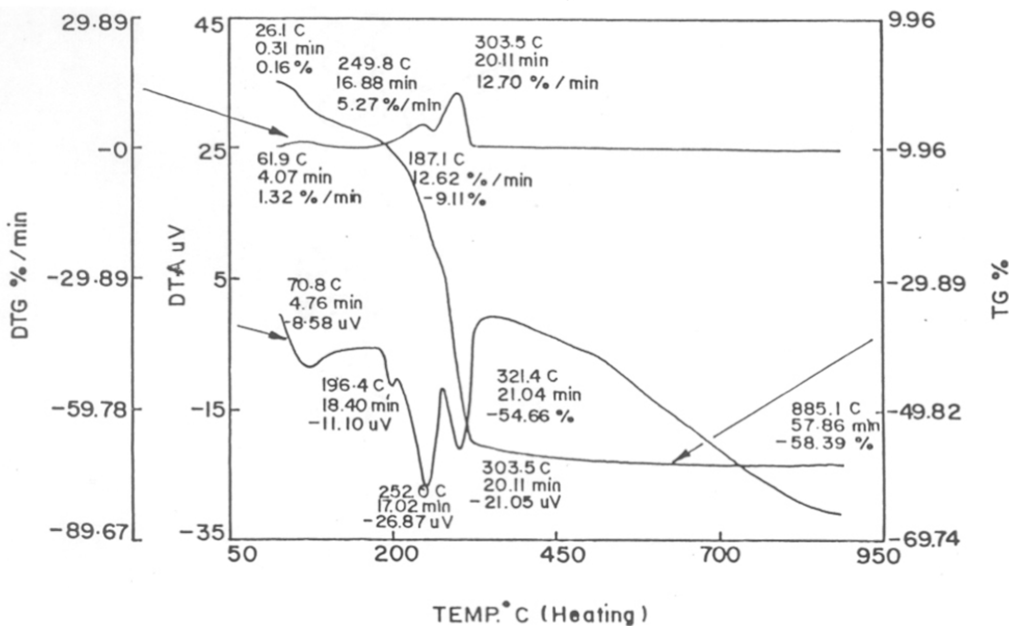

Figure 4.24 DTA/TGA/DTG curves of chemicaly prepared SnO_2 varistor powder.

4.9.2 DTA/TGA analysis

The well mixed chemically prepared powder was subjected to DTA/TGA/DTG analysis and the curves obtained are given in figure **4.24**. The endothermic loss at 187.1°C (9.11%) is related to loss due to adsorbed water. The endothermic losses at 252°C & 303°C (45.55%) are due to decomposition of hydroxide/ammonia complexes of Co and Sn respectively. After 450°C, There is no change in DTA/TGA/ DTG curves which indicated the formation of SnO_2 based varistor powder.

4.10.3 Density

Density of the chemically prepared samples is better than the ceramic samples. The density measured is plotted against the corresponding sintering temperature in figure **4.25**. The 1200°C sintered sample have the lowest density of 5.67gm/cc. As the sintering temperature increases, the density also increases and reaches a maximum value of 6.175gm/cc. All the samples prepared by this synthesis route have density greater than the corresponding density values of the sample prepared by the ceramic route. The improvement in the sintered densities is a direct consequence of the microcrystalline nature of the precipitated complex.

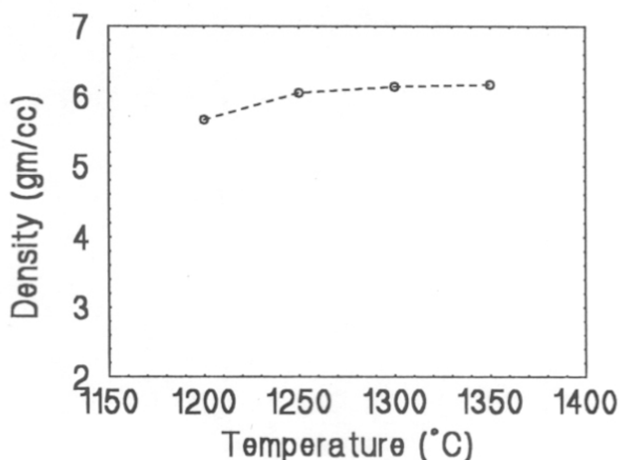

Figure 4.25 Measured density vs temperature of SCNAC samples.

4.9.4 X-ray diffraction for phase analysis

The X-ray diffraction pattern of the chemically prepared sample dried at 80°C and those calcined at 400°C, 800°C are plotted in figure **4.26**. At 80°C, the XRD pattern shows both broad and sharp peaks. The broad peaks correspond to rutile structure and indicates the presence of fine particles. The sharp peaks correspond to large particles corresponding to Tin complexes with ammonia which decomposes at higher calcining temperatures to form rutile SnO_2. At 400°C itself, the SnO_2 rutile phase is formed with broad peaks indicating very fine particles. As the calcination temperature is increased to 800°C, the crystallization increases showing finer peaks, which is also an indication of increase in particle size.

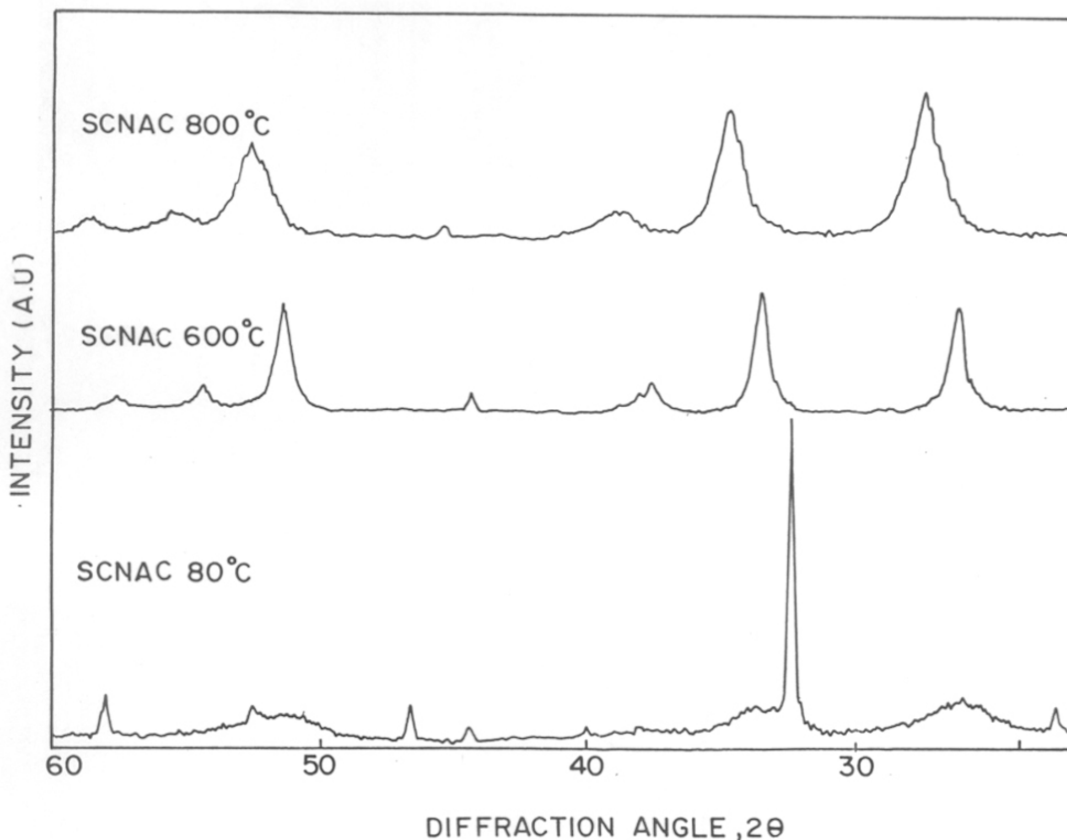

Figure 4.26 X-ray diffraction pattern of SCNAC powder at 80°C, 600°C and 800°C

Figure **4.27** shows the XRD patterns of the 800°C sample sintered at different temperatures. (1200, 1250, 1300 and 1350°C). The X-ray diffraction pattern shows well defined SnO_2 rutile structure. There are no additional diffraction peaks indicating no secondary phases are formed during the sintering process. The hkl indices 110, 101, 200, 111, 210, 211, 220 and 002 are indicated in the figure.

The relative intensity of the peaks compared to the rutile structure available in the literature differs since the XRD patterns were recorded on pellets. In pellets, orientation of planes can occur during sample shaping and formation. The lattice parameters of all the samples are similar. They are, a = b = 4.752A° and c = 3.183A°.

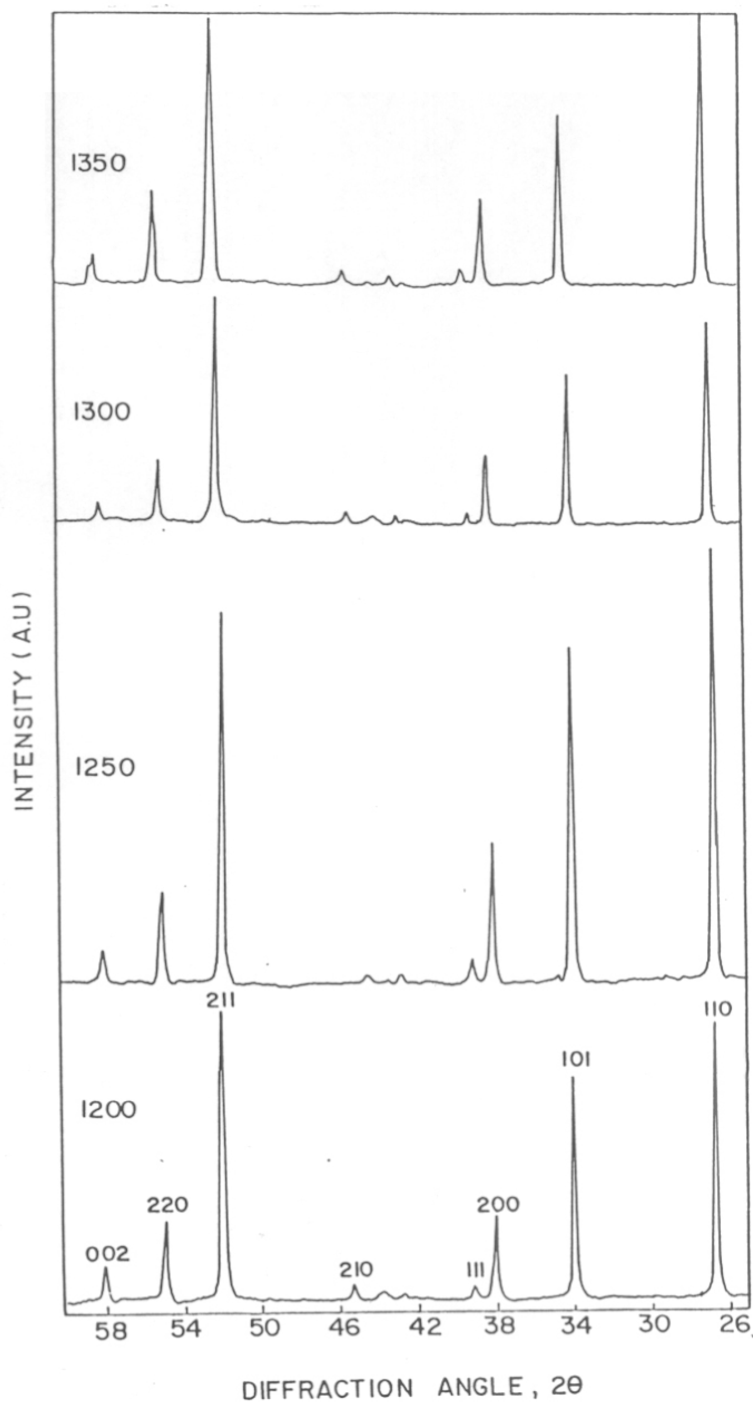

Figure[4.26] X-ray diffraction pattern of SCNAC pellets at 1200°C, 1250°C, 1300°C and 1350°C.

4.9.5 Scanning electron micrographs of fractured surface

The SEM fractographs of the chemically prepared samples sintered at 1200, 1250 1300 and 1350°C are given in Figure **4.28**. The average grain size observed in each case is given in Table **4.10**.

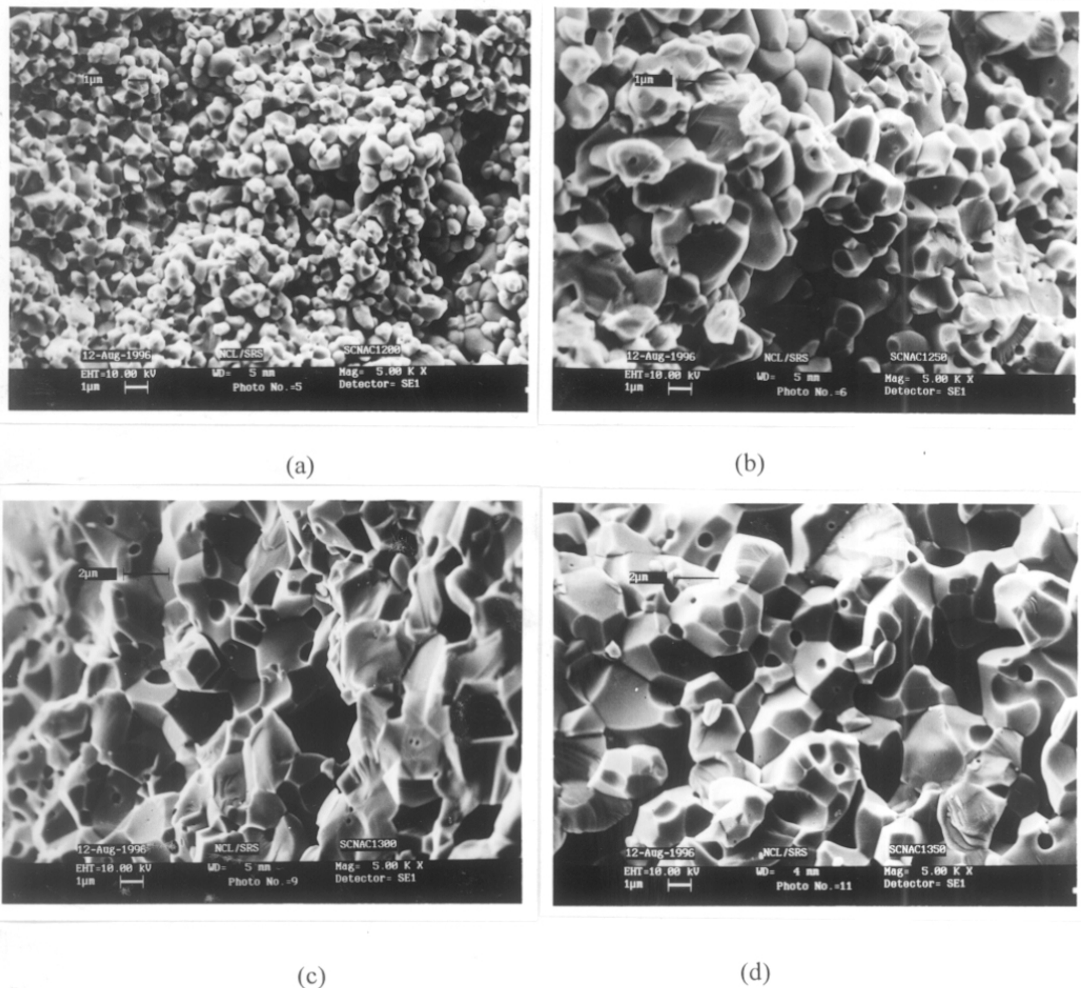

Figure 4.28 SEM fractographs of SCNAC samples sintered at (a)1200°C, (b)1250°C, (c)1300°C and (d) 1350°C.

At 1200°C, the grains are very small but uniformly distributed. The average grain size is <1μm. When the sintering temperature is increased to 1250°C, the grain size also increased to

~ 1μm. The most important aspect of these chemically prepared samples are that the grains are well formed with each grains clearly separated from each other (in the case of SCNA samples the grains had platelet like nature with no well defined grain boundaries). As the sintering temperature is increase to 1300°C, the grain size again increases to ~2μm. At 1350°C grain size further increase to 3μm.

With the chemical synthesis, the uniformity in the grain size is increased. The grains are well defined and the voids are reduced considerably. This is evident from the density measurements also. There are no additional phases or liquid like phases which are usually found in ZnO varistors. But as the sintering temperature is increased above 1300°C, abnormal grain growth is seen. Hence lower sintering temperature of 1250°C is necessary to attain reproducible well defined non-linear characteristics. The sintering temperature of 1250°C seems to be the ideal temperature both in terms of non-linearity and microstructural distribution. It is clear that the uniform distribution of dopants and grain sizes is important to get enhanced varistor characteristics.

Table 4.10 Grain size of SCNAC sample obtained from SEM

Sintering temp.(°C)	1200	1250	1300	1350
Grain size (μm)	<1	~1	~2	~3

4.9.6 Impedance analysis

The impedance plot for the SCNAC (sintered at 1250°C) sample measured at different temperatures is given in figure **4.29**. At room temperature, the impedance plot shows only a part of a large semicircle since the room temperature resistance of the sample is very high. As the measuring temperature is increased, a semicircular nature evolves. At 300°C, the sample shows a simple semicircle similar to that observed in SCNA samples. The individual contributions from the grains and grain boundaries cannot be separated out due to the high grain boundary impedance. Hence the Bode plots were plotted to separate the individual contributions as explained in equations (4.7) and (4.8).

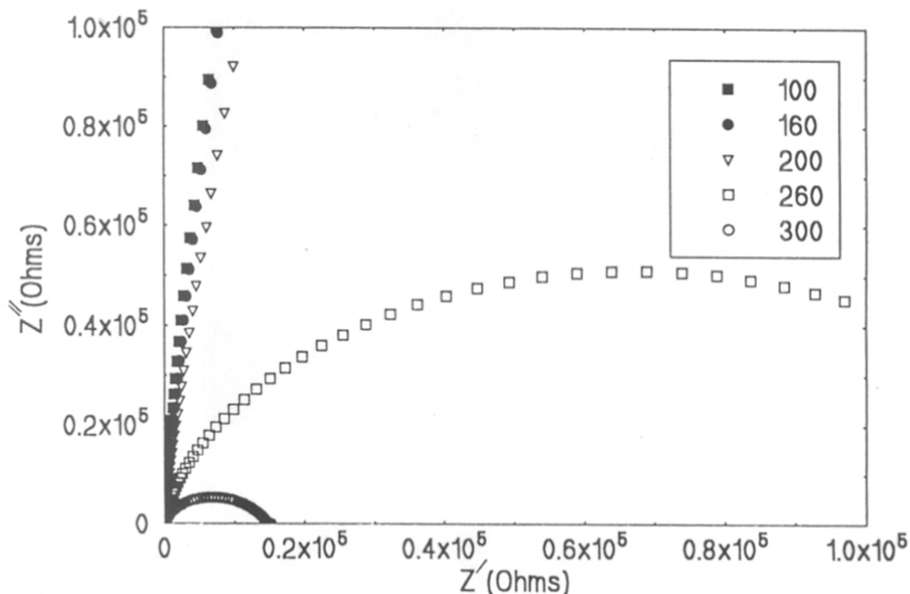

Figure4.29 Impedance plots (Z' vs Z'') of SCNAC sample measured at different temperatures.

The Bode plots of the chemically synthesized samples (1250°C) measured at various temperatures from RT to 300°C are given in figure **4.30**. The grain and grain boundary resistance and the corresponding grain boundary capacitance obtained from the Bode plots for this SCNAC sample is given in Table **4.11**.

In this case also, at low frequencies, the resistivity is in the range of $10^8\Omega$cm and as the frequency is increased to very high values (MHz range), the resistivity drops to ~100Ωcm. This indicates, as previously explained, the presence of grain-grain boundary-grain like structure (Capacitor like). This kind of microstructure gives rise to double Schottkey barriers which leads to excellent non-linear current-voltage behaviour. The above conclusion is supported by the phase change with frequency observed in this sample which is similar in nature to that observed in SCNA sample.

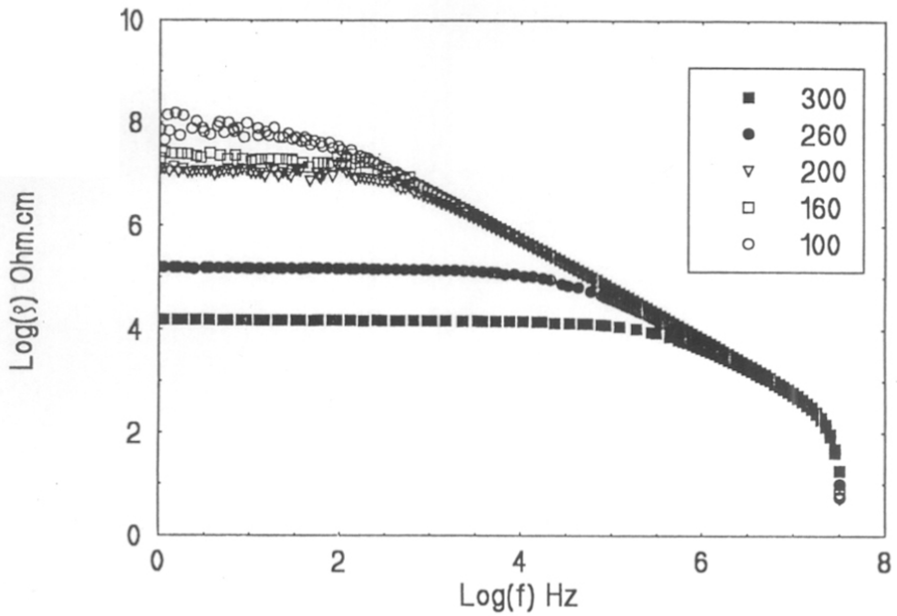

Figure 4.30 Bode plots for resistivity vs frequency of SCNAC sample measured at different temperatures.

Table 4.11 Grain resistivity(ρ_g), grain boundary resisitivity(ρ_{gb}) and grain boundary capacitance(C_{gb}) obtained from the Bode plots

Measuring temperature (°C)	ρ_{gb} (Ohm.cm)	ρ_g (Ohm.cm)	C_{gb} ($f.cm^{-2}$)
160	6.02×10^{7}	5.62	1.1487×10^{-11}
200	1.09×10^{7}	5.32	3.586×10^{-11}
260	1.51×10^{5}	10	2.711×10^{-11}
300	1.55×10^{4}	17.78	2.310×10^{-11}

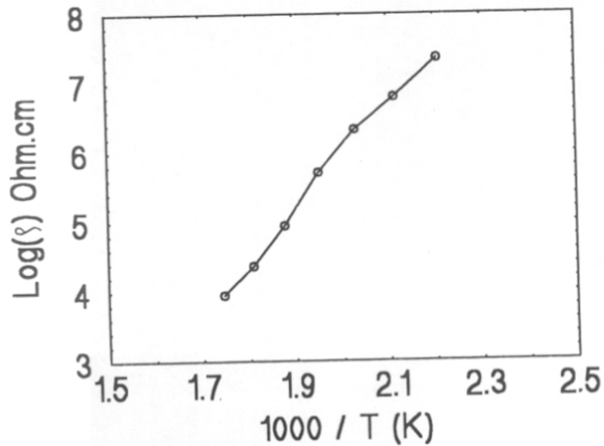

Figure 4.31 Arrhenius plot of SCNAC sample

The Arrhenius plots of the logarithm of grain boundary resistivity vs inverse of the measurement temperature for SCNAC sample is plotted similar to SCNA samples in figure **4.31**. The slope of the curve was found and the activation energy is calculated as explained in Section **4.7**. In this case, the activation energy is 0.697eV. This is more than double the activation energy obtained in the case of SCNA samples. The increase in activation energy points at the formation of more efficient energy barrier compared to the SCNA sample.

4.10 Discussion

The composition of SCNA (SnO_2, CoO, Nb_2O_5, Al_2O_3) is found to be an excellent non-linear resistor. The added dopants enter in the SnO_2 lattice structure and this is evident from the X-ray diffraction patterns which doesnot show any additional phases. This is because the ionic sizes of the dopants are of comparable value with the Sn^{4+} ions. CoO acts as the densifying agent as is evident from the increase in density with increase in CoO concentration. This is because the substitution of Sn^{4+} by Co^{2+} leads to the formation of oxygen vacancies, as described by equation(4.3), and in SnO_2 ceramics the rate controlling mechanism for sintering and densification is with the aid of oxygen vacancies

Nb^{5+} donates one more free electron to the system when it replaces Sn^{4+} (equation (4.1)). Hence the conductivity of the SnO_2 grains are increased. It is reported in the literature that Nb inhibits the grain growth also[9].

Al_2O_3 is the dopant which increases the non-linear coefficient of the varistor. It is already known that the SnO_2:CoO, Nb_2O_5 composition have a limited non-linear behaviour with an $\propto$ value of 8[9]. But the introduction of Al_2O_3 increases the $\propto$ value to 24. Hence it can be called as *performance enhancer* in this system.

Al_2O_3 doping in SnO_2 gives rise to the substitution of Sn^{4+} by Al^{3+} and thereby create oxygen vacancies.

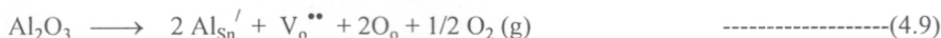

$$Al_2O_3 \longrightarrow 2\,Al_{Sn}^{/} + V_o^{\bullet\bullet} + 2O_o + 1/2\,O_2\,(g) \qquad \text{------------------(4.9)}$$

These dopants create defects alongwith the native defects occurring in the SnO_2 system during the sintering process. Hence a defect model is assumed in analogy with the defect model proposed in the case of ZnO varistors by Gupta et al (10) and in the case of TiO_2 varistor discussed in chapter **3**.

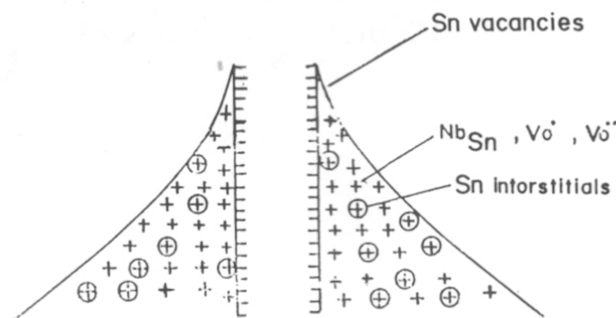

Figure 4.32 Defect model of SnO_2 voltage sensor.

The defect model is explained as follows: figure **4.32**. The positively charged ions are of two components. They are the oxygen vacancies created by doping with Al_2O_3 and CoO and the tin interstitials. These positively charged ions are compensated by the negatively charged ions at the interface. The negatively charged ions comprise of native tin vacancies. Hence a depletion layer of positive charge is formed in the grains during the sintering process. This creates an energy barrier leading to a Double Schottkey barrier (DSB) type structure[11] which gives rise to excellent non-linear current voltage behaviour. In this case

also, the conduction across the grain-grain boundary structure is explained by the hole induced tunneling mechanism[12,13].

As the Co concentration increases, the density also increases. The increase in Co concentration increases also the grain size. The Co dopants may introduce interface states which considerable influence on the breakdown characteristics of the varistor. This is the most likely reason for the drastic decrease in breakdown voltage of the S2CNA sample compared to the SCNA sample. The non-linear coefficient of the S2CNA sample is less than the SCNA sample. Therefore, large amount of Co addition have a deleterious effect on the current-voltage characteristics. With increase in Co concentration, it may be neutralizing the effect of Nb doping as an electron donor, since both Co and Nb occupy the lattice.

Chemical method of synthesis has considerably improved the non-linear characteristics. It is due to the uniform distribution of the dopants. The uniform disribution of dopants gives rise to a uniform distribution of the defects which are responsible for the formation of energy barrier resulting in improved non-linear current-voltage behaviour. The improved energy barrier is indicated by the improved activation energy of the grain boundary (as indicated by the impedance analysis).

4.11 Conclusions

The composition SCNA (SnO_2: CoO, Nb_2O_5 and Al_2O_3) is an excellent voltage sensor which have properties similar to ZnO varistors. A maximum non-linear coefficient($\propto$) as high as $\propto \approx 24$ and breakdown voltage of 700volts/mm in the case of sample prepared by the ceramic route. A further improvement of non-linear coefficient to $\propto \approx 72$ is observed in the case of chemically synthesized SCNA sample. The breakdown(E_{1mA}) voltage also increased to a very high value of 1380volts/mm. This improvement in the non-linear behaviour is brought about by the improved uniform distribution of dopants and related microstructure [14,15].

The impedance analysis is proved to be an excellent technique to understand the grain/grain boundary contribution to the varistor characteristics. The estimate of the activation energy of the grain boundary gives an indication about the physico-chemical details of the functional microstructure.

The absence of any low temperature liquid phase forming dopants like Bi_2O_3 will definitely improve the degradation characteristics of the varistor. The degradation study, improving the sintered density, study of the interface energy states brought about by the dopants are some of the aspects to be studied extensively to understand the SnO_2 varistor system completely. It is expected to be a worthy competitor on the basis of cost-benefit ratio to the proven ZnO voltage sensor.

References

1. Z.M.Jarzebski and J.P.Marton., *J.Electrochem.Soc.*, **123**, 199C(1976).
   Z.M.Jarzebski and J.P.Marton., *J.Electrochem.Soc.*, **123**, 299C(1976).
   Z.M.Jarzebski and J.P.Marton., *J.Electrochem.Soc.*, **123**, 333C(1976).
2. C.G.Fonstad and R.H.Redikar., *J.Appl.Phys.*, **42**, 2911(1971).
3. R.W.Mar., *J.Phys.Chem.Solids.*, **33**, 220(1972).
4. J.A.Varela, O.J.Whittemore and E.Longo., *Ceram.Int.*, **16**, 177(1990).
5. K.P.Kumar and A.D.Damodaran., *J.Mater.Sci.Lett.*, **8**, 1425(1989).
6. M.K.Paria and H.S.Maiti., *J.Mater.Sci.*, **18**, 2101(1983).
7. R.D.Shannon., *Acta.Cryst.*, **A32**, 751(1976).
8. W.H.Bauer., *Acta.Cryst.*, **9**, 515(1956).
9. D.Gouvea, M.H.Kobori, J.A.Varela, W.C.Las, C.V.Santilli and E.Longo., *Ceramics Today-Tomorrows ceramics*, p2091, Part C, Materials Science Monographs, **66C**, Ed.by P.Vincenzini, Elsevier, 1991.
10. T.K.Gupta and W.G.Carlson., *J.Mater.Sci.*, **20**, 3487(1985).
11. T.K.Gupta., *J.Amer.Ceram.Soc.*, **73**, 1817(1990).
12. H.R.Philipp and L.M.Levinson., *J.Appl.Phys.*, **46**, 3206(1975).
13. G.Blatter and F.Grueter., *Phys.Rev.B.*, **34**, 8555(1986).
14. P.N.Santhosh and S.K.Date., *Bull.Mater.Sci.*, **19**, 713(1996).
15. P.N.Santhosh, H.S.Potdar and S.K.Date., *J.Mater.Res.*, (1997) (in press).

List of Publications

1. Chemical synthesis of a new tin oxide based (SnO_2:Co,Al,Nb) varistor

   P.N.Santhosh, H.S.Potadar and S.K.Date., *J.Mater.Res*., (Feb., 1997) (in press).

2. Electrical characterization of ceramic voltage sensors by impedance spectroscopy

   P.N.Santhosh, D.K.Kharat, S.K.Date and A.R.Kulkarni., *Asian Journal of Physics*., (1997) (in press).

3. A new ceramic voltage sensor: SnO_2 doped with Co, Nb, Al

   P.N.Santhosh and S.K.Date., *Bull.Mater.Sci*., **19**, 713(1996).

4. Effect of strontium substitution in (Nb,Bi) doped TiO_2 varistors

   P.N.Santhosh, D.K.Kharat and S.K.Date., *Mater.Lett*., **28**, 37(1996).

5. On the origin of itinerant electron behaviour and long-range ferromagnetic order in $La_{1-x}Sr_xCoO_3$.

   P.Ganguly, P.S.Anil Kumar, **P.N.Santhosh** and I.S.Mulla., *J.Physics: Condens. Mater*., **6**, 533(1994).

6. Impedance analysis of the new SnO_2 based varistors

   P.N.Santhosh, S.K.Date and A.R.Kulkarni.,(1996) (to be communicated)

Papers presented at Conferences

1. A new ceramic voltage sensor: SnO_2:Nb,Co,Al.

   P.N.Santhosh, S.R.Sainkar, J.J.Shrotri and S.K.Date, C3-1, Proceedings of the third National seminar on physics and technology of sensors helh at University of Pune, 1996.

2. Microstructural engineering of ceramic voltage sensors

   S.K.Date, **P.N.Santhosh**, D.K.Kharat and A.Mitra, C4-1, Proceedings of the third National seminar on physics and technology of sensors helh at University of Pune, 1996.

3. Electrical characterization of ceramic voltage sensors by impedance spectroscopy

   P.N.Santhosh, D.K.Kharat, S.K.Date and A.R.Kulkarni., presented at the DAE-BRNS symposium on electroceramics held at Rajkot in March 1996.